UNIVERSITÀ DEGLI STUDI DI PADOVA

Dipartimento di Ingegneria Industriale DII

Corso di Laurea Magistrale in Ingegneria Aerospaziale

Feasibility of Aerocapture in a Rapid Crewed Mission to Mars

Relatore: Enrico Lorenzini

Alessia Rigato 2048417

Anno Accademico 2023/2024

To my grandmothers, Rodica and Giselda, whose blue eyes could never land on a degree, but always landed, lovingly, on mine.

Acknowledgments

First of all, I'd like to express my gratitude to Professor Paulo Gil for the precious time he has dedicated to me, for the passion he sparks when talking about space exploration, and for the care with which he ensured that I could find a welcoming place in a city I had just landed in.

Heartfelt thanks go to Professor Mario Lino da Silva for his valuable guidance and expertise, and to Filipe Teixeira for dedicating a Friday evening to resolving my doubts about the studies that have laid the foundations for this.

To Alice, Beatrice, Federico, Klara, Sophie, Silvia, and Stans for making Portugal a cherished memory of evenings spent sitting on the ground, afternoons defending what we believe in, and sunsets over the most wonderful landscapes.

To Julio, Andrés, and Dimitar for the fortune that led me to spend six months in a foggy hinterland with people who make me remember it as the sunniest of places.

To Laura for sharing the burden of a master's degree that, alone, would have overwhelmed me.

To Leila, for being simultaneously my younger and older sister, for her sharp intelligence, and her sensitivity.

To Beatrice, Chanele, Elisa, and Emma because in the most difficult moments and in the loudest laughs, they were there.

To Benedetta, Giacomo, Margherita, and Serena for being my second family, the lenses through which I perceive the world, and the people I am sure I will encounter, even in old age, in the place we grew up in.

To Riccardo, for everything he is and for offering me every day the gaze under which I understand who I am.

Lastly, I am deeply thankful to my parents, brother, aunts, uncle, cousins, and grandparents, who are my measure of love, for teaching me everything I know and making me everything I feel like I am.

Abstract

Rapid missions would be a desirable way for people to reach Mars, ensuring crew safety against the hazards of sustained exposure to reduced gravity and radiation, although posing significant challenges in terms of mass and deceleration requirements, for which suitable propulsion systems are yet to be developed.

This work investigates the integration of aerocapture as a strategy to reduce propellant expenditure at Mars, aiming to reduce overall mission mass and duration.

The interplanetary trajectory that leads to rapidly reaching Mars from Low Earth Orbit is defined alongside a spacecraft that can safely accommodate the crew, subsystems, multiple tanks, and a potentially massive propulsion system.

Following a detailed assessment of the atmospheric entry environment, a $70°$ sphere-cone aeroshield is designed to ensure sufficient deceleration for the spacecraft. Key constraints to ensure crew safety and mission success are identified and shown to impose limits on the entry velocity, entry mass, and aeroshield size.

Pareto fronts for the Initial Mass in Low Earth Orbit are traced for missions employing aerocapture versus those relying solely on propulsion systems, considering various mission durations and propulsion technologies. Results reveal the potential of aerocapture to enable shorter transfer durations across all propulsion systems, with mass benefits exceeding 80% for available options, albeit diminishing with increasing propulsion system efficiency.

Aerocapture seems to offer a viable way to significantly diminish the mass, and therefore the price, of rapid crewed missions to Mars.

Contents

List of Tables

List of Figures

Nomenclature

Greek symbols

α Angle of attack [°]

β Ballistic coefficient [kg/m^2]

β_{Mach} Mach angle [°]

Δt Finite change in time [s]

Δv Finite change in velocity [km/s]

δ Sphere-cone half angle [°]

ϵ_{t} Structural ratio

γ Flight path angle [°]

λ Mean free path between the particles [m]

μ Standard gravitational parameter [km^3/s^2]

ω Angular orbital velocity [rad/s]

ρ Density [kg/m^3]

Θ Angle at the leading edge of a body [°]

θ Orbital angle [°]

Roman symbols

A Reference area [m^2]

a Semi-major axis [km]

c Speed of sound [km/s]

C_{D} Coefficient of drag

c_{i} Mass fraction of the species i

C_{L} Coefficient of lift

C_P Coefficient of pressure

D Drag force [N]

d Duration of the outbound segment [days]

f_TPS TPS mass fraction [%]

g_0 Gravitational acceleration at the surface of the Earth [m/s^2]

h Altitude [km]

I_sp Specific Impulse [s]

K Heat transfer coefficient [kg/(s m$^{3/2}$atm$^{1/2}$)]

L Lift force [N]

L/D Lift-to-drag ratio

L_c Characteristic length of a body [m]

m Mass [t]

M_i Molecular weight of the species i

N_crew Number of crew members

Q Heat load [J/cm^2]

q Heat rate

Kn   Knudsen number

M   Mach number

$\mathbf{r}$ Position vector

R Planetary radius [km]

r Orbital radius [km]

R_a Tapering ratio

R_B Base radius of the aeroshield [m]

R_N Nose radius of the aeroshield [m]

Re   Reynolds number

T Thrust [N]

t Thickness [m]

T/W Thrust-to-weight ratio

$\mathbf{v}$	Velocity vector
V	Volume [m^3]
v	Velocity [km/s]

Subscripts

0	Initial
f	Final
E	Earth
M	Mars
S	Sun
∞	Infinity
ell	Elliptical
hyp	Hyperbolic
p	Perigee
atm	Atmosphere
pl	Payload
pr	Propellant
c	Convective
r	Radiative
ms	Aeroshield main structure
sc	Spherical cap
tc	Truncated cone
x,y,z	Cartesian components
i	Index of summation

Acronyms

ADCS   Attitude Determination and Control System

AFE   Aeroassist Flight Experiment

AMAT   Aerocapture Mission Analysis Tool

AU   Astronomical Unit

CFD   Computational Fluid Dynamics

DHCS   Data Handling and Control System

DRA   Human Exploration of Mars Design Reference Architecture 5.0

ECLSS   Environmental Control and Life Support System

EPS   Electrical Power System

ESA   European Space Agency

GRAM   Global Reference Atmospheric Model

HEEET   Heatshield for Extreme Entry Environment Technology

IMLEO   Initial Mass in Low Earth Orbit

LEO   Low Earth Orbit

MAV   Mars Ascent Vehicle

MDM   Mars Descent Module

MGS   Mars Global Surveyor

MRO   Mars Reconnaissance Orbiter

MSL   Mars Science Laboratory

NASA   National Aeronautics and Space Administration

PICA   Phenolic-Impregnated Carbon Ablator

SHAB   Surface Habitat

TCS   Thermal Control System

TCW   Theoretical Corridor Width

TGO   ExoMars Trace Gas Orbiter

THAB   Transit Habitat

TPS   Thermal Protection System

TRL   Technology Readiness Level

Chapter 1

Introduction

1.1 Objectives and Motivation

This work aims to assess the feasibility of implementing aerocapture as an entry strategy for missions to Mars [1, 2]. As rapid missions entail significant masses and velocities, it is crucial to explore the possibility of integrating aerocapture as a complementary strategy alongside traditional propulsive braking. The complexity of the problem and the substantial masses involved require careful consideration in defining a spacecraft configuration capable of completing the interplanetary journey and performing the aerocapture maneuver. Feasibility, in this context, extends beyond merely evaluating the success of the maneuver, as it is essential to determine whether it is achievable while respecting the additional constraints imposed by human presence, in order to guarantee crew safety and mission success.

After the Moon landing in 1969, the next logical destination for humans to set foot on is Mars. Although Venus is closer [3, 4], Mars has a temperature, pressure, and gravity that, while being certainly lower than those of Earth, are way more appealing than the extreme conditions one would encounter on Venus. Two of the main obstacles standing in the way of achieving this goal are the duration of the journey and the prolonged stay on the surface, which pose risks to the well-being of the astronauts [5]. Therefore, it is crucial to minimize the mission time while also optimizing the mass of the spacecraft so that mission feasibility is ensured. With these premises, aerocapture can be a promising way to significantly cut on propellant mass, especially in the case of fast missions, where any savings can be very advantageous to the already large total mass of the mission [1].

1.2 The Aerocapture Strategy

Human missions to Mars have dominated the imagination of men since immemorable times, although we can pinpoint the first conceptual human mission to the Red Planet to date back to 1947, authored by the aerospace engineer Wernher von Braun [6]. His work inaugurated half a century of prolific mission design (more than 1000 missions have been designed only between 1950 and 2000 [6]), which has undoubtedly continued with the coming of the new millennium.

Although many unmanned missions have successfully landed on Mars [7], adding a crew to the equation represents a significant complication of the problem, mainly because of the long time necessary to reach, stay, and return from the planet, which is essential to reduce as much as possible [5]. This is why, in the following work, aerocapture is analyzed as a potential technology supporting rapid crewed missions to Mars [1, 2]. The association of the terms "crewed" and "rapid" is indispensable, as the need for speed arises precisely from the presence of humans on board, achievable in safety only by reducing the travel time to limit excessive exposure to radiation [5, 8] and to the absence of gravity [5, 9, 10]. The necessity to shorten mission duration involves achieving extremely high velocities and is only possible with the use of an exceptionally massive propulsion system. The obstacles posed to the traditional study of aerocapture are, therefore, numerous, as an entry velocity not found in scientific literature is coupled with a remarkably high mass. Additionally, the geometry of the spacecraft, required to accommodate the numerous tanks necessary for the interplanetary trajectory, deserves special consideration.

Aerocapture is a flight maneuver that takes advantage of the atmosphere of a celestial body to insert a spacecraft into a desired orbit in a quick, propellant-free way. A vehicle approaching on a hyperbolic orbit moves away after having reached periapsis unless enough of its kinetic energy is depleted. The traditional approach to dissipating this energy is to perform a propulsive change in velocity (Δv) in a direction opposite to that of motion, but aerocapture employs the aerodynamic drag generated by atmospheric friction to perform that Δv [11, p.386].

In an aerocapture maneuver, which is schematically represented in Figure 1.1, three distinct phases are generally distinguished. The operation starts with the approach, during which the spacecraft advances towards the planet on a hyperbolic trajectory. As it penetrates the atmosphere of the celestial body, the aerodynamic braking process commences. Energy dissipation occurs during this atmospheric flight phase, making it crucial for the spacecraft to maintain a specific altitude and orientation to ensure the desired atmospheric drag. The final phase involves exiting the atmosphere, after which the orbit, now elliptical, is adjusted at apoapsis so that the spacecraft no longer re-enters the atmosphere, preventing further energy dissipation [12].

The topic of aerocapture and its applicability to missions in the solar system have been studied for decades as an alternative way to propulsive braking to insert a spacecraft in orbit around an atmosphere-bearing body. The idea of using aerodynamic forces to achieve orbital change was first introduced by Howard S. London in 1962 [13] and paved the way for subsequent studies. The first mention of aerocapture in scientific literature dates back to 1979 [14], when the concept was introduced and first examined precisely in the context of a mission to Mars. Already at that time, not only the feasibility of the mission was demonstrated, but also the advantages that the use of this new technology would entail, especially in terms of mass savings in comparison with the purely propulsive scenario.

Indeed, since propellant usage is limited to the final periapsis-raising maneuver, aerocapture allows for saving most of the propellant mass that would be needed for the spacecraft to be captured, and this can significantly reduce its overall mass. Over the years, many studies, e.g., [15–18], have confirmed that the saving of propellant vastly outweighs any extra mass that might need to be allocated for the drag-inducing and heat-protecting aeroshell. This advantage can be even more significant when the
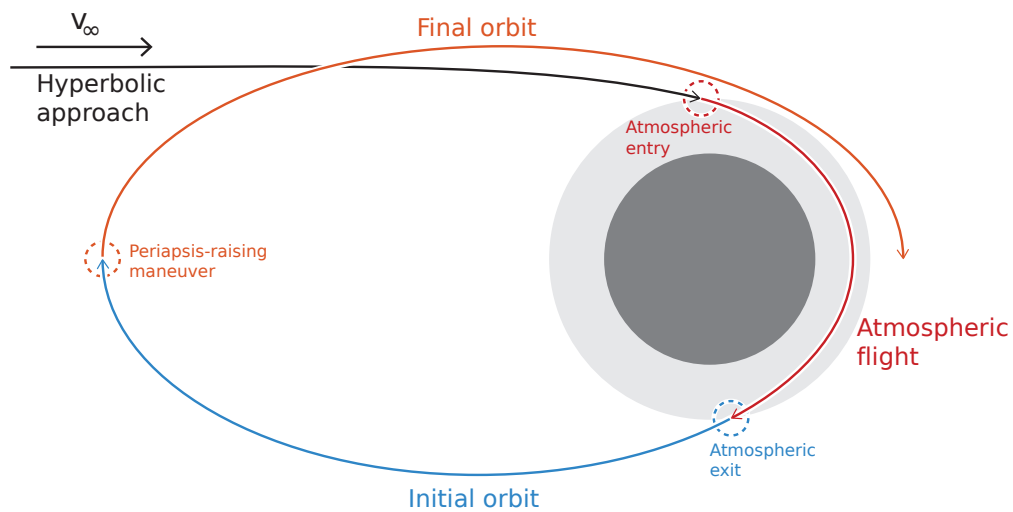
Figure 1.1: Representation of the main phases of aerocapture.

orbit insertion velocity change is large [19], such as in high-energy missions. At the same time, though, it must be taken into account that in those cases atmospheric drag can be insufficient to perform the whole capture maneuver and a combination with propulsive braking may have to be considered. Also, large maneuvers can have implications on the spacecraft configuration and introduce additional constraints. Because of its potential to save propellant, aerocapture also looks appealing from a cost-reduction point of view. When analyzed, though, this aspect does not show a substantial improvement when compared to the non-aerocapture scenario because, for most missions, orbit insertion costs only constitute a small fraction of the overall mission cost [15].

Aerocapture is not a technology that can be easily implemented on any type of mission. Naturally, it is limited to planets and moons that have an atmosphere. At the same time, the atmosphere must have favorable thermodynamic properties and composition to allow for sufficient deceleration while still imposing acceptable heating rates on the spacecraft. The gravity of the celestial body also plays an important role, as a greater gravitational pull induces a higher approaching velocity at the beginning of the atmosphere [20].

For these reasons, Mars represents a strong candidate for the employment of aerocapture, with a gravitational pull of about 40% of that of Earth and a relatively thin atmosphere, whose density is about 1% of that of Earth, which, while preventing excessive heating, raises concerns about its capacity to induce sufficient drag [20]. Therefore, in order to conduct successful aerocapture, it is necessary to go deep into it and close to the surface of the planet, but since the Tharsis region, a mountainous area rising up to 25 km above the mean surface, constitutes up to 25% of the surface of the planet [21–23], it is not recommended to ever go below 30 km [24, 25].

The atmospheric interface represents the altitude at which the atmosphere becomes so rarefied it induces negligible drag. Most aerocapture analyses put it at 125 km [20, 26], and although there are a few that consider higher ones, such as 300 km [27] or 195 km [25], this definition should not greatly

impact mission design, since deceleration mostly happens at significantly lower altitudes [20].

The addition of a human crew to the aerocapture scenario does not undermine the feasibility of the mission; however, it imposes constraints on the maximum allowable deceleration compared to unmanned spacecraft. Traditionally, five times the acceleration of gravity at the surface of the Earth ($5g$) is taken as the limit deceleration for manned missions [19, 27, 28]. Nevertheless, this is to be considered an average value, as the safety of the crew depends on the duration of exposure to such loads and their direction relative to the human body [29, 30]. Depending on these conditions, the acceptable acceleration levels can vary from about $0.5g$ for sustained loads coming from the top to as high as $38g$ for impulsive loads coming from the front [29, 30].

Though aerocapture has never been performed yet, the scientific community agrees that we currently are at a technological readiness level to perform it, at least on Venus, Mars, and Titan [16] and that while a demonstrative mission could be conducted to set a precedent, it is not strictly necessary to actively start employing the technology. Moreover, in the context of employing aerodynamic forces to conduct orbital maneuvers, aerocapture is not the only strategy that has been developed, and precedents have already been set. Aerobraking is the process of progressively lowering the apoapsis of the elliptical orbit of an already captured spacecraft, usually with various passes through the atmosphere of the planet. So, while it is also a technique that uses aerodynamic drag to achieve a propellant-free Δv, it differs from aerocapture for starting conditions and purpose, and consequently for characterization of the vehicle [31]. Contrary to aerocapture, there are several successful examples of aerobraking on Venus [32, 33], Earth [34], and Mars [35–38], the last one being that of the European Space Agency (ESA) ExoMars Trace Gas Orbiter (TGO) [38].

Aerocapture, alongside its advantages, presents some inherent risks and challenges that need to be assessed. One significant risk is associated with atmosphere and gravity field uncertainties, stemming from our limited knowledge of planets other than Earth, spatial and temporal variations in atmospheric conditions, and occurrence of random fluid dynamics phenomena [16]. For Mars, the uncertainties in the density profile are mainly linked to the seasonal variability of the atmosphere and are shown to increase with altitude. At heights relevant for aerocapture, the 3σ density variations are estimated to vary between $\pm10\%$ at 30 km up to $\pm50\%$ at 80 km; at the entry interface, 125 km, they can even surpass $\pm100\%$, but the atmosphere is so rarefied up there that this does not impose great variations on the exerted drag [39]. Because of this phenomenon, it is essential to consider a sufficiently broad range of encounterable densities during mission design and make sure that an entry corridor exists with a certain level of safety. This is also particularly valid during the atmospheric flight phase, where the spacecraft must be maintained at the right altitude and orientation to ensure the right amount of energy is dissipated. Additionally, during the actual flight, an accurate guidance system must counteract deviations from the nominal trajectory.

Another substantial risk of aerocapture concerns the high temperatures resulting from the interaction with the atmosphere, which both enables and constrains the maneuver [16]. It is crucial to precisely evaluate the stagnation-point heating rates and integrated heat load in order to address them by providing the spacecraft with an efficient Thermal Protection System (TPS).

4
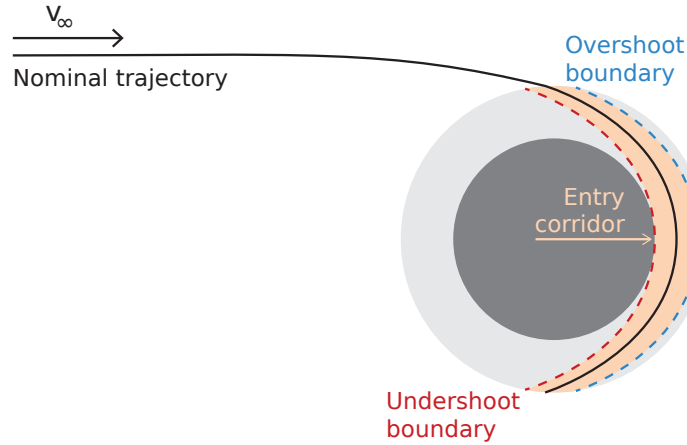
Figure 1.2: Schematic representation of the entry corridor and of undershoot and overshoot boundaries.

To ensure the success of the mission, the vehicle must enter a specific entry corridor (represented in Figure 1.2), defined as the range of trajectories within which the spacecraft is captured [27, 40]. This entry corridor primarily depends on four parameters:

- Entry velocity v_{entry} [m/s] is the speed at which the spacecraft enters the atmosphere of the celestial body at the altitude where the atmosphere interface is assumed to be (in the case of Mars, it will be assumed at 125 km). It is a direct consequence of the interplanetary trajectory, and, as such, it is closely linked to the transfer time. In the case of rapid missions, it will be particularly large, but it must be kept under control as it determines the magnitude of heating rates and decelerations, and the overall feasibility of aerocapture [41, p. 406].

- Flight path angle γ [°] represents the angle between the velocity vector and the normal to the position vector, so it is essentially the angle at which the spacecraft is descending relatively to the horizon [41, p. 41]. The maximum entry flight path angle γ_{max} defines the overshoot boundary, representing the shallowest angle at which the vehicle can enter and develop enough drag to be captured. Conversely, the minimum entry flight path angle γ_{min}, which establishes the undershoot boundary, is the steepest angle at which capture is achieved without hitting the surface. The difference between those two angles defines the width of the entry corridor, the Theoretical Corridor Width (TCW) [12]:

$$TCW = \gamma_{\text{max}} - \gamma_{\text{min}}. \tag{1.1}$$

- Lift-to-drag ratio L/D represents the ratio of the lift force L [N] to the drag force D [N], the two aerodynamic forces resulting from the interaction between the spacecraft and the atmosphere. It depends on the angle of attack α (defined as the angle between the reference line of the body and the incoming flow [41, p. 145]), the atmospheric density, and the velocity relative to the incoming flow. Higher values of it ($L/D > 1.0$) are indicative of slim bodies, such as slender cones or biconics, while lower values ($L/D < 1.0$) apply to capsule-shaped blunt bodies, whose main purpose is to develop drag in order to be decelerated [19; 41, p. 143]. Consequently, in the context

of aerocapture, a low L/D is expected.

- Drag coefficient C_D is a dimensionless parameter that indicates the drag experienced by a rigid body immersed in a fluid independently of its size or the characteristics of the fluid, so it only depends on the shape of the body and its angle of attack. It can be defined as

$$C_D = \frac{D}{\frac{1}{2}\rho V^2 A},$$ (1.2)

where ρ is the density of the fluid in kg/m^3, v is the velocity of the stream in m/s, and A is the reference area in m^2.

Alternatively to the drag coefficient, in aerocapture and aerobraking literature attention is often focused on the ballistic coefficient β [kg/m^2], alternatively defined as either the ratio of the mass of the spacecraft to its drag coefficient and reference area [42, p.46; 43, p. 106]:

$$\beta = \frac{m}{C_D A},$$ (1.3)

or the inverse of it [41, p.452; 40, Ch. 12-13]. The term "ballistic" traditionally refers to the trajectory of a body primarily influenced by gravity and drag rather than aerodynamic lift, but since $L = 0$ is only achievable by spherical reentry bodies, it is considered ballistic a trajectory where gravitational and drag forces dominate over lift ones. Its importance is predominant for cases in which control is achieved via drag modulation, but in this work, where mass will always be a continuously varying parameter, the use of the drag coefficient will be preferred over the ballistic coefficient in providing a measure of the drag.

1.3   State of the Art

Human missions to Mars have always been of great interest to the aerospace community, leading National Aeronautics and Space Administration (NASA) to define a mission baseline that incorporates all aspects and strategies to be considered for their realization: the Human Exploration of Mars Design Reference Architecture 5.0 (DRA) [5]. In this report, the round-trip time of these types of missions first depends on the strategy chosen to synchronize the outbound and inbound legs of the journey: Conjunction Class missions are characterized by a long stay on the planet (475 to 540 days) and a long total round-trip time (850 to 950 days), while Opposition Class missions have a short stay time (30 days to 90 days) and a short round-trip time (400 to 650 days) [5]. Proposals of a similar nature also yield total journey durations of up to 971 days, particularly when Conjunction Class missions are preferred due to their longer duration of stay, cost-effectiveness, and reduced risk [44–46]. When choosing Opposition Class missions, the total time can go down to 407 days [46]. Rapid missions, achievable when the spacecraft goes back to Earth before it completes a revolution around the Sun, have been barely considered in literature [1, 2, 45, 46], but show how the total trip time can theoretically be brought down to less than 180 days.

Rapid missions imply the need for a significant amount of propellant, leading to an increase in the mass of the spacecraft, thereby requiring even more propellant. For this reason, it is important to achieve the lowest possible mass [5]. Many proposals aiming towards this goal have been advanced. It is generally accepted that it is necessary to divide the mission into its cargo and crewed components [1, 5, 46–48], sending the cargo segments in advance on a longer trajectory while still granting the shortest possible one to the crewed segment. The possibility of employing a Venus gravity assist has also been studied, as it would allow for a propellant-free way to increase the energy of the trajectory. While it has been shown that this is a viable way to reduce propellant requirements and trip times [49–51], the total time of flight still results in over a year for all the studied cases. Another interesting option is represented by cycler orbits [52–55], characterized by a transfer vehicle on a heliocentric orbit that periodically encounters both Earth and Mars, allowing for regular crew transfers between the two planets. Although promising, this strategy is quite complex and would hence be more beneficial for regular transfers to Mars rather than a first rapid exploratory mission. Additionally, most of the current proposals still consider total mission durations of over a year [52, 53, 55]. Rotating tether systems may also constitute an interesting addition, as they allow for shorter transfer times when compared to the previously cited methods [56], but there are only a few studies about them, and the associated complexity and risks suggest further investigation should be conducted.

Taking advantage of the atmosphere of Mars to decelerate has been considered in the form of parachutes, aerobraking, and aerocapture. The employment of parachutes can be an important addition that allows for saving propellant in the last stages of the mission [48, 57], but they can only be deployed at Mach numbers lower than three [48] and result more beneficial for smaller and lighter spacecrafts, while their benefits decrease as vehicle mass increases [57]. Aerobraking is to be discarded for a crewed scenario, as the necessity of several passages through the atmosphere would inevitably increase the mission time to unacceptable levels [46, 57]. Aerocapture, on the other hand, with a single passage through the atmosphere, allows for a faster solution and is hence not only deemed a viable alternative, alone [5, 25, 46, 57, 58] or in combination with aforementioned strategies [52, 56], but even regarded as a potential enabling technology due to the mass savings it allows for [48, 59].

The feasibility of aerocapture for various destinations in the Solar System has been analyzed by creating feasibility charts where the constraints induced by TCW, peak deceleration, peak heat rate on the stagnation point, and total heat load are shown as a function of entry velocity for both the cases of lift and drag modulation [18]. In the case of Mars, where a low circular target capture orbit is considered, results show how aerocapture is feasible with both lift and drag modulation, but the constraints on deceleration (the previously mentioned $5g$) suggest that its feasibility is limited to entry velocities lower than 10 km/s, discouraging the possibility of capturing a high-velocity spacecraft using the atmosphere alone and suggesting this scenario might require some additional propulsive braking.

The mass benefit seems to be a general advantage offered by aerocapture, but it is still necessary to analyze how this declines in cases that differ for the choice of spacecraft or parking orbit. The main parameters that determine mass advantages are the required insertion Δv and the specific impulse of the propulsive stage I_{sp}, as was demonstrated in the case of a manned mission from Earth to Mars and

7

back [19], under the assumption of a *"small and light"* Earth return vehicle. After comparing the scenario where aerocapture is used on both planets to the purely propulsive one, the ratio between the mass at Earth departure in the two cases is calculated and is shown to decrease as $\Delta v/g_0 I_{\text{sp}}$ increases, demonstrating that the mass-saving provided by aerocapture becomes important for increasing Δv. This also means that, when the same propulsive system is in place, Δv becomes the most important parameter in determining mass advantages. The reason is that, while the use of aerocapture implies less propellant mass, it also requires the addition of an extra aeroshell in order to perform the maneuver, which, especially considering the heat-resistant materials it must be made of, might entail a non-negligible mass. If the extra aeroshell mass exceeds what has been saved by discarding part of the propellant, aerocapture is not worth implementing.

The dependence on Δv is confirmed when analyzing the effect of entry velocity and parking orbit choice. By comparing the mass delivered with aerocapture to that delivered with aerobraking or chemical propulsion, it has been shown that aerocapture entails more mass benefits when the target orbit is circular rather than highly elliptical, because of the bigger Δv required to brake into a circular orbit [15]. Additionally, when a range of entry velocities is considered, it has been shown that aerocapture outperforms the purely propulsive scenario at every velocity and outperforms aerobraking for velocities greater than 4 km/s, delivering an increasing payload mass fraction for increasing velocities. Furthermore, aerocapture is shown to be an enabling technology for arrival velocities over 7 km/s, as it represents the only known strategy that can deliver a significant payload mass fraction [18]. In the latter study, the mass fraction for TPS is derived empirically and does not consider the newest materials, such as Heatshield for Extreme Entry Environment Technology (HEEET) or Phenolic-Impregnated Carbon Ablator (PICA), suggesting that mass-benefit advantages might slightly differ when newer technologies are employed. Furthermore, both studies consider uncrewed spacecraft with relatively low masses, suggesting the need for a more specific analysis to be conducted for heavier, crewed spacecrafts.

One of the most important parameters to assess while designing an aerocapture mission is the lift-to-drag ratio L/D. Analyses of different mission scenarios with entry velocities ranging from 6 km/s to 10 km/s show that a minimum L/D of 0.28 is necessary to obtain $TCW > 1°$, which is considered the minimum corridor width to accommodate for the guidance accuracy available at the time [17, 44, 58]. The ideal L/D is identified as ranging from 0.3 to 0.5 [19], to provide adequate control authority and good payload packaging efficiency. By investigating the relation between L/D, TCW, and entry velocity for a manned vehicle employing bank angle modulation [27], the L/D requirements are shown to depend on entry velocity which, when increased, demands an increase in L/D. While the requirement for a minimum L/D of 0.3 is confirmed if no limit to the entry velocity is imposed, it has been shown that if $v_{\text{entry}} > 8.5$ km/s, a minimum L/D of 0.5 is required, and if v_{entry}=10 km/s, L/D must be increased to a minimum of 1.5. This result, obtained by numerically integrating the three degrees of freedom equations of motion for a case where the highly elliptical parking orbit has a one Sol (where one Sol corresponds to one Mars day) period, is due to the limit imposed on deceleration, $5g$, suggesting that the required L/D may vary in case a different limit deceleration is considered. The same situation is analyzed with a methodology that only varies for the algorithm used to solve the differential equations, and rather different

results are achieved [24]. In this second analysis, an L/D between 0.4 and 0.5 results enough for entry velocities up to 10 km/s. One main difference between the two analyses is the choice of parking orbit, which is a low circular orbit in the second case. A highly elliptical one Sol period orbit was also taken into consideration [28], stating that an increase in L/D requirements is only appreciable for velocities lower than 7 km/s, thus confirming the previous findings for the 10 km/s case. Another difference between the two approaches is the entry interface that has been considered for the Mars atmosphere, which is 300 km in [27] and 125 km in [28]. Such different results can ultimately be explained either by the different algorithms that have been used or by the sensitivity to entry altitude.

The employment of aerodynamic drag and the expected hypersonic flow field [19] cause substantial heating rates to appear, and it is necessary to evaluate them, as well as the maximum integrated heat on the stagnation point, in order to provide the spacecraft with an adequate TPS capable of guaranteeing its integrity. Various studies have tried to assess the aerothermodynamic environment an aerocapture vehicle would experience on Mars [19, 24, 60]. Through a comprehensive analysis of flow field simulations, conducted for various entry conditions and including computation of convective and radiative heating rates, it has been concluded that, for an aerocapture vehicle having a 20 m effective nose radius and entering with $v_\text{entry} = 7$ km/s, maximum combined heat rates are expected to be around 100 W/cm^2 [19]. A rapid increase is shown to occur when velocities get close to 10 km/s due to the effect of radiative heating, which has little effect at velocities below 6 km/s, but becomes dominant when velocities exceed 8 km/s. These results are valid under the assumption of chemical equilibrium, which is considered to be a valid one after comparison with past studies on chemical species concentration profiles [19].

These conclusions on the intervals of predominance of convective or radiative heating and of maximum heating trend with velocity are confirmed for a range of vehicles having different L/Ds through analytic expressions (both convective and radiative heating are calculated via the empirical equations developed by Tauber [61, 62]) under the assumptions of a fully catalytic cold wall and, again, of chemical equilibrium. Furthermore, it has been shown that vehicles with an L/D of 1.0 experience higher heat loads than those with lower L/Ds, especially due to prolonged heating pulses [24].

Different results were obtained when studying vehicles with smaller nose radii (1 ft and 2 ft, corresponding to 0.30 m and 0.61 m, respectively), where radiative heating has been shown to become comparable with convective heating only for velocities around 12 km/s [60]. At the same time, a study on the influence of nose radius showed how radiative heating becomes increasingly important with an increasing nose radius, explaining why the entry velocity at which radiative heating becomes prevalent can change so much [60]. In this context, convective heating rates were calculated by solving non-similar boundary layer equations, while radiative heating rates were obtained by a solution of the inviscid flow equations coupled with a very detailed radiation model, including atomic line, continuum, and wavelength characterization [60].

Although guidance, navigation, and control are not the focus of this work, it is worth considering what the current state of the art is on the matter of guidance for aerocapture missions because of its possible impact on mission design choices. In the context of aeroassist maneuvers, the main strategies used to control the trajectory of the spacecraft are lift modulation and drag modulation. An optimal

trajectory using lift modulation, as demonstrated analytically [63], should involve a "bang-bang" bank angle profile, first maximizing lift upwards and then downwards. While a downward lift can also be maintained throughout the entire trajectory, this option might lack resilience in the face of trajectory uncertainties [63].

While lift modulation is historically the reference method used to achieve control in atmospheric entry scenarios [64–66] and has already been tested for the Mars Science Laboratory (MSL) aerobraking phase [67, 68], drag modulation has only recently gained attention thanks to its potential to reduce the complexity associated with lift modulation [69]. Feasibility studies on Earth and Mars [70] have shown that drag modulation can provide viable control strategies, especially for high ballistic coefficient ratios. Various configurations, such as single-stage jettison, two-stage jettison, and continuously variable systems, have been explored [71], showing promise for missions to Mars, given its low-density atmosphere that accommodates lightweight inflatable mechanisms. However, only small and light vehicles are considered, leaving crewed missions unexplored. Also, the narrowness of the TCW resulting from numerical simulations implies the necessity for a very good guidance system [70]. Additionally, the effectiveness of drag modulation increases with the adaptability of the reference area, introducing a certain level of complexity to the operation [71].

Comparative analyses between lift and drag modulation revealed that, while lift modulation generally outperforms drag modulation, drag modulation may provide a better TCW for low entry velocities and high apoapsis altitudes [69]. While these results have been numerically tested for various conditions and uncertainties, only a discrete control strategy has been considered for the lift modulation case, as opposed to the continuous bank angle modulation that is traditionally employed, possibly disfavoring it against the drag modulation case [69].

1.4   Overview

This study of the integration between rapid crewed missions and aerocapture begins by defining the concept of rapid missions and the inherent complexities associated with their implementation. Following that, a mission architecture that suits the characteristics of such a mission is defined.

The assumptions and methodology behind the formulation of the interplanetary trajectory are presented, and key concepts are introduced to provide a framework for determining the requisite acceleration and deceleration at Earth and Mars. A spacecraft architecture is then defined, ensuring the accommodation of both astronauts and a robust propulsion system, whose range of high-thrust possibilities is presented. A specific focus is devoted to obtaining the mass of the various elements that constitute the spacecraft.

With the main characteristics of the spacecraft and the interplanetary trajectory in place, the criticality of the aerocapture phase is explored in its dynamics, flow regime, and heating environment, with particular attention to the search for a robust model for radiative heating on Mars. Additionally, limit deceleration loads for the crew are presented and discussed.

The history of spacecraft configurations used to provide the required deceleration during past aeroas-

sist maneuvers is addressed and will lead to the definition of an aeroshield shape inspired by that of the Viking 1 mission to Mars, albeit featuring more modern materials and leaving the definition of the TPS and the shield size for successive determination.

After explaining which strategies are used in the eventuality the aerocapture maneuver necessitates being paired with propulsive braking, results are presented and discussed. Parametric analyses will establish the key constraints to atmospheric entry and provide limitations to some of the entry parameters. Additionally, the possibility and consequences of encountering density uncertainties are assessed.

Once the range of possibilities that allow safe atmospheric entry is defined, the aerocapture phase is linked with the interplanetary one, providing a measure of the required Δv and allowing for the calculation of the Initial Mass in Low Earth Orbit (IMLEO), a parameter which allows the assessment of mission cost and minimum transfer time. An analysis of the contribution of the various components of the spacecraft to the IMLEO will provide insight into the main mass drivers. The IMLEO will then be presented for all propulsion systems, for both the aerocapture and purely propulsive scenarios, in a range of mission times shorter than one year, allowing for comparing the two situations and defining the potential mass benefit of aerocapture.

Chapter 2

Mission Design

2.1 The problem of rapid missions

Space dynamics are governed by the ideal rocket equation, originally formulated by Konstantin Tsiolkovsky in 1903 [11, p. 3,215]:

$$\frac{m_0}{m_f} = \exp\left(\frac{\Delta v}{g_0 I_{\mathsf{sp}}}\right),\qquad(2.1)$$

where m_0 and m_f represent the initial and final mass of the rocket before and after a propulsive burn. This equation determines the change in mass required to achieve the desired change in velocity, representing the amount of propellant needed, depending on the efficiency of the engine. Its exponential nature reveals that an increase in Δv leads to a progressively larger increase in the required propellant mass.

By definition, rapid missions involve high velocities, which require large Δv both to reach and decelerate from. Consequently, a substantial portion of the IMLEO must inevitably be allocated to propellant.

For the outbound segment to Mars, the initial maneuver must not only accelerate the spacecraft itself but also the propellant mass needed for the decelerating maneuver upon arrival. Therefore, it is crucial to minimize the arrival propellant mass as much as possible.

In this context, aerocapture represents a clever strategy to delegate a portion or the entire Δv to the Martian atmosphere, thereby reducing the propellant load and, consequently, the IMLEO. This reduction stems not only from the elimination of a significant fraction of the propellant required upon arrival but also from reducing the propellant needed to impose at the beginning thanks to a reduced IMLEO.

2.2 Mission Architecture

To allow for the crew to get to Mars in the fastest possible way, the crewed segment must carry only what is strictly necessary to transport the astronauts to the Red Planet, so that its mass, the limiting factor of the rocket equation, is the lowest possible. To achieve this goal, the mission design considerations conducted in [1] are adopted and presented in this section.

First, two cargo segments are envisioned to be launched ahead of the crewed mission on a minimum energy trajectory, so that they are available on Mars upon crew arrival.

The first cargo spacecraft will transport all that is necessary for the return journey of the crewed segment: propellant, tanks, consumables, and the Earth re-entry capsule, as well as its own propulsion system, propellant, and tanks for the journey to and from Mars. Additionally, it will also include separate vehicles for transporting the crew to and from the Martian surface and provide a safe environment during their stay there. Those are, respectively, one Mars Ascent Vehicle (MAV) and one Mars Descent Module (MDM) or Surface Habitat (SHAB), depending on the chosen architecture.

The second cargo spacecraft will deliver supplies required during the stay on the surface of the Planet using multiple MDMs. It will also include another MAV or SHAB, as well as all power systems and consumables that will be needed for surface operations. Just like the first cargo spacecraft, it will also include its own propulsion system, propellant, and tanks. Also, in the case In-Situ Resource Utilization is considered, it will also carry the necessary equipment.

By delegating these tasks to the slow cargo spacecraft, the crewed segment is left with the Transit Habitat (THAB), consumables, propellant and tanks for the outbound segment, and the propulsion system.

The THAB serves as a living space for astronauts during interplanetary travel and is equipped with accommodations and subsystems such as the Environmental Control and Life Support System (ECLSS), Thermal Control System (TCS), Attitude Determination and Control System (ADCS), Data Handling and Control System (DHCS), and Electrical Power System (EPS). It is also externally shielded to protect against solar radiation during interplanetary transfer.

All the spacecraft initially depart from a circular 500 km Low Earth Orbit (LEO). The two cargo segments will depart first on a minimum-energy transfer orbit, optimizing propellant use, and arrive to Mars, where they will be placed in a highly elliptical 250 km x 119 450 km orbit.

The crewed segment, on the other hand, will be launched to Mars on a high-energy trajectory and, once reached, placed in the same highly elliptical orbit. Once there, the crew will be able to descend to the surface by using the MDM and perform the required operations there. Upon completing their mission, they will use the MAV to return to the crewed spacecraft, which will have been loaded with the tanks, consumables, and re-entry capsule, so it is ready for the journey back to Earth.

For the scope of this work, only the outbound portion of the crewed segment will be considered, from departure from LEO to arrival to the elliptical orbit around Mars.

As all space missions, this journey consists of a quite complicated subsequence of operations that can be simplified into three main phases of flight: the launch phase, dominated by thrust, the vacuum phase, occurring in the virtual vacuum of space, and the atmospheric entry (or reentry) phase [42, p.XXI].

While the launch phase is outside the focus of this work and the entry phase will be discussed in detail in Chapter 3, it is important to assess the specificity of the vacuum phase, during which the large distance that separates Earth from Mars is covered.

2.3 Interplanetary Trajectory Design

For the purpose of this work, which aims to assess the feasibility of employing aerocapture for rapid crewed missions rather than designing a fully realistic mission, certain assumptions about the interplanetary trajectory will be made. By focusing on the general mission concept and evaluating its viability under various scenarios, the objective is to lay the groundwork for future mission planning efforts, which will undoubtedly delve into the intricate details of space dynamics and planetary alignments.

All orbits, including the interplanetary trajectory, are assumed to be co-planar. The inclination of the orbit of Mars to the ecliptic is 1.848° [4], which is a rather small difference from the 0° that co-planarity assumes.

Additionally, both the orbits of Earth and Mars are assumed to be perfectly circular, despite their slightly elliptical nature, with eccentricities of 0.0167 and 0.0935, respectively [4].

The relative positions of the two planets significantly impact the feasibility of rapid missions, and, when detailed mission design is being conducted, it is imperative to consider a precise time frame. However, for the purpose of this analysis, specific time frames are not considered. Since the mission is designed for the far future and the Earth and Mars will, cyclically, occupy the same relative positions, precise positions at any given time are not crucial for determining mission feasibility.

The interplanetary trajectory comprises two segments: the outbound one, from Earth to Mars, and the inbound one, from Mars to Earth. By determining the optimal duration of both segments in rapid missions, it has been shown that it mostly occurs when they are symmetric, meaning that the same transfer angle is covered in the same amount of time [72]. Although there are cases where the optimal outbound and inbound transfer times slightly differ, the assumption of symmetry will be used for the sake of simplicity and because it is not expected to significantly impact the results.

Finally, all the mentioned Δv are the result of maneuvers that are assumed impulsive.

Under these assumptions, the interplanetary trajectory will be designed by first determining the relative angle θ_{transfer} between Earth and Mars to be covered during the transfer. A Lambert solver will then calculate the required velocities at the two planets, and the patched conics method will be employed to evaluate the necessary Δv.

2.3.1 Transfer angle determination

The transfer angle θ_{transfer} is the angle between the orbital radii of Earth and Mars at departure, which the spacecraft will cover during the outbound segment of the trip. Once the spacecraft arrives at Mars, it will remain there for a defined period of 30 days [1], during which the Mars orbital radius will traverse an angle θ_{stay}. Once the stay is concluded, the inbound segment of the trip will commence, and the spacecraft will return to Earth by covering θ_{transfer}. This sequence, depicted in figure 2.1, enables the calculation of the transfer angle as a function of the total trip time t_{total}:

$$\theta_{\text{transfer}} = \frac{1}{2}(\omega_{\text{E}} t_{\text{total}} - \omega_{\text{M}} t_{\text{stay}}), \tag{2.2}$$
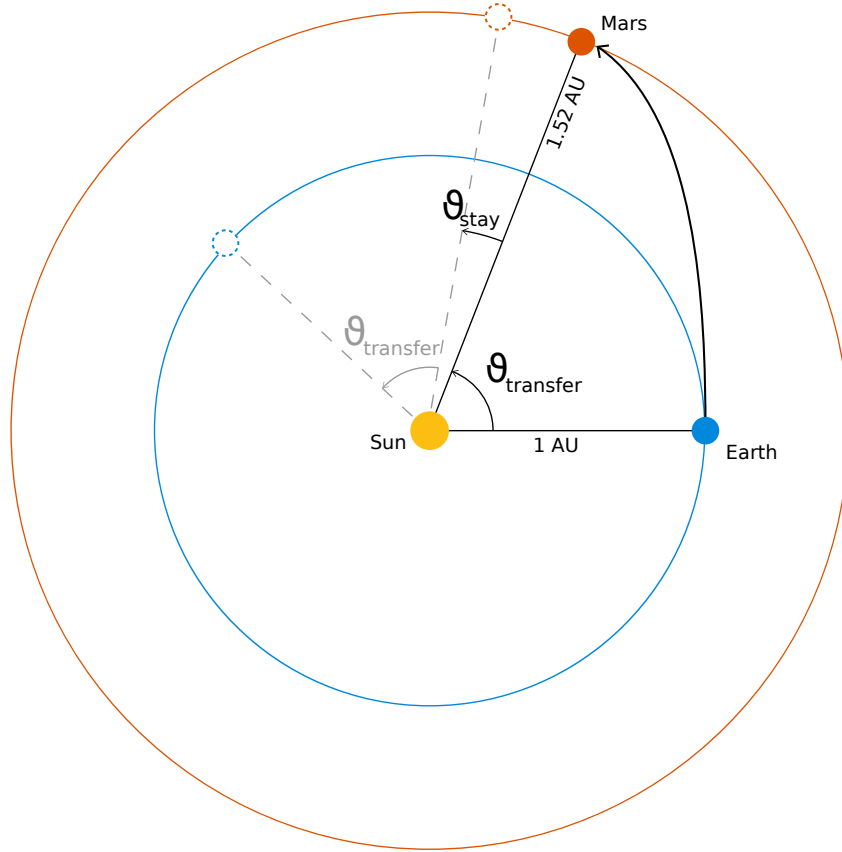
Figure 2.1: Schematic representation of the outbound segment of the trajectory. Hatched planets and radii represent the positions of the planets at the beginning of the inbound segment. The dimensions of the planets are not to scale, but their distances from the Sun are.

where ω_E and ω_M represent the angular orbital velocities of Earth and Mars, respectively, and t_{stay} denotes the duration of the stay on Mars.

2.3.2 Lambert's problem

Lambert's problem seeks to determine the trajectory of a two-body orbit connecting two given points, P_0 and P_f, having position vectors $\mathbf{r}_0$ and $\mathbf{r}_f$, within a specified time interval Δt, assuming gravitational attraction between the bodies is the only force acting on the spacecraft [73, p.238]. The solution to the problem consists of providing the velocity vectors $\mathbf{v}_0$ and $\mathbf{v}_f$ at the respective points, which, along with the position vectors, fully define the initial and final conditions of the trajectory.

In our case, the initial and final points correspond to Earth and Mars, located 1.0 Astronomical Unit (AU) and 1.52 AU away from the Sun, respectively. Under the assumption of coplanarity, their position vectors and orbital velocities are given by

$$\mathbf{r}_E = \begin{pmatrix} 1 \\ 0 \\ 0 \end{pmatrix} \qquad \mathbf{r}_M = \begin{pmatrix} 1.52 \cos\theta_{transfer} \\ 1.52 \sin\theta_{transfer} \\ 0 \end{pmatrix},$$

16

where $\mathbf{r}_E$ and $\mathbf{r}_M$ are the positions of Earth at departure and Mars at arrival, respectively, and

$$\mathbf{v}_E = \sqrt{\frac{\mu_S}{r_E}} \begin{pmatrix} 0 \\ 1 \\ 0 \end{pmatrix} \qquad \mathbf{v}_M = \sqrt{\frac{\mu_S}{r_M}} \begin{pmatrix} -\sin\theta_{transfer} \\ \cos\theta_{transfer} \\ 0 \end{pmatrix},$$

where $\mathbf{v}_E$ and $\mathbf{v}_M$ are the velocities of Earth at departure and Mars at arrival, respectively, and μ_S is the standard gravitational parameter of the Sun.

Once $\theta_{transfer}$ is determined, it is used to calculate the positions of Earth and Mars. These, together with the outbound segment transfer time, serve as inputs for Lambert's problem, whose solution yields the required velocities of the spacecraft relative to both planets, at departure and arrival, required to reach Mars within the specified time frame.

For this work, Lambert's problem is solved by using a solver based on the method developed by Robert Gooding [74], implemented through an algorithm assembled by Jorge Martínez [75].

2.3.3 Patched conics method

Once the velocities at Earth and Mars are determined, they can be compared with the initial velocities of the spacecraft to calculate the necessary Δv. In this work, initial velocities are obtained using the patched conics method, which assumes that within the sphere of influence of each celestial body, its gravitational field dominates, while outside of it, the spacecraft follows an unperturbed Keplerian orbit around the Sun [73, p.396].

The concept of sphere of influence arises from the fact that, although the Sun is the most massive celestial body in the Solar System and its gravitational pull extends across vast distances, the gravity of a planet becomes dominant when a body approaches it closely [73, p.392].

The method of patched conics models the trajectory of the spacecraft as connected segments of conic sections. It assumes that the gravitational attraction of the Sun is negligible inside the sphere of influence of a planet while, once outside this sphere, the orbit becomes heliocentric, and the sizes of the spheres of influence can be disregarded [73, p.396].

Departure from Earth

At Earth, the spacecraft must accelerate from LEO to be placed in a hyperbolic orbit that provides it with the right velocity at infinity $v_{\infty,E}$, represented by the outcome of Lambert's problem $\mathbf{v_0}$ in the geocentric reference frame.

$$v_{\infty,E} = |\mathbf{v_1} - \mathbf{v_E}|. \tag{2.3}$$

Maximum efficiency is obtained if $v_{\infty,E}$ is aligned to the velocity of Earth $\mathbf{v_E}$.

The velocity at the periapsis of the hyperbolic departure orbit $v_{p,E,hyp}$ can be determined by solving
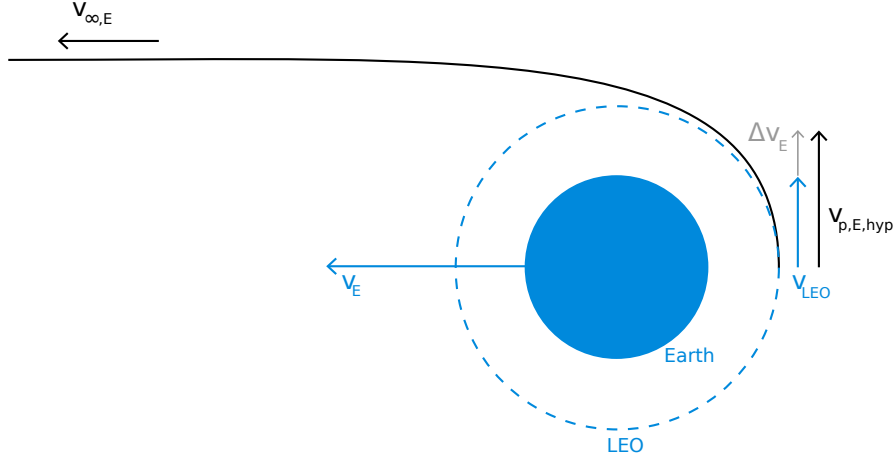
Figure 2.2: Hyperbolic departure orbit.

the conservation of energy equation [73, p.98], which yields

$$v_{\text{p,E,hyp}} = \sqrt{v_{\infty,\text{E}}^2 + \frac{2\mu_\text{E}}{r_{\text{p,E}}}}, \tag{2.4}$$

where μ_E is the standard gravitational parameter of Earth, and $r_{\text{p,E}}$ is the orbital radius at perigee, which in this case corresponds to the orbital radius in LEO.

The required Δv can now be obtained as the difference between $v_{\text{p,E,hyp}}$ and the velocity of the circular orbit:

$$\Delta v_\text{E} = v_{\text{p,E,hyp}} - \sqrt{\frac{\mu_\text{E}}{r_{\text{p,E}}}}. \tag{2.5}$$

Arrival at Mars

At Mars, the situation is symmetric, but it is complicated by the necessity to define the conditions to reach the desired periapsis.

The elliptical target orbit is defined by its periapsis and apoapsis radii $r_{\text{a,M}}$ and $r_{\text{p,M}}$, which allow to determine the velocity at periapsis $v_{\text{p,M,ell}}$ using the conservation of energy equation [73, p. 99]:

$$v_{\text{p,M,ell}} = \sqrt{\mu_\text{M} \left(\frac{2}{r_{\text{p,M}}} - \frac{1}{a_{\text{M,ell}}} \right)}, \tag{2.6}$$

where the semi-major axis $a_{\text{M,ell}}$ is defined as [73, p. 99]

$$a_{\text{M,ell}} = \frac{r_{\text{p,M}} + r_{\text{a,M}}}{2}. \tag{2.7}$$

On the other hand, the hyperbolic approach orbit is not uniquely determined. Its velocity at infinity $v_{\infty,\text{M}}$ results from subtracting the velocity of Mars $\mathbf{v}_\text{M}$ from the output of Lambert's problem $\mathbf{v_2}$:

$$v_{\infty,\text{M}} = |\mathbf{v_2} - \mathbf{v}_\text{M}|. \tag{2.8}$$

18
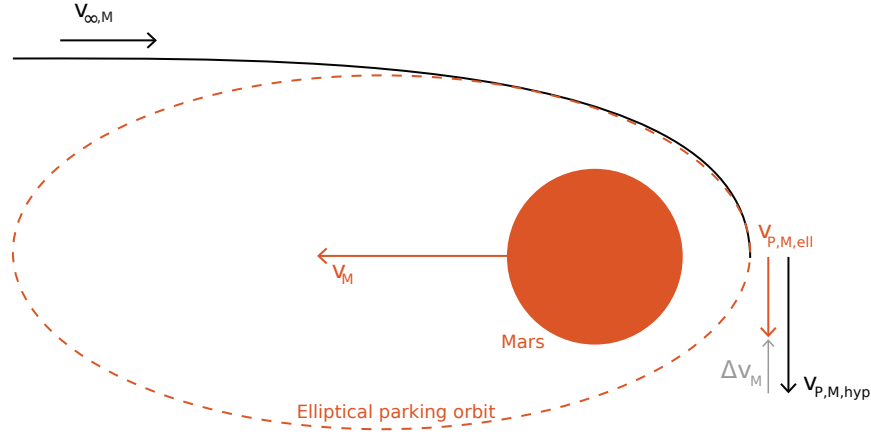
Figure 2.3: Hyperbolic arrival orbit.

The periapsis of the hyperbolic orbit depends on both the magnitude of the velocity at infinity and the angular momentum of the trajectory, which determines the flight path angle [76, p. 226]. Assuming the latter can always be adjusted through negligible thruster actuations, the desired periapsis radius becomes a design parameter, and arrival at the right periapsis altitude can be imposed. By doing so, the velocity at periapsis $v_{\text{p,M,hyp}}$ can be found by imposing the conservation of energy [73, p. 75]:

$$v_{\text{p,M,hyp}} = \sqrt{v_{\infty,\text{M}}^2 + 2\frac{\mu_{\text{M}}}{r_{\text{p,M}}}}. \qquad (2.9)$$

Finally, the required change in velocity at Mars Δv_{M}, which will be used to analyze the purely propulsive scenario, can be found as

$$\Delta v_{\text{M}} = v_{\text{p,M,hyp}} - v_{\text{p,M,ell}}. \qquad (2.10)$$

2.4 Spacecraft architecture

The essence of spacecraft design lies in balancing various functional requirements and the constraints imposed by the challenging space environment. At this preliminary stage, the key considerations for defining the architecture reflect the concepts presented in [1, 72] and can be summarized as follows.

The crewed spacecraft, as outlined in Section 2.2, must include a THAB, consumables, a propulsion system, and tanks. Since consumables and tanks for the return journey to Earth will be replenished on Mars, they only need to be provisioned for the outbound segment of the mission.

The THAB must accommodate the crew, providing them with a habitable space for the interplanetary trip. As each crew member implies an increase in the necessary volume and, consequently, in the mass, a crew of two has been chosen for this mission.

Given the rapid nature of the mission, a significant number of tanks are anticipated, requiring dedicated allocation space. To minimize spacecraft weight for the aerocapture maneuver, these tanks are designed for being jettisoned upon usage, requiring careful positioning to avoid interference with spacecraft operations.

The propulsion system is likely to be particularly large and potentially incorporate multiple engines.

For the aerocapture maneuver, an aeroshield positioned at the forefront of the spacecraft is essential to provide the desired aerodynamic drag and protect the rest of the spacecraft from heating.

Considering these requirements, the envisioned spacecraft takes on a predominantly longitudinal shape, with tanks radially arrayed around the main body. The engine is positioned at the rear, while the aeroshield occupies the front, with the THAB situated directly behind it.

2.4.1 Propulsion system

The choice of propulsion system plays a critical role in determining the amount of propellant needed to achieve a specific Δv. Propulsion efficiency is primarily influenced by three parameters: specific impulse I_sp, thrust T, and thrust-to-weight ratio of the engine T/W [1, 2, 72].

Thrust represents the force exerted by the engine along its axis [73, p. 706]. Depending on the position and orientation of the nozzle, it can be used to accelerate the spacecraft (with the nozzle aligned along the longitudinal axis of the spacecraft in the direction of the velocity vector), decelerate it (with the nozzle aligned along the longitudinal in a direction opposite to the velocity vector), or induce rotation (with the nozzle perpendicular to the longitudinal axis). Assuming engines can be added in parallel, the thrust of the propulsion system scales as a finite multiple of that of a single engine and becomes a design parameter.

Under this assumption, specific impulse and thrust-to-weight ratio emerge as the primary indicators of propulsion system efficiency. The interdependence between those parameters has been investigated, leading to the identification of a list of candidate propulsion systems for rapid Mars missions [1, 72]. This work will examine the same propulsion system scenarios, listed in Table 2.1, to enable a direct comparison between aerocapture and purely propulsive mission strategies.

Case	I_sp, s	T/W
I	3×10^2	190.0
II	1×10^3	75.0
III	3×10^3	32.0
IV	1×10^4	12.6
V	3×10^4	5.4

Table 2.1: Propulsion system case scenarios identified in [1, 72]

The considered cases cover a wide range of Technology Readiness Level (TRL). This parameter indicates the maturity of a given technology, in a range going from one (technologies with only basic research done) to nine (system proved in operational environment) [77]. Specifically, the TRL decreases from case I to case V: while the first one represents the best propulsion system available at the moment, the other ones are all, in some measure, still not mature enough to be used at the current time.

While case I is representative of a chemical engine, cases II and III are non-chemical, meaning they provide thrust without combustion, as in the case of an electric engine. Finally, cases IV and V are

considered advanced, meaning they utilize extremely advanced technologies, such as fusion reactors or electromagnetic drive [78].

2.5 Mass estimation

Estimating the mass of the crewed segment requires the calculation of the mass of its components, namely the THAB, crew, consumables, propulsion system, propellant, tanks, and, for the aerocapture scenario, aeroshield. In this work, we adopt the mass estimation approach outlined in References [1, 72], summarized in the following sections. The mass of the aeroshield will be then calculated in Section 3.5.3.

2.5.1 THAB

During the interplanetary segment, the THAB must provide enough space to ensure livable conditions for the crew and storage for consumables. Its volume V_{THAB} depends on the number of crew members N_{crew} and the duration of the outbound segment d [days]:

$$V_{\text{THAB}} = 1.24 N_{\text{crew}} d^{0.59}. \tag{2.11}$$

The mass of the THAB structure m_{THAB} can be obtained by relating it to the volume:

$$m_{\text{THAB}} = 106.30 V_{\text{THAB}}^{2/3} = 122.61 \left(N_{\text{crew}} d^{0.59} \right)^{2/3}. \tag{2.12}$$

The main structure of the THAB alone is not enough to shield the crew and subsystems from incoming radiation and must be provided with adequate shielding. Assuming a side-wall density of 200 kg/m^2, the mass of the shielding $m_{\text{shielding}}$ is given by:

$$m_{\text{shielding}} = 804.37 \left(N_{\text{crew}} d^{0.59} \right)^{2/3}. \tag{2.13}$$

Subsystems mass, comprehending the ECLSS, ECLSS, ADCS, DHCS, and EPS, total 4010 kg, independently from crew size or transfer duration. Accommodations contribute an additional 670.9 kg.

2.5.2 Crew and consumables

For the crew, an average mass of 82 kg per member is assumed.

Consumables encompass various items essential for the sustenance and well-being of the crew during the transfer. This includes:

- Water for hydration, food re-hydration, and personal hygiene, totaling 2.9 kg per day per crew member.

- Provisions for food, oxygen, and lithium hydroxide, amounting to 2.39 kg, 0.82 kg, and 1.75 kg per day per crew member, respectively.

- Water and oxygen tanks, contributing with an additional 1.78×10^{-2} kg and 0.19 kg per day per crew member.

- Personal stowage, allocating a total mass of 182.50 kg.

- Medical supplies, estimated at 51.63 kg per crew member.

- Hygiene supplies, amounting to 0.31 kg per day.

- Cleaning supplies, accounted for at 1.81 kg per day per crew member.

Overall, the total mass of consumables $m_{consumables}$ amounts to:

$$m_{consumables} = 9.88 N_{crew} d + 51.63 N_{crew} + 0.31 d + 182.5. \tag{2.14}$$

2.5.3 Propulsion system

The propulsion system can be divided into its main components: the engine (or engines), propellant, and tanks.

The mass of the engine m_{engine} is calculated by relating it to the thrust T and to the thrust-to-weight ratio T/W [79]:

$$m_{engine} = \frac{T}{g_0 \left(T/W\right)}. \tag{2.15}$$

Estimating propellant mass is crucial yet complex, as it heavily depends on the assumptions made and the level of precision that is aimed for. Theoretically, propellant mass can be estimated using the ideal rocket equation (2.1). However, this equation is, as its name says, ideal, as it does not account for many of the aspects that space propulsion involves. While it is indeed a useful instrument for preliminarily assessing the required propellant mass, it might provide a rather optimistic view of the problem. The ideal rocket equation assumes a rocket moving in a vacuum and gravity-free space, where the thrust is assumed to be constant and to be the only force acting on the spacecraft [80, ch. 3.7]. While these assumptions will be maintained, the propellant is estimated through a modified rocket equation that accounts for tank jettison and burn losses [79]:

$$\frac{1}{1 - \epsilon_t} \frac{m_{pr}}{m_{pl}} = \exp\left(\frac{1}{1 - \epsilon_t} \frac{\Delta v}{g_0 I_{sp}} \left(1 + \frac{1}{24} \frac{\mu}{r^3} \left(\frac{g I_{sp}}{T} m_{pr}\right)^2\right)\right) - 1, \tag{2.16}$$

where ϵ_t is the structural factor of the tanks, m_{pr} is the propellant mass, and m_{pl} is the payload mass. Unlike the ideal rocket equation, this equation does not provide a solution for every combination of parameters as it presents an asymptote that determines the maximum achievable Δv for a given engine [79].

The mass of the tanks, assumed in an infinite number, is incorporated in the modified rocket equation through their structural factor.

This chapter outlines the mission and spacecraft architecture, presenting a potential approach for implementing a rapid mission to Mars. The interplanetary trajectory is particularly crucial as it determines the required Δv, which will then be used in Equation (2.16) to calculate the propellant masses at departure and arrival. Additionally, the mass estimation considerations provided will enable the determination of the masses for all other spacecraft components. The principles delineated in this chapter apply to both purely propulsive and aerocapture scenarios. However, the latter requires additional considerations on the atmospheric entry environment, which will be discussed in detail in Chapter 3.

Chapter 3

Atmospheric entry phase

Atmospheric entry (or reentry) typically represents the final phase of a space mission, as it often implies the landing of the spacecraft on its destination planet. In the case of aerocapture, though, the entry phase does not coincide with the end of the mission.

This phase begins as the vehicle crosses the atmosphere border. Since identifying a clear edge is impossible for a gassy body like the atmosphere, its beginning can be defined as the point where atmospheric drag becomes significant, as opposed to the theoretical vacuum that characterizes space flight in vacuum [76, p. 2-3].

During the entry phase, the spacecraft is subject to a combination of aerodynamic, gravitational, and inertial forces that alter its trajectory. Furthermore, the interaction with atmospheric gasses has significant effects on the heating of the spacecraft surfaces [76, p. 4; 42, p. xxi]. These effects become increasingly important as the spacecraft descends, mainly due to an increase in density that is typical of all atmosphere-carrying bodies [42, p. xxi; 39].

3.1 Atmospheric entry equations

The atmosphere of Mars is intersected during the hyperbolic arrival orbit at the planet discussed in Section 2.3.3. Before focusing on atmospheric conditions, it is important to first determine the atmospheric entry velocity $\mathbf{v}_{\text{entry}}$. Its absolute value, v_{entry}, can be obtained by imposing the conservation of energy at atmospheric interface:

$$v_{\text{entry}} = \sqrt{v_\infty^2 + \frac{2\mu_{\text{M}}}{r_{\text{atm}}}}, \tag{3.1}$$

where $r_{\text{atm}} = R_{\text{M}} + h_{\text{atm}}$, with R_{M} being the radius of Mars and h_{atm} the altitude where the atmospheric interface is assumed to start having a dynamic effect (in this case, 125 km). The flight path angle of $\mathbf{v}_{\text{entry}}$ is crucial in determining overshoot and undershoot trajectories, as discussed in Section 1.4.

For the continuation of this work, the assumption of planar entry is made. This assumption implies confining the motion of the spacecraft to a plane containing its radius, velocity vector, and the center of the planet [76, p. 58]. As can be seen in Figure 3.1, the position and orientation of the spacecraft are defined by its radial distance from the center of the planet r (or its altitude $h = r - R_{\text{planet}}$) and its velocity
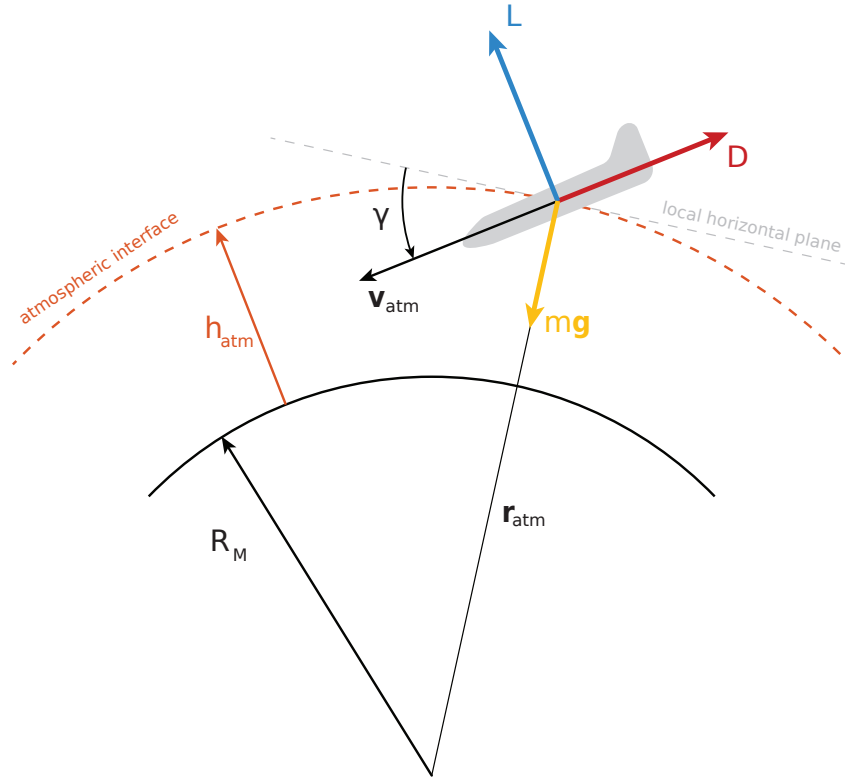
Figure 3.1: Planar entry conditions.

$\mathbf{v}$, defined by its absolute value v and flight path angle γ. Assuming the specific longitude and latitude of the vehicle are negligible for this analysis, its dynamics are defined by three equations [76, p. 63]:

$$\dot{r} = v \sin \gamma, \tag{3.2}$$

$$\dot{v} = -\frac{D}{m} - g \sin \gamma, \tag{3.3}$$

$$v\dot{\gamma} = \frac{L}{m} - g \cos \gamma + \frac{v^2}{r} \cos \gamma, \tag{3.4}$$

where m is the mass of the vehicle and lift and drag L and D are defined as:

$$L = \frac{1}{2} \rho A C_{\mathsf{L}} v^2, \tag{3.5}$$

$$D = \frac{1}{2} \rho A C_{\mathsf{D}} v^2. \tag{3.6}$$

Those two parameters generally depend on the angle of attack, the Mach number M, and the Reynolds number Re, but in the case of hypersonic flight that characterizes the mission considered (refer to Section 3.3), they become a function of the angle of attack only [76, p. 64].

Equations (3.2), (3.3), and (3.4) imply that, under the specified assumptions, the trajectory of the spacecraft within the atmosphere depends on its mass, reference area, atmospheric density, and aerodynamic coefficients C_{L} and C_{D}. The mass of the spacecraft is given by the considerations done in

Section 2.5, and is hence not a design parameter. Atmospheric density, while given by the specific planet, can be modulated by diving deeper or shallower into the atmosphere. The main design parameters, though, are the aerodynamic coefficients and reference area, which are, in a first analysis, a function of the size and shape of the aeroshield only [81, p. 110]. Thus, it is mainly by acting on these that the spacecraft trajectory can be influenced and, consequently, its capture can be ensured.

In the present work, the atmospheric entry phase is analyzed by using the Aerocapture Mission Analysis Tool (AMAT) [82] developed by Athul P. Girija. This software is used to provide the overshoot and undershoot boundaries that ensure capture is obtained, given the entry conditions and vehicle characteristics. Additionally, it is used to obtain the acceleration and heating profiles for a given trajectory.

3.2   Mars Atmosphere

The study of the atmosphere of Mars has been, and still is, the subject of numerous studies and missions [83, ch. 1-3]. Just like that of Earth, it is not an immobile and unchanged entity, but the result of billions of years of ongoing evolution [83, ch. 2]. Additionally, both its composition and thermodynamical properties are subject to latitudinal and seasonal variations [84, p. 1].

Currently, the atmosphere of Mars consists of approximately 95% carbon dioxide (CO_2), 2.7% nitrogen (N_2), 1.6% argon (Ar), and traces of other gases [83, p. 16; 76, p. 164]. Its composition, temperature, and gas properties vary across three distinct layers: lower, middle, and upper atmosphere [76, p. 171; 83, p. 42].

The lower atmosphere extends from the surface up to approximately 40 km altitude. In this region, pressure, temperature, and density decrease with altitude, and are greatly influenced by seasonal variations and dust storms [76, p. 172]. CO_2, the predominant component, acts as a powerful greenhouse gas, blocking infrared radiation from escaping from the surface to space, and it varies seasonally with the sublimation and condensation of the ice-cemented dust layers composing polar caps [76, p. 144, 172]. Dust storms appear when the longitudinal differences in pressure and temperature generate strong winds capable of moving large quantities of dust, largely present on the surface of the Red Planet due to lack of liquid water and past rock erosion [76, p. 173]. Just like CO_2, dust absorbs energy at visible and infrared wavelengths, affecting local climate and atmospheric dynamics [83, p. 295; 76, p. 172]. The middle atmosphere, extending from about 40 km to 100 km altitude, experiences significant temperature variations due to CO_2 cycles, but averagely decreases with altitude and remains generally cooler compared to the lower atmosphere [83, p. 41-43; 76, p. 172]. In contrast, the upper atmosphere, spanning beyond 100 km altitude, displays temperatures that increase with altitude and mainly vary depending on solar activity [76, p. 172; 83, p. 42]. Unlike temperature, density decreases exponentially with altitude along the three layers, averaging around 1% of that of Earth, as depicted in Figure 3.2 [39].
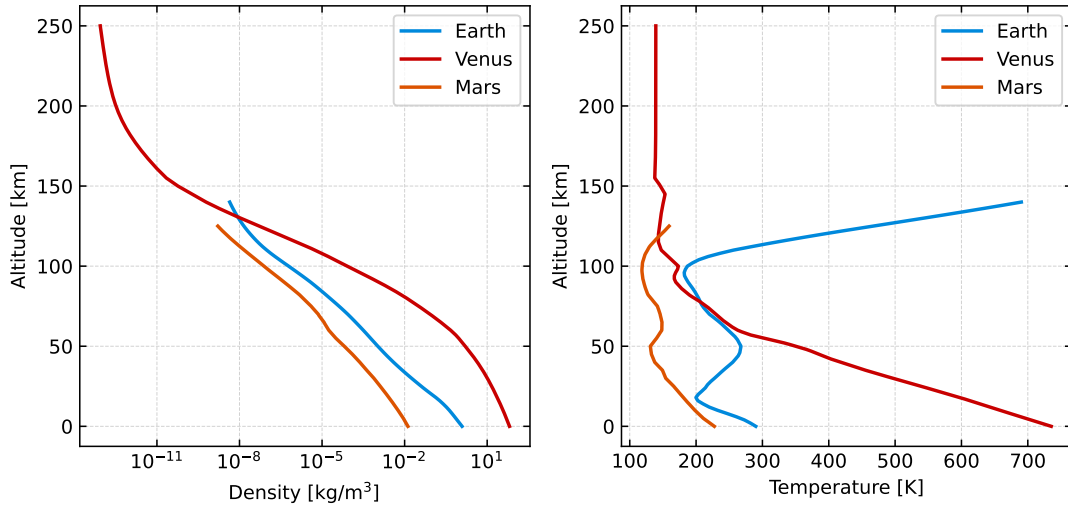
Figure 3.2: Mars-GRAM mean density and temperature as a function of altitude for the atmosphere of Mars. The averaged profiles for Earth and Venus derived from Earth-GRAM [82, 86] and Venus-GRAM [82, 87] are also shown for comparison.

3.2.1 Atmospheric model

Planetary atmospheres consist of a mixture of gases that can significantly influence the aerodynamic heating experienced by entry vehicles due to gas dissociation at the bow shock wave of the vehicle. Their impact on aerodynamic drag, though, is generally negligible compared to atmospheric density [40, p. 1], which emerges as the main parameter to precisely model.

The Mars - Global Reference Atmospheric Model (GRAM) developed by NASA [85] is currently the most comprehensive atmospheric model available. It has been used to plan the aerobraking operations of many of the last Mars aerobraking missions [85], as it provides detailed data on atmospheric density, temperature, pressure, winds, and composition depending on time, latitude, longitude, and dust level. While offering exceptional accuracy, its complexity makes it unsuitable for preliminary analysis such as that discussed hereby. Instead, averaged profiles of density, temperature, pressure, and speed of sound as a function of altitude are enough for assessing preliminary aerocapture feasibility and benefits [12, p. 65,110], hence the averaged Mars-GRAM profiles provided by AMAT are used in the present work.

By eliminating any dependence on longitude or latitude the assumption of spherical symmetry is made, meaning that atmospheric density is a function of altitude only and that the oblateness of the planet or its atmosphere is ignored [40, p. 1-2]. Although significant, this assumption greatly simplifies the analysis and is hence justifiable for a preliminary analysis [40, p. 1-2]. Another assumption of this model is that of a non-rotating atmosphere. For Mars, at the relatively low altitudes where aerocapture occurs, the atmosphere rotates with an angular velocity approximately equal to that of the planet [40, p. 1-3], but its contribution to the relative speed of the flux that passes an entry vehicle is so low it can, again, be ignored in preliminary analyses [40, p. 1-4].

28

3.3 Hypersonic flow

In fluid dynamics, the local Mach number is a dimensionless parameter used to evaluate compressibility effects within a fluid flow regime. It is defined as the ratio of the local flow velocity u to the velocity of sound c in the same medium [88, p. 96]:

$$\text{M} = \frac{u}{c}.$$ (3.7)

The flow regime is characterized based on Mach number [88, p. 98]:

- M < 0.3 Incompressible flow;

- $0.3 <$ M < 0.8 Subsonic flow;

- $0.8 <$ M < 1.2 Transonic flow;

- $1.2 <$ M < 5.0 Supersonic flow;

- M > 5.0 Hypersonic flow.

As a body moves through a fluid, it generates pressure waves. When M < 1 they propagate radially around the body, which eventually encounters those that moved ahead of it [88, p. 97]. However, when M ≥ 1, pressure waves form an envelope around the body, leading to the formation of shock waves.

If the half angle at the leading edge of the body Θ is less than a critical angle Θ_{max}, which depends on the Mach number, the body is considered sharp. In this case, the resulting shock wave is called an oblique shock wave, as it is attached to the leading edge and then continues as a conical shape around it, characterized by the Mach angle β_{Mach}, given by [89, p. 81]:

$$\sin \beta_{Mach} = \frac{1}{\text{M}}.$$ (3.8)

If $\Theta > \Theta_{max}$ the body is considered blunt, the shock wave is a detached bow shock, and it assumes a curved configuration near the leading edge, approaching the Mach angle asymptotically. This case is known as a bow shock wave [89, p. 86] and is depicted, alongside the oblique shock wave, in Figure
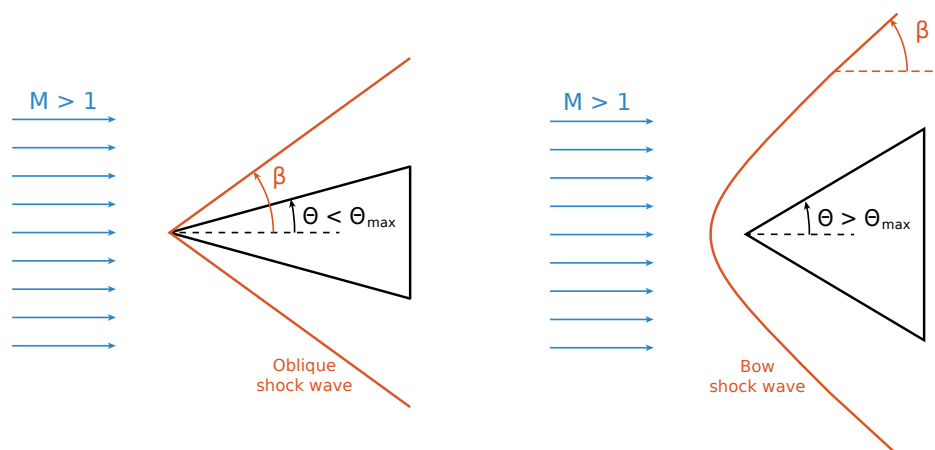

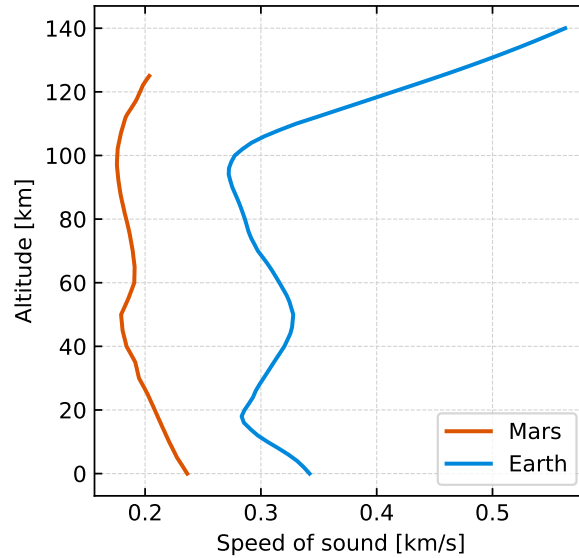Figure 3.3: Oblique and bow shock waves.

Figure 3.4: Speed of sound as a function of altitude computed from average Mars-GRAM [82, 85] and Earth-GRAM [82, 86].

3.3. This scenario also applies to bodies with a curved front part, where Θ approaches $90°$, making the formation of a bow shock wave common in such cases [89, p. 86].

The drag and heat generated in the case of a bow shock wave are significantly bigger than that generated for an oblique shock wave, hence blunt bodies are preferred when the main objective is to quickly decelerate, such as in the case of reentry capsules [89, p. 87].

On Mars, the average speed of sound reaches a maximum value of approximately 0.236 km/s at ground level, as illustrated in Figure 3.4. Considering the high velocities at which the planetary atmosphere will be approached ($v > 6$ km/s) the flight regime will most certainly be hypersonic for the entire duration of the aerocapture phase. Thus, defining the characteristics of this type of flow and the consequences of a shock wave is fundamental.

In hypersonic flow, as the Mach number increases beyond supersonic levels, the flow pattern around the moving body undergoes significant compression, causing its lateral extent to shrink to smaller Mach angles. As a consequence, gas masses accumulating along the surface of the body generate local velocities of sound sufficiently high to maintain finite gas density and prevent the thickness of the flow layer from diminishing to zero. This transition marks the realm of hypersonic flow, where the influence of the undisturbed Mach number diminishes, and the thermodynamic properties of the gas, particularly at high temperatures, become prevalent. The proximity of the shock wave to the surface of the leading edge of the body generates significant interaction with the boundary layer, whose extreme temperatures render the ideal gas hypothesis invalid [40, p. 1-14].

The Knudsen number Kn is defined as the ratio of the mean free path between the particles of the flow λ to the characteristic length of the body L_c [81, p. 20-21]:

$$\text{Kn} = \frac{\lambda}{L_c}.$$

(3.9)

This parameter indicates the rarefaction of the gas and allows for distinguishing between different flow regimes [90, p. 16]:

- Kn ≤ 0.01 Continuum flow;

- $0.01 \leq$ Kn ≤ 0.1 Slip flow;

- $0.1 \leq$ Kn ≤ 10 Transitional flow;

- Kn ≥ 10 Free molecular flow.

Free molecular flow best describes the vicinity of a hypersonic shock wave, where the mean free path length tends to infinity, and the common description of the fluid through Navier-Stokes equations is not valid anymore. Instead, the Newtonian flow model, developed by Isaac Newton, is more appropriate [40, p. 1-15; 89, p. 84]. This model, developed before the existence of shock waves was even discovered [40, p. 1-15], neglects the thermodynamic movements of fluid particles and assumes the free path length to be infinite [89, p. 26]. In that case, the corresponding pressure coefficient C_P, used to determine the drag and lift coefficient, depends only on the angle δ between the flow direction and the surface normal [40, p. 1-17]:

$$C_P = 2 \sin \delta. \tag{3.10}$$

3.3.1 Aerodynamic coefficients calculation

The main aerodynamic coefficients, the lift coefficient C_L and drag coefficient C_D, must be evaluated to determine the drag and lift forces that act on the spacecraft during its atmospheric passage. They are defined from Equations (3.5) and (3.6) [91, p.10] as

$$C_L = \frac{L}{\frac{1}{2}\rho v^2 A} \qquad \text{and} \qquad C_D = \frac{D}{\frac{1}{2}\rho v^2 A}. \tag{3.11}$$

They provide a non-dimensional measure of the aerodynamic forces and, although mainly indicative of the geometric properties of the body, generally also depend on the flow conditions.

In a hypersonic regime, however, they are independent of the Mach number and can be derived from the integration of the pressure coefficient (see Equation (3.10)) over the body surface [81, p. 110].

For the present analysis, aerodynamic coefficients have been computed according to Newtonian theory using the software MC-New [92], which employs a meshless Monte-Carlo integration method. Specifically tailored for bodies immersed in hypersonic flow fields, MC-New eliminates the need for extensive computational mesh generation, typical of panel methods, by decomposing the body into simple geometries, determining intersections between them, and computing aerodynamic coefficients as the sum of local pressure components on randomly distributed sample points on the surface.

3.4   Heating

During interplanetary travel, in an atmosphere-free environment, the primary sources of heating are solar radiation, either direct or reflected from a planet, and infrared radiation emitted by the planet itself [93, p. 22]. These factors necessitate a specific TPS design, which is included in the considerations of Section 2.5.1. The heating encountered during atmospheric entry, however, arises due to different causes and therefore requires a specific approach.

During atmospheric entry, heating occurs due to the dissipation of the initial kinetic and potential energy of the vehicle through two distinct heat transfer mechanisms: convection and radiation [94, p. 299]. Convective heat transfer occurs as the atmospheric gas bathes the surface after being heated by the passage through the bow shock [94, p. 299; 89, p. 87]. Conversely, radiative heat transfer arises from the radiative emission of the high-temperature gas in the shock layer and only becomes significant in hypersonic flows [94, p. 299; 89, p. 87]. High temperatures in the shock layer cause molecular dissociation and atomic ionization, leading to radiation from subsequent recombinations. During Mars entry, the shock layer primarily consists of carbon monoxide (CO), which dominates the radiative mechanism, atomic oxygen (O) and carbon (C), as well as small amounts of cyanide (CN) and argon (Ar) [19].

Peak aerodynamic heating typically manifests in the stagnation point region, corresponding to the leading edge point where the flux hits the surface perpendicularly [94, p. 299]. The turbulent flow along the rest of the surface can, under some specific circumstances, produce a comparable or even greater heat flux. Nevertheless, only the heating of the stagnation point of the shield is considered in this analysis, as the primary objective is to determine whether the magnitude of the heating at this point can be withstood by current technologies. A comprehensive analysis of the phenomenon would require techniques, such as Computational Fluid Dynamics (CFD), which are beyond the scope of this work.

In spacecraft design, two types of thermal load must be managed: the instantaneous heat rate q [W/cm^2], and the cumulative heat load Q [J/cm^2] [94, p. 298]. The first one must be kept below a certain maximum limit specific to the material being used to prevent its temperature from reaching unacceptable levels [95, p. 129]. The latter, on the other hand, relates to the mass fraction f_{TPS} of the TPS over the total entry mass following the relation [12, p. 107; 96]

$$f_{\text{TPS}}(\%) = 0.091 Q^{0.51575}. \tag{3.12}$$

Therefore, while the heat rate has a fixed maximum value determined by the chosen TPS material, the heat load can be counteracted by increasing the TPS mass fraction, although its implications on total mass suggest it must still be kept under a reasonable value.

In this analysis, the stagnation point heat rate is computed as the sum of the convective and radiative contributions and then integrated on the surface of the shield to provide the corresponding stagnation point heat load.

3.4.1 Convective heating model

Convective heating, in the present analysis, is computed using the empirical model implemented in AMAT [12, p.106], based on the relation developed by Sutton and Graves [97]. The convective heat rate q_c is given by

$$q_c = K \left(\frac{\rho_\infty}{R_N} \right)^{0.5} v^3,$$ (3.13)

where K is the convective heat transfer coefficient [kg/(s m$^{3/2}$atm$^{1/2}$)], ρ is the freestream atmospheric density [kg/m^3], R_N is the effective nose radius of the vehicle [m], and v is the freestream velocity [m/s].

The convective heat transfer coefficient is a constant that depends on the mean atmospheric composition of the planetary atmosphere. Sutton and Graves [97] provided equations for deriving it for several simple gases and gas mixtures. For simple gases

$$K = \frac{0.1106}{\sqrt{\sum \frac{c_i}{M_i \gamma_i}}},$$ (3.14)

where c_i is the mass fraction, M_i the molecular weight, and γ_i the transport parameter of the species i. For gas mixtures

$$K = \frac{1}{\sqrt{\sum \frac{c_i}{K_i^2}}},$$ (3.15)

where K_i represents the heat transfer coefficients of the gases composing the mixture. In AMAT, the value of K for Mars is obtained from a different source, [98], yielding $K = 1.8980 \times 10^{-4}$.

3.4.2 Radiative heating model

The computation of radiative heating during Mars entry poses significant challenges, especially for the high velocities considered in this analysis. Contrary to convective heating, AMAT does not provide a radiative heating model for Mars, deeming it negligible for entry scenarios [12, p. 107]. However, both the author and other sources [19, 24, 60] agree on the fact that radiative heating is only negligible at low velocities, and becomes not only relevant but prevalent on convective heating when a certain minimum velocity is reached.

Given the focus on high-velocity atmospheric entry in this analysis, dismissing radiative heating as negligible was deemed unacceptable. An extensive literature review uncovered two radiative models for Mars entry: one was developed by Tauber and Sutton [62], and the other by West and Brandis [99]. Additionally, correlations for radiative heating on Venus [100] were considered due to the similar composition of the atmosphere of the two planets [20].

The Tauber-Sutton correlations were derived using a multiband radiative model under the assumption of thermochemical equilibrium. Results are computed for nose radii ranging from 1 m to 23 m and for velocities from 6 km/s to 9 km/s. The resulting expression for calculating the radiative heating rate q_r [W/cm^2] results [62]

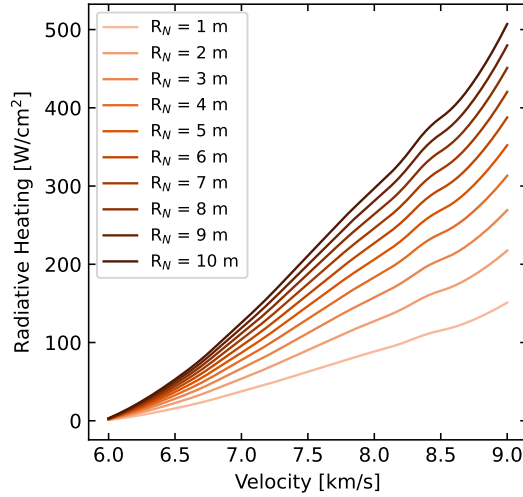$$q_r = C R_N^a \rho^b f(v),$$ (3.16)

Figure 3.5: Tauber-Sutton model over its range of validity for the density of Mars at 30 km of altitude.

where, for the Martian atmosphere,

$$C = 2.35 \times 10^4, \qquad a = 0.526, \qquad b = 1.19, \qquad (3.17)$$

and $f(v)$ are tabulated values that vary with the flight velocity v. This model, depicted in Figure 3.5, was validated against a radiative heating model for Venus entry [101] considering a 90% CO_2 and 10% N_2 composition, as well as different pressures, densities, and nose radii. Despite the numerous differences between the two, the models exhibit good agreement, differing by a maximum of 30%.

The West-Brandis model [99] is based on CFD calculations conducted in a range of velocities ranging from 2 km/s to 8 km/s and nose radii from 1 m to 20 m. Two versions of the model are presented: an exponential relation based on the physics of the problem and a polynomial regression of the data set, both distinguishing the freestream velocity as ranging from 2 km/s to 6 km/s and from 6 km/s to 8 km/s. The exponential relations calculate radiative heating as a function of effective nose radius, post-shock equilibrium CO, CN, and CO_2 mass fractions, post-shock equilibrium temperature, and post-shock equilibrium density. The polynomial regression, on the other hand, yields

$$q_{\mathrm{r}} = e^{f(v, ln(\rho), R_{\mathrm{N}})}, \qquad (3.18)$$

where $f(v, ln(\rho), R_{\mathrm{N}})$ is a fourth-order polynomial that varies with the freestream velocity, freestream density, and effective nose radius. Because a fourth-order expansion of three variables has 35 coefficients, this equation is quite lengthy, and the full list of coefficients is not presented here. The two models were compared to the CFD predictions and the Tauber-Sutton model, showing a better agreement of the polynomial regression over the exponential fit and proving an overall better fit than the Tauber-Sutton model. Additionally, the model was applied to the atmospheric entry of Mars Pathfinder, resulting in a slight underestimation of the radiative heating resulting from a CFD analysis of the problem, but confirming the better agreement of the polynomial fit over the exponential one and of both of them to the Tauber-Sutton relation. Due to the demonstrated accuracy of the polynomial regression and the ad-
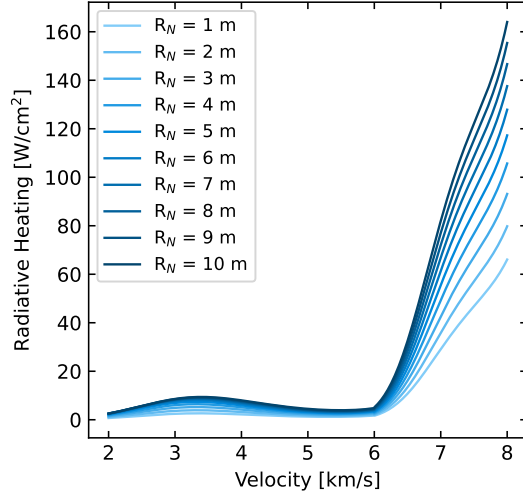
Figure 3.6: West-Brandis model over its range of validity for the density of Mars at 30 km of altitude.

ditional complication introduced by the necessity of calculating post-shock equilibrium conditions, the polynomial regression has been chosen to represent the West-Brandis model in this work. The results over the considered range are illustrated in Figure 3.6.

The last radiative model considered was originally developed for Venus [100]. Venus and Mars have very similar atmospheric compositions, both predominantly CO_2 (96.0% for Mars and 96.5% for Venus), with smaller percentages of N_2 (1.9% for Mars and 3.5% for Venus) and other gasses (1.9% of Ar for Mars and even smaller fractions of other gasses for both planets) [102]. Because of the thicker atmosphere of Venus (as illustrated by Figure 3.2, it is averagely a thousand times denser than that of Mars), the main concern with using this model is the possibility that it has only been tested for higher densities. Nevertheless, the density range in the atmosphere of Venus covers the whole density range present in that of Mars, and the extension of this model has already been recommended in the past [18]. The mentioned model was developed by Tauber based on a computing program that solves the coupled thin shock-layer equations of mass, momentum, energy, and non-grey radiation [101]. Stagnation point radiative heating is calculated as

$$q_r = 3.07 \times 10^{-48} v^{13.4} \rho^{1.2} R_N^{0.49} \quad \text{for} \quad 10000 \leq v \leq 12000, \tag{3.19}$$

$$q_r = 1.22 \times 10^{-16} v^{5.5} \rho^{1.2} R_N^{0.49} \quad \text{for} \quad 8000 \leq v \leq 10000, \tag{3.20}$$

$$q_r = 3.33 \times 10^{-34} v^{10.0} \rho^{1.2} R_N^{0.49} \quad \text{for} \quad v < 8000. \tag{3.21}$$

A graphical representation of it can be seen in Figure 3.7. The main advantage of this model, and the reason for its inclusion despite it not being developed for Mars, is the wide range of velocities it was tested over, compared with the limited range of the Tauber-Sutton and West-Brandis models.

Given that all the previously discussed models have an upper-velocity limit that is likely to be surpassed in a rapid mission, the prospect of extrapolation became necessary to address this potential scenario. The first step was to determine the most suitable extrapolation approach. An old technical pa-
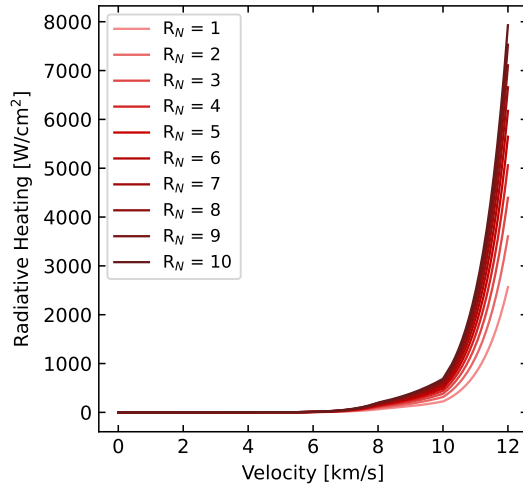
Figure 3.7: Venus model over its range of validity for the density of Mars at 30 km of altitude.
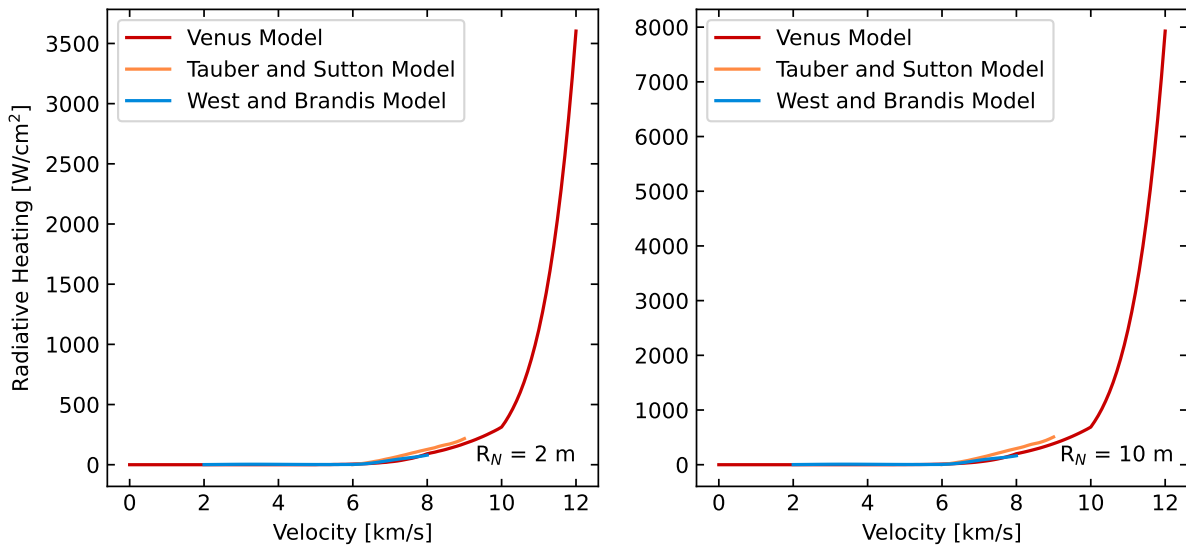
Figure 3.8: Comparison of the three radiative models for varying nose radii, for the density of Mars at 30 km of altitude.

per provided a similar extrapolation for the Martian atmosphere, assuming a proportionality to v^8 [103] due to its good fit to experimental data up to 8 km/s, though acknowledging that this dependence might change at higher velocities. For the Venusian atmosphere, an extrapolation to v^{10} has been proposed [104] for higher velocities.

A comparison of the three models can be observed in figure 3.8 for varying nose radii. It is evident that, for each nose radius, the Tauber-Sutton model tends to overestimate q_r compared to the other two. Consequently, the decision was made to use the Tauber-Sutton model within its range of applicability and the Venus model beyond it. Given that the Venus model utilizes a velocity exponent of 13.4, surpassing the proposed extrapolations, it offers a conservative approach for addressing higher velocities. As a result, if extrapolation to higher velocities is required, the Venus model will be extended accordingly.

36

3.5 Aeroshield design

The atmospheric entry phase is a particularly delicate and crucial moment of a space mission, demanding the addition of a specifically designed aeroshield. This component serves a dual purpose: decelerating the spacecraft and mitigating the intense heating generated by the interaction with the atmosphere.

Deceleration is mainly driven by the shape of the aeroshield, which determines the drag coefficient of the entry body, thereby influencing the efficiency of an aeroassist maneuver.

Furthermore, an aeroshield must be provided with an efficient TPS to handle the heating environment. Its material sets the threshold for the maximum allowable heat rate, while its mass is linked to the maximum expected heat load, as outlined in Equation (3.12).

Since aerocapture has never been performed, the only examples of aeroassist maneuvers available for analysis are aerobraking ones. The first aerobraking test occurred on Earth during the Hiten mission launched in 1990 [34]. Subsequently, the Magellan mission at Venus, launched in 1993, became the first space mission to employ aerobraking [32]. The Magellan spacecraft successfully lowered its apoapsis during a 70-day aerobraking that was conducted at altitudes ranging from 135 to 150 km [32]. The atmospheric density of Venus at these altitudes resembles that of Mars at the same height (see Figure 3.2), so the encountered heating environment was favorable enough to allow the spacecraft to use its solar panels to brake, avoiding the need for a dedicated aeroshield.

Following the success of the Magellan mission, aerobraking became a regular practice for numerous Mars missions. To date, four examples can be cited: Mars Global Surveyor (MGS) in 1996 [35], Mars Odyssey in 2001 [36], Mars Reconnaissance Orbiter (MRO) in 2005 [37], and TGO in 2017 [38]. Additionally, another mission to Venus employed aerobraking, the Venus Express [33], launched in 2005.

Following the Magellan mission heritage, all of these spacecraft employed their solar panels [33, 35, 36, 38], or a combination of solar panels and antennas, in the case of MRO [37], as braking surfaces. This choice allowed for saving the mass that would have otherwise been dedicated to an aeroshield. However, this strategy was only feasible because of the high altitudes that were reached by these spacecraft, which descended to a minimum altitude of about 95 km on Mars and 135 km on Venus.

These altitudes correspond to densities reaching approximately 10^{-7} kg/m^3 at their highest. In contrast, the altitudes expected from an aerocapture maneuver on Mars can be as low as 30 km [24, 25], where densities can reach an order of about 10^{-4} kg/m^3. Furthermore, entry velocities for aerocapture, performed directly from a hyperbolic orbit rather than an elliptical one, are generally much higher.

The combination of higher densities and entry velocities implies heavier thermal loads on the spacecraft, which solar panels alone are unlikely to withstand. Consequently, aerocapture missions typically require dedicated aeroshields.

3.5.1 Shape choice

Due to the absence of direct aerocapture experience and the lack of dedicated aeroshields for aerobraking missions, previous aerocapture design studies often relied on aeroshields derived from entry

37

probes.

Many Mars aerocapture design studies [46, 58, 59] opt for spacecrafts equipped with 70° sphere-cones. This shape was inherited from the Viking program [105], consisting of missions Viking 1 and Viking 2, which marked the successful exploration of the surface of Mars by NASA. In 1976, Viking 1 achieved the first successful on landing Mars, executing atmospheric entry with a lander housed within an aeroshell composed of a sphere-cone forebody and a biconic afterbody [106].

A sphere-cone is a geometry characterized by the seamless junction of a spherical shape, placed in the forward portion, and a conical shape. This geometry, presented in Figure 3.9, is defined by the following parameters:

- the base radius R_B [m] of the circular base of the conical portion;

- the nose radius R_N [m] of the spherical nose portion;

- the ratio $R_a = R_B/R_N$, which indicates the conical tapering relative to the spherical nose;

- the half-angle δ [°], representing half of the angle formed by the conical portion.

The forebody of the Viking 1 aeroshell had a base radius of 1.75 m, a half-angle of 70°, and a tapering ratio of 2 [106]. Following the success of Viking 1, its aeroshell shape was replicated for the Viking 2 lander later in the same year and for all the subsequent NASA Mars landers [107], culminating in the lander of the MSL mission, landed in 2012 [108].

Another commonly employed aeroshell shape [17, 60] is that of the Aeroassist Flight Experiment (AFE) [109], consisting of a non-axial-symmetric rake elliptic cone combined with an ellipsoidal nose cap. The main motivation behind this choice is the extensive aerodynamic and thermodynamic research conducted on the shape.

Apollo-shaped capsules have also been studied for potential use in aerocapture [57, 110], primarily for mass efficiency purposes. This shape consists of a truncated cone having a half-angle of approximately 30°.

More slender shapes, such as a triconic with a 25° half-angle [110], a Mars Sample Return Mission heritage biconic [60], or ellipsled geometries [58], have been explored to avoid in-orbit assembly, enhance packaging efficiency, and reduce heating rates thanks to higher L/D.

For this analysis, the Viking heritage 70° sphere-cone is selected. This choice is motivated by its simplicity, given by an axial-symmetric geometry, the inherited knowledge derived from past Mars missions, and the low L/D which, while potentially presenting a challenging thermodynamic environment, facilitates capture in a low-density atmosphere such as the Martian one. Furthermore, the avoidance of in-orbit assembly does not offer significant advantages for a high-cost mission of this nature. While the half-angle and the ratio R_a are chosen to be consistent with the original Viking aeroshield, a parametric analysis to assess the optimal nose radius is conducted in Chapter 4, because it significantly affects both aerodynamic performance and surface heating. As indicated by Equation (3.13), convective heat rate decreases as the nose radius increases [97]. Conversely, although different models suggest various options for the power of the nose radius to which radiative heating is proportional, they all agree on the fact

radiative heating increases with a larger nose radius (see Equations (3.16) and (3.19)) [62, 99, 100]. The opposing effects of the two main heating mechanisms underscore the need to reach a compromising middle ground.

3.5.2 Thermal Protection System

The selection of materials for the aeroshield and its TPS is primarily driven by their resistance to aerodynamic and heating loads. However, given the necessity to minimize mass, these considerations must also include an evaluation of the lightest available material options.

The 70° aeroshield employed in the Viking 1 mission had a main aluminum structure reinforced by additional T-rings and Z-rings to withstand the expected aerodynamic loads [111]. The TPS consisted of an 8.6 mm thick [111] layer of SLA-561V [112]. The acronym SLA stands for Super Light Ablator, indicating the ablative nature of the material. Ablative materials undergo controlled melting or sublimation when exposed to high heat fluxes, using their latent heat of fusion to reduce heat flux and protect the underlying structure from thermal damage, making them commonly used for planetary entry probes [95].

During the design phase of the MSL mission, the predicted peak heat flux of 234 W/cm^2 was deemed too extreme to be sustained by SLA-561V [113]. Consequently, a substitute in the form of an approximately 30 mm thick [108] layer of PICA was chosen to coat the forebody [113], given its capacity to withstand a maximum heat rate of 1500 W/cm^2 [114]. Additionally, its main structure was lightened by substituting aluminum with aluminum honeycomb, which eliminated the need for T-rings and Z-rings reinforcements thanks to an increased structural strength [108].

More recently, a new ablative TPS material has been developed, HEEET, able to withstand heat fluxes up to 8000 W/cm^2 [12].

While SLA-561V and PICA are considered low-density ablators, with densities of approximately 256 kg/m^3 and 274 kg/m^3 [115], HEEET falls into the mid-density ablator category, having a density of about 820 kg/m^3 [116].

For the primary structure of the aeroshield, MSL heritage honeycomb aluminum is selected due to its low density and demonstrated efficiency. Given the expected intense heating environment and the necessity of reducing the mass as much as possible, PICA is chosen as the preferred TPS material for this analysis. However, the potential use of HEEET remains an option if the computed heat flux is particularly high.

3.5.3 Mass calculation

The shield can ultimately be distinguished as the combination of two layers: the main structure and the ablative layer. The mass of the ablative layer will be calculated using Equation (3.12), which requires an estimation of the expected heat loads and will be calculated in Chapter 4.

The mass of the main structure of the aeroshield m_{ms}, on the other hand, can be simply calculated
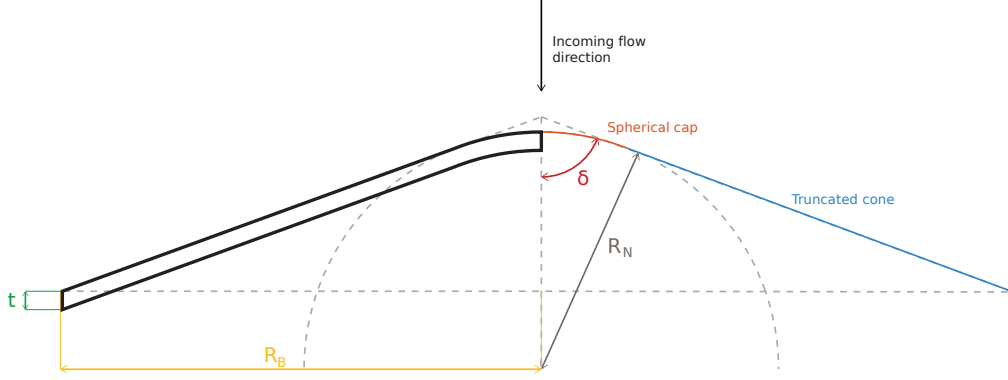
Figure 3.9: Sphere-cone section geometry and key parameters.

as the product of its volume V and the density ρ of the material it is made of:

$$m_{\mathsf{ms}} = V_{\mathsf{ms}}\rho_{\mathsf{ms}}, \tag{3.22}$$

where the subscript ms stands for *main structure*.

The volume V_{ms} can be calculated as the product of the surface S of the sphere-cone and its thickness t:

$$V_{\mathsf{ms}} = t_{\mathsf{ms}}S. \tag{3.23}$$

The surface can be obtained by separately considering the spherical cap and the truncated cone base. For a spherical cap, the surface is calculated as

$$S_{\mathsf{sc}} = \pi\left(a^2 + h^2\right), \tag{3.24}$$

with a being the radius of the base of the spherical cap and h being its height. In our case, $a = R_{\mathsf{N}}\cos\delta$ and $h = R_{\mathsf{N}}\left(1 - \sin\delta\right)$, yielding

$$S_{\mathsf{sc}} = \pi\left(\left(R_{\mathsf{N}}\cos\delta\right)^2 + \left(R_{\mathsf{N}}\left(1 - \sin\delta\right)^2\right)\right) = \pi R_{\mathsf{N}}^2\left(2 - 2\sin\delta\right). \tag{3.25}$$

For a truncated cone, the lateral surface can be calculated as the difference between the original cone and the part that is truncated,

$$S_{\mathsf{tc}} = \pi\left(RL - rl\right), \tag{3.26}$$

where R and r represent the radii of the original cone and the truncated cone, and L and l are their slant height. In our case, $R = R_{\mathsf{a}}R_{\mathsf{N}}$, $r = R_{\mathsf{N}}\cos\delta$, $L = R_{\mathsf{N}}/\sin\delta$, and $l = R_{\mathsf{N}}\cos\delta/\sin\delta$, giving

$$S_{\mathsf{tc}} = \pi\left(\frac{R_{\mathsf{a}}^2 R_{\mathsf{N}}^2}{\sin\delta} - \frac{R_{\mathsf{N}}^2\cos\delta^2}{\sin\delta}\right) = \frac{\pi R_{\mathsf{N}}^2}{\sin\delta}\left(R_{\mathsf{a}}^2 - \cos\delta^2\right). \tag{3.27}$$

Combining the two surfaces ultimately yields

$$S = S_{\text{sc}} + S_{\text{tc}} = \pi R_{\text{N}}^2 \left(2 - 2 \sin \delta + \frac{R_{\text{a}}^2}{\sin \delta} - \frac{\cos \delta^2}{\sin \delta} \right), \tag{3.28}$$

which, combined with Equations (3.23) and (3.22), defines the mass of the aeroshield main structure.

3.6 Surviving deceleration

The delicate nature of the human body, finely tuned to the gravity of Earth ($1g$), necessitates careful determination of maximum acceleration and deceleration limits during space flight and atmospheric entry.

As stated in the second law of Newton ("force equals mass times acceleration", $\vec{F} = m\vec{a}$), acceleration entails a corresponding force, hence the term *acceleration load*. Excessive acceleration loads pose significant risks to human health and safety, with consequences that affect several organs and systems, such as the musculoskeletal, cardiovascular, or respiratory one, and that can range in severity depending on the intensity of the load, its direction, and the time of exposure [117, ch. 8; 30].

NASA established maximum sustained translational acceleration limits based on those parameters and the duration of exposure to reduced gravity. For emergency conditions, meaning situations where crew survival must be prioritized, limit accelerations are maximum, but they drop for nominal conditions and become even lower for mission durations over 30 days, where the crew is considered deconditioned and lower limits must be applied [30].

The direction of the load relative to the human body significantly influences the maximum sustainable acceleration. Longitudinal loads from the front ($+G_{\text{x}}$) are better sustained than those from the back ($-G_{\text{x}}$), and both are preferable to lateral ($\pm G_{\text{y}}$) or vertical ($\pm G_{\text{z}}$) ones. The impact of the time of exposure is illustrated in Figure 3.10 for the $+G_{\text{x}}$ case [30].

In this analysis, it is assumed that the crew can be rotated to ensure acceleration loads always come from the front ($+G_{\text{x}}$). Additionally, the lower limits for a deconditioned crew are utilized, given the crew will have spent more than 30 days in a reduced gravity environment in most of the cases considered, resulting in more conservative limits than those that would occur for shorter missions. The maximum acceleration limits for this case are shown in Table 3.1.

Duration [s]	0.5	10	30	50	90	120	150	10000
Acceleration [g]	14	10	8	6.3	5	4.3	4	4

Table 3.1: Maximum $+G_{\text{x}}$ acceleration limits for deconditioned crew [30].

As acceleration arises with every change in velocity, acceleration loads appear during both propulsive maneuvers and aerocapture. Only those arising from the latter, though, are going to be investigated, due to aerocapture being the main focus of this analysis.
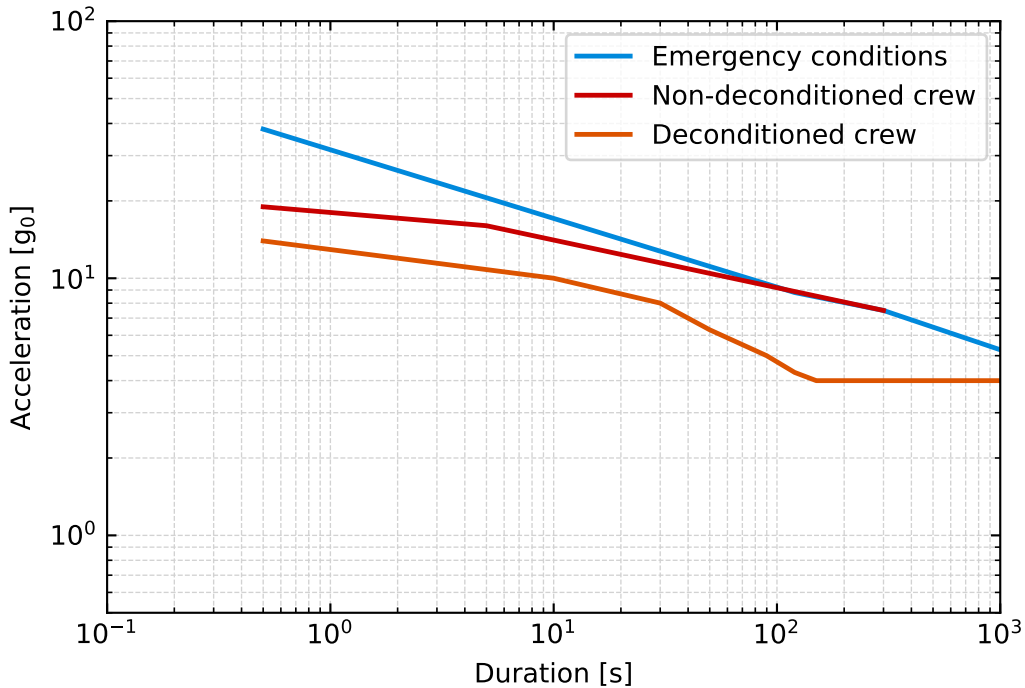
Figure 3.10: Maximum $+G_x$ sustained translational acceleration limits

3.7 Aerocapture Alternatives

This chapter focused on defining the atmospheric entry environment encountered by the spacecraft during an aerocapture maneuver. The entry dynamics were presented, along with the specific atmospheric conditions of Mars and the way they were modeled for this work. The hypersonic flow regime experienced by the vehicle upon entry was defined, and the critical issues introduced by the formation of a bow shock wave were addressed. The convective heating model that will be used was introduced, and three models for radiative heating have been analyzed to determine the best option for this case. The aeroshield was selected after considering the available options, and its materials and geometry were assessed. Finally, the maximum acceleration loads that must be respected to ensure crew safety were presented.

Chapter 4 will use the methodologies outlined in the previous sections to perform a parametric analysis aimed at optimizing the aerocapture system so that the feasibility associated with implementing this maneuver at Mars can be assessed. A comparison will then be drawn between a purely propulsive scenario and one integrating aerocapture as the primary braking strategy to be captured at Mars.

In both scenarios, the spacecraft starts its journey from LEO and uses its propulsive system to execute the first Δv maneuver.

In the purely propulsive case, the entirety of the required Δv at Mars is achieved through propulsion. This maneuver will be strategically executed at the periapsis of the hyperbolic arrival orbit to maximize efficiency. The necessary Δv will likely be substantial, and while burn and gravity losses are included in Equation (2.16), assuming this maneuver can be completed at periapsis is a simplification used to estimate the order of magnitude of the propellant mass. Equation (2.16) will be solved for the various

propulsive system configurations presented in Table 2.1, first at Mars and then at Earth, where the propellant required by the former is going to be accounted for as well. Pareto fronts illustrating the trade-off between spacecraft mass and transfer time will then be presented.

Subsequently, aerocapture at Mars will be explored as an alternative strategy to obtain the Δv at Mars without relying on the propulsive system. This approach eliminates the need to transport additional propellant mass, thereby reducing the propellant mass required at arrival. While a propulsive Δv maneuver remains necessary at Earth, a lighter spacecraft facilitates it and reduces the propellant required for this maneuver as well. If any of the previously presented constraints — such as acceleration (Section 3.6), heat rate (Section 3.4), or minimum altitude — are violated, aerocapture will be combined with a propulsive maneuver to decelerate the spacecraft before atmospheric entry and create a more favorable aerothermodynamic environment.

Finally, the Pareto fronts of the aerocapture scenario will be compared with those from the purely propulsive approach to assess the mass-benefit, if any, of employing this technique.

Chapter 4

Results and Discussion

Relating aerocapture to rapid missions requires a comprehensive understanding of its feasibility and the constraints imposed by atmospheric entry. Specifically, adherence to those constraints must be ensured from the beginning of the interplanetary trajectory.

Initially, aerocapture is examined as independent from the interplanetary segment to determine the required entry conditions that ensure an effective maneuver while guaranteeing it is also safe for the crew.

Subsequently, the interplanetary trajectory is linked to the atmospheric entry phase to obtain the required Δv, thereby determining the propellant requirements at both departure from Earth and arrival at Mars, depending on the utilization or omission of aerocapture.

Finally, Pareto fronts for the IMLEO are derived for the propulsion system cases delineated in Table 2.1. Optimization efforts focus on the engine thrust and, for the aerocapture scenarios, the nose radius of the aeroshield and the distance at which propulsive braking is conducted. A comparative analysis between the purely propulsive and aerocapture scenarios is then drawn to define the mass benefit of the latter.

4.1   Aeroshield

Although the shape and materials constituting the aeroshield have been preliminarily determined and discussed in Section 3.5.1, the success of aerocapture is influenced by various parameters beyond these initial considerations. Among these, the nose radius R_{N}, which is half the base radius R_{B} of the shield, and the angle of attack α (Figure 4.1) play a fundamental role and require to be optimized to ensure the proper conditions are met during atmospheric entry.

4.1.1   Aerodynamic Coefficients

To assess their impact aerodynamic coefficients, specifically the drag coefficient C_{D} and the lift-to-drag ratio L/D, were computed using MC-New and subsequently plotted to illustrate their variation over a range of nose radii (1 m to 10 m) and angles of attack (-10° to +10°).
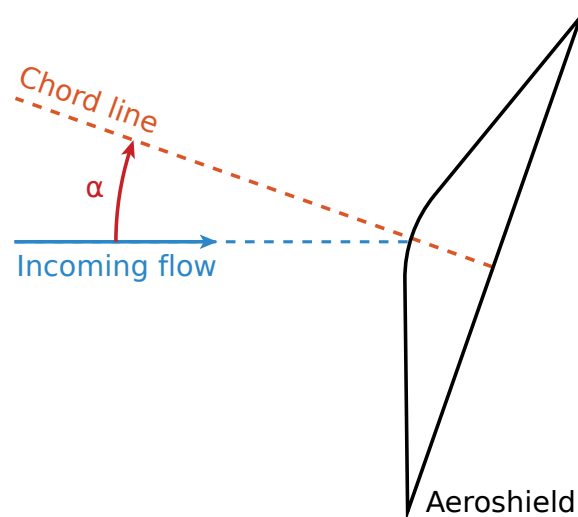
Figure 4.1: Representation of the angle of attack of the aeroshield.

Observing Figure 4.2, it becomes evident that both the drag coefficient and the lift-to-drag ratio are independent of the nose radius. The small fluctuations observed in the drag coefficient plot can be attributed to the inherent margins of error within the software.

The angle of attack, on the other hand, emerges as the main determinant of aerodynamic coefficients once the shape of the aeroshield is selected. In the diagrams, solid lines represent positive values of the angle of attack, while dashed lines indicate negative ones. It can be seen that the sign of the angle of attack does not influence the drag coefficient. The lift-to-drag ratio, however, shows a symmetrical distribution of positive and negative angles of attack around $\alpha = 0$.
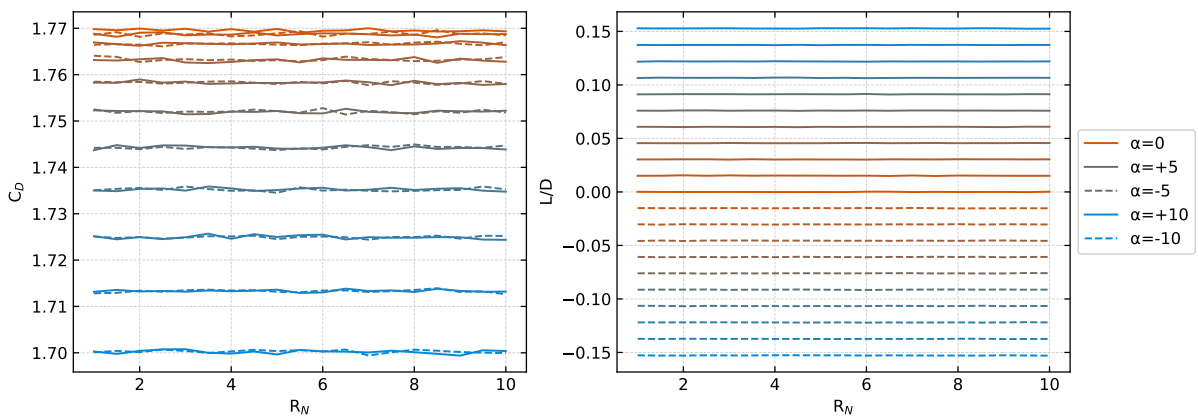
Figure 4.2: Aerodynamic coefficients for varying nose radii and angles of attack.

4.1.2 Theoretical Corridor Width

Further analysis revolved around understanding the influence of the lift-to-drag ratio on the TCW, as well as the potential role of the mass, nose radius, and entry velocity on it. This analysis was conducted by simulating entry conditions using AMAT [82] and retrieving the corresponding TCW.

As illustrated in Figure 4.3, the TCW is mainly driven by the lift-to-drag ratio, hence by the angle

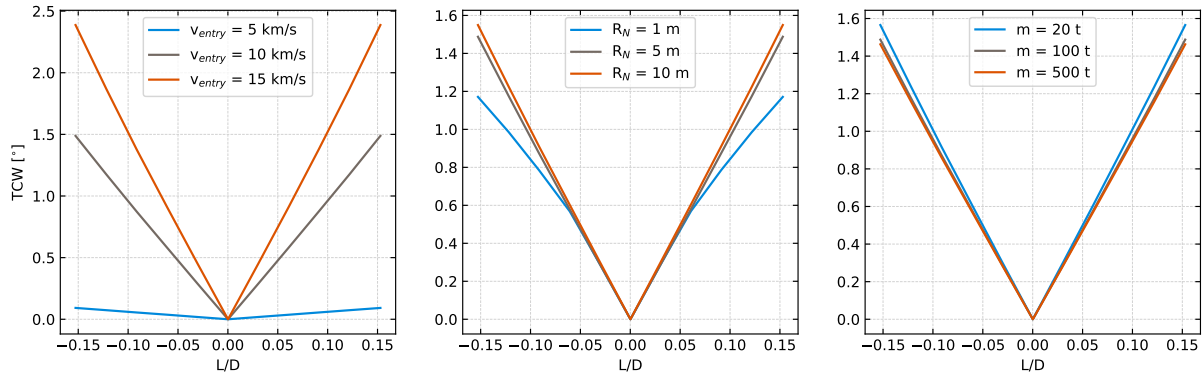Figure 4.3: TCW for varying lift-to-drag ratio, entry velocity, nose radius, and mass.

of attack. Emphasizing the requirement of maintaining TCW $\geq 1°$, all plots highlight the necessity of keeping a lift-to-drag ratio different from zero. As shown by the L/D plot of Figure 4.2, this implies the necessity of keeping a non-zero angle of attack.

Entry velocity also significantly affects the TCW, with decreasing velocities providing narrower corridor widths. This phenomenon stems from the diminished aerodynamic forces exerted on the spacecraft at lower velocities, which require a more controlled trajectory to achieve optimal aerodynamic performance.

Additionally, the TCW proves to slightly increase with larger nose radii and smaller masses. Because of the fixed ratio between the nose radius and base radius, a bigger nose radius entails a larger reference area, which facilitates capture by increasing the drag surface and, as a result, the drag force. Conversely, smaller masses demand less drag force to achieve adequate deceleration, thereby resulting in a wider interval of densities to achieve it.

4.1.3 Aeroshield main structure mass

Reminding that the aeroshield is mainly composed of two layers - an internal main structure, made in honeycomb aluminum, and an external TPS, consisting of ablative material - this section will address the main structure mass. The discussion regarding the TPS mass will be postponed to Section 4.4.3, as it depends on the encountered heat load through Equation (3.12).

As presented in Section 3.5.3, the mass of the main structure can be calculated as the product of the volume and the density of the material (Equation (3.22)). Given that honeycomb aluminum is not a bulk material, its density is not pre-defined and can range from $\sim$20 kg/m^3 to $\sim$120 kg/m^3, depending on foil thickness and cell size [118]. To avoid an arbitrary choice that could potentially lead to underestimation, the density of honeycomb has been directly derived from the mass of the MSL heat shield, whose value is documented [119], after removal of its TPS. This methodology yielded a main structure density of $\rho_{\mathsf{ms}} = 221$ kg/m^3. Although it appears to be a major overestimation compared to the recommended values, using this value allows for the inclusion of elements beyond the main structure and TPS that are inevitably included in an aeroshield.

As illustrated in Figure 4.4, the mass of the main structure varies with the third power of the nose
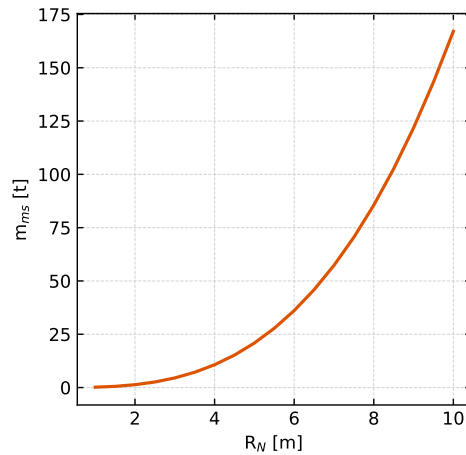
Figure 4.4: Shield main structure mass for varying nose radii.

radius, resulting in particularly massive values for larger nose radii. The advantages of a low mass and those of a large nose radius, which are presented in Section 4.1.2 and will be further investigated in Section 4.3, are inherently conflicting and require that an optimal compromise is reached.

4.2 Acceleration

The compliance with the multiple acceleration limits, which depend upon the time of exposure as presented in Section 3.6, has been assessed across varying entry velocities, masses, and nose radii.

Atmospheric entry was analyzed using AMAT [82], which provided the acceleration profile for each of the considered entry conditions. Then, the maximum and sustained acceleration limits presented in Table 3.1 were imposed. Ensuring adherence to the maximum acceleration limit implied verifying that the vehicle never experienced accelerations exceeding the prescribed limit during the maneuver. Investigating sustained acceleration limits, on the other hand, required checking the duration for which the vehicle surpassed the limit imposed for each time interval.

An illustrative example is provided in Figure 4.5, which represents the acceleration experienced during atmospheric entry by a vehicle having $R_N = 5$ m, $\delta = 5°$, $m = 100$ t, and $v_{entry} = 11$ km/s. While the maximum limit of approximately $14g$ is never surpassed, the sustained accelerations exceeding the limit for intervals of up to 10 s and 30 s render such cases unsuitable, as all acceleration constraints must be met.

The main driver of acceleration loads is the entry velocity, as it dictates the Δv that must be achieved to ensure capture and, consequently, the magnitude of deceleration required to obtain it. The relationship between entry velocity and time spent over the acceleration limit is depicted in Figure 4.6 for an entry mass of 20 t.

The upper limits of 90 s, 120 s, and 150 s, have not been plotted, as they were not reached in any of the experimental cases. Lower limits, however, pose significant constraints on the maximum entry velocity. Specifically, the 10 s acceleration limit of approximately $10g$ is surpassed for all entry velocities exceeding about 10.3 km/s. Figure 4.6 shows how the nose radius exerts a minimal influence
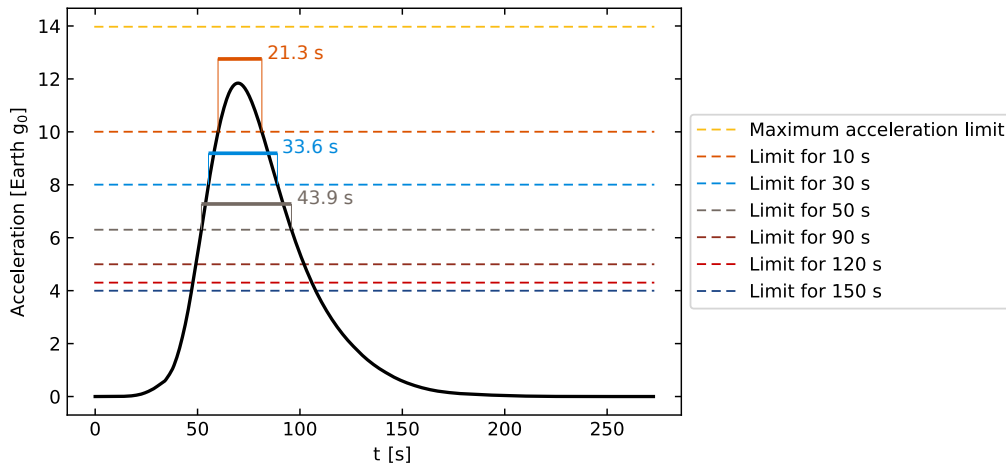
Figure 4.5: Example acceleration profile during an aerocapture maneuver.

on acceleration loads. Similarly, increasing the entry mass also showed no major impact, resulting in a very similar acceleration profile.

Given the importance of keeping acceleration loads within the limits to guarantee crew safety, a conservative maximum allowable entry velocity $v_{\text{entry}} = 10$ km/s has been chosen for this study.
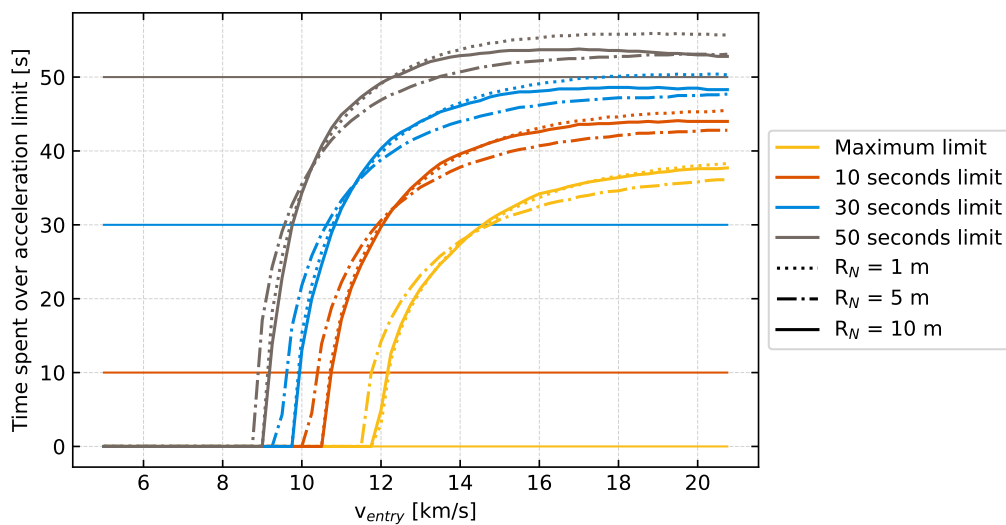
Figure 4.6: Time spent over the acceleration limits as a function of entry velocity for varying nose radii.

4.3   Minimum Altitude

The possibility of the spacecraft inadvertently encountering any of the highlands of Mars required a careful evaluation of the minimum altitude required to perform successful aerocapture. To mitigate such risks, a minimum altitude limit of 30 km was imposed, accounting for the possibility of incurring into the Tharsis region, where Mount Olympus reaches an altitude of 25 km [21–23]. While theoretically feasible to navigate around such areas with precise trajectory calculations and navigation systems, the extreme nature of this mission imposes that meticoulous care is put into respecting the given constraints with

Figure 4.7: Minimum altitude as a function of entry velocity for varying nose radius and mass.

ample margin.

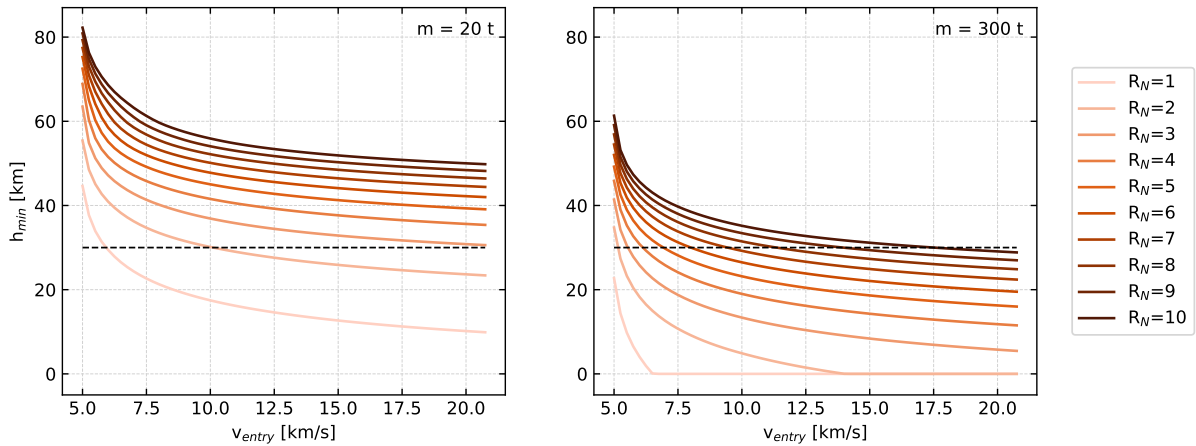The minimum altitude required to achieve aerocapture has been derived using AMAT [82] for various nose radii, masses, and entry velocities. Results, which are illustrated in Figure 4.7, underscored the significant impact of all aforementioned parameters on the potential violation of the 30 km constraint.

Generally, a vehicle needs to descend deeper into the atmosphere if its capture requires encountering the higher densities that concentrate close to the surface. Smaller shields must compensate for their reduced drag surface, whereas spacecraft with larger masses or entering at higher velocities need it to develop the additional drag that ensures they are properly decelerated.

Notably, for a 300 t spacecraft having a nose radius of 1 m or 2 m, the pursuit of higher densities would inevitably lead to surface impact after a certain entry velocity, rendering the entire aerocapture operation unfeasible.

Ultimately, since mass is not a design parameter but nose radius is, the minimum altitude constraint imposes a minimum nose radius dependent on both mass and entry velocity. For the maximum allowable atmospheric entry velocity of 10 km/s, the corresponding limit entry masses for each nose radius are tabulated in Table 4.1.

R_{N}, m	1	2	3	4	5	6	7	8	9	10
Maximum entry mass, t	-	22	50	86	138	200	260	340	440	540

Table 4.1: Maximum entry mass imposed by the constraint on minimum altitude for varying nose radii.

A nose radius of 1 m did not provide any result across the considered entry mass range. Consequently, it will be excluded from any following consideration to ensure that subsequent analyses are based on viable configurations only.

4.4 Heating

Both the heat rate and heat load were computed across the presented range of parameters. The heat rate quantifies the amount of heat transferred per unit area to the TPS of the spacecraft during

atmospheric entry, thereby dictating the choice of material required. The heat load, as presented in Equation (3.12), defines the TPS mass fraction over the total entry mass.

Given the divergent correlations between heat flux and nose radius for convective and radiative heating (see Section 4.4.1), particular attention is given to defining an optimal nose radius that could, ideally, minimize both.

4.4.1 Convective and Radiative Heating

Equation (3.13) reveals that convective heating scales with $R_N^{-0.5}$, while Equations (3.16) and (3.19) (the chosen models for radiative heating) manifest dependencies on $R_N^{0.526}$ and $R_N^{0.49}$, respectively.

The contrasting dependencies on the nose radius appear when comparing the plots of Figure 4.8, where convective and radiative heating are plotted for the atmospheric density at 30 km of altitude (the highest one that the spacecraft will potentially encounter) across varying velocities, for nose radii of 2 m and 10 m. The hump that can be seen in the radiative heating curve is attributed to the use of the Tauber-Sutton model [62] within the velocity range of 6 km/s to 9 km/s, which provides an overestimation of heat rates compared to the Venus one [100] employed for other velocities. Although it does interfere with defining the intersection of convective and radiative heating, it does not get in the way of the purpose of this analysis, which is to show the opposing effects of the nose radius on the two primary heating mechanisms.

Figure 4.8: Convective versus radiative heat rate as a function of velocity for $R_N = 2m$ and $R_N = 10m$ at 30 km of altitude.

It is noteworthy how the radiative heat rate rises as a consequence of augmenting the nose radius, while the convective heat rate decreases. Because of this, the intersection between the two curves, which represents the velocity at which radiative heating becomes predominant over convective one, shifts, occurring at about 10 km/s for a 2 m nose radius, and at approximately 6.5 km/s for a 10 m one.

Furthermore, atmospheric density plays a pivotal role in determining the predominant heating mechanism. When the same analysis is conducted at 100 km of altitude (Figure 4.9), where atmospheric

density is approximately ten thousand times less dense than at 30 km, the intersection between the curves occurs at even higher velocities.

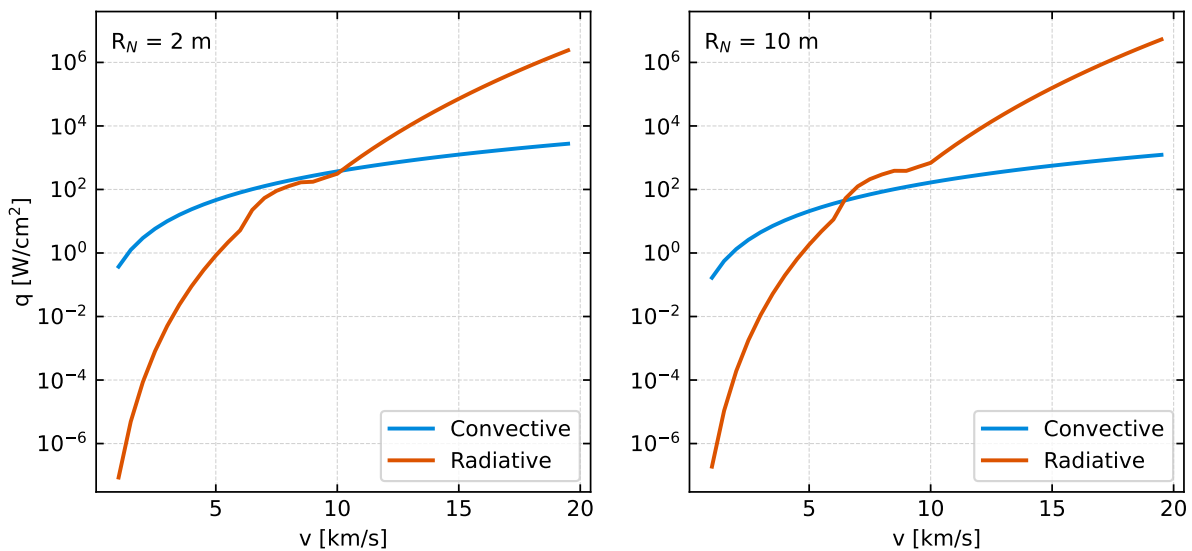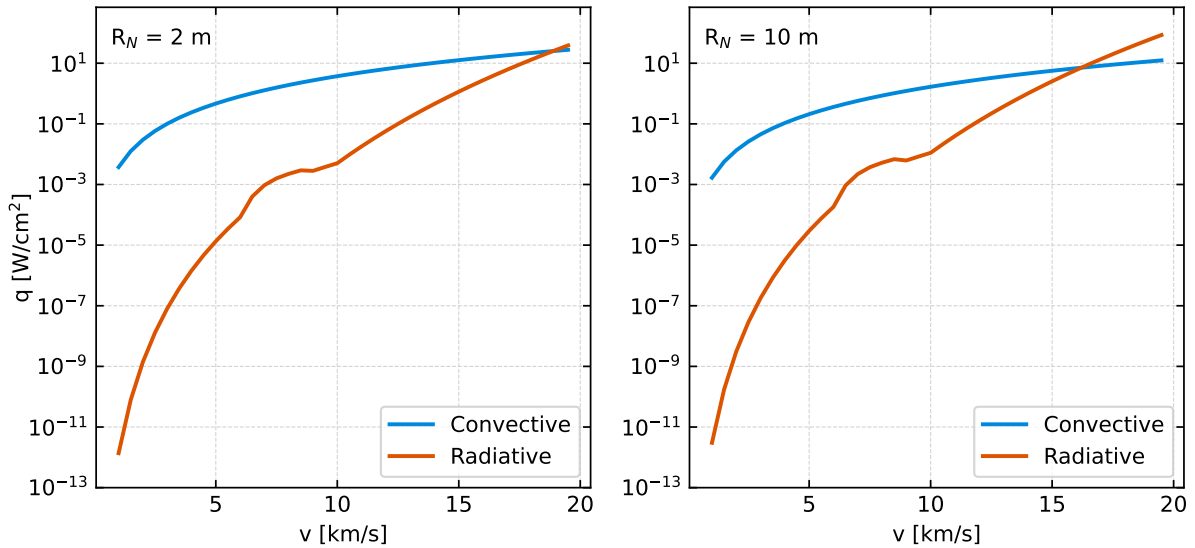

Figure 4.9: Convective versus radiative heat rate as a function of velocity for $R_N = 2m$ and $R_N = 10m$ at 100 km of altitude.

The fact that deep dives into the atmosphere of Mars at high velocities and with large nose radii have been rarely considered in literature explains the lack of adequate radiative models for the Planet and the tendency of some research to consider radiative heating negligible. However, its significant contribution to total heating under conditions likely encountered during aerocapture highlights the necessity of considering its influence in these maneuvers and, more broadly, in atmospheric entry at high velocity.

4.4.2 Heat Rate

After assessing the significance of radiative heating in the context analyzed by this study, a parametric analysis like those conducted for acceleration and minimum altitude was performed for the final constraint imposed by atmospheric entry: maximum heat rate.

The results, depicted in Figure 4.10, feature heat rate limits for PICA and HEEET serving as the thresholds for allowable heat rate. All the curves exhibit a discontinuity occurring at an entry velocity of approximately 11 km/s, attributed to the transition in predominance between convective and radiative heating. Increasing entry velocity results in higher heat rates, imputable to both the higher instantaneous velocity and the higher densities encountered at the lower altitudes that must be reached to decelerate. The increase in heat rates shown for the 300 t spacecraft compared to the 20 t counterpart is also attributed to the same cause.

The behavior of the curves for varying nose radii was found to be less predictable than that of the aforementioned parameters. At the high velocities where radiative heating predominates, the influence of a larger nose radius in the radiation equation is not sufficient for these spacecraft to experience higher heat fluxes than the smaller nose radius counterparts. Once again, this phenomenon can be traced back to the lower altitudes that must be reached when employing smaller shields.
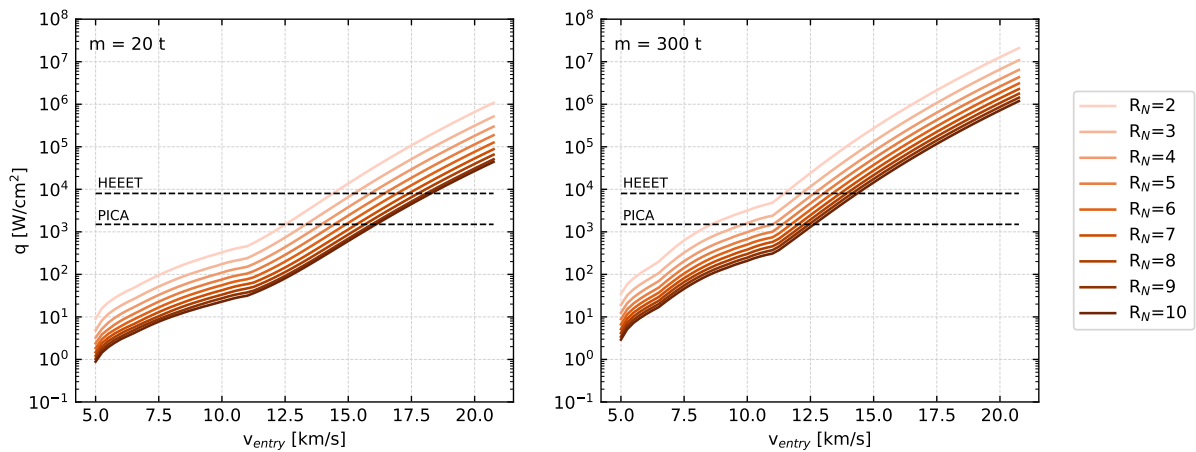
52

Figure 4.10: Maximum heat rate on the stagnation point as a function of entry velocity for varying nose radius and mass.

The limit heat rate imposed by the choice of PICA as TPS material does not introduce any additional constraint on mass, entry velocity, or radius beyond those already imposed by acceleration or minimum altitude limits. For a 20 t spacecraft, all nose radii can be used until the 10 km/s limit imposed by acceleration loads. For the 300 t one employing a shield having $R_N < 3$ m means surpassing the limit heat rate imposed by PICA at 10 km/s. However, at the same entry velocity, the use of shields with $R_N < 8$ m is already restricted by minimum altitude constraint, as depicted in Figure 4.7.

4.4.3 Heat Load

The total heat load on the stagnation point was calculated as a function of entry mass for varying nose radii at the maximum allowable entry velocity of 10 km/s. It has then been correlated to the TPS mass fraction using Equation (3.12), displaying the results that are depicted in Figure 4.11. Due to the higher heat load experienced at higher entry masses and smaller nose radii, the TPS mass fraction increases significantly with those parameters, displaying the necessity of the TPS to be even more massive than the spacecraft itself, in some cases.

Consequently, although larger nose radii inherently entail high structural masses, as discussed in Section 4.1.3, larger shields require a smaller mass fraction to be dedicated to the TPS. Given the substantial masses anticipated after a rapid interplanetary transfer, this result suggests that smaller shields may not necessarily offer a solution for achieving lower entry masses.

4.5 Density uncertainties

The aerocapture profile has been analyzed across a range of anticipated density uncertainties, adjusting the density within the recommended range of variability depending on the altitude. Between 0 km and 30 km, it manifests variations within $\pm 10\%$, while at 80 km it can vary within $\pm 50\%$. Maximum variability is reached in the higher levels of the atmosphere, where the density can vary up to $\pm 100\%$ [39].
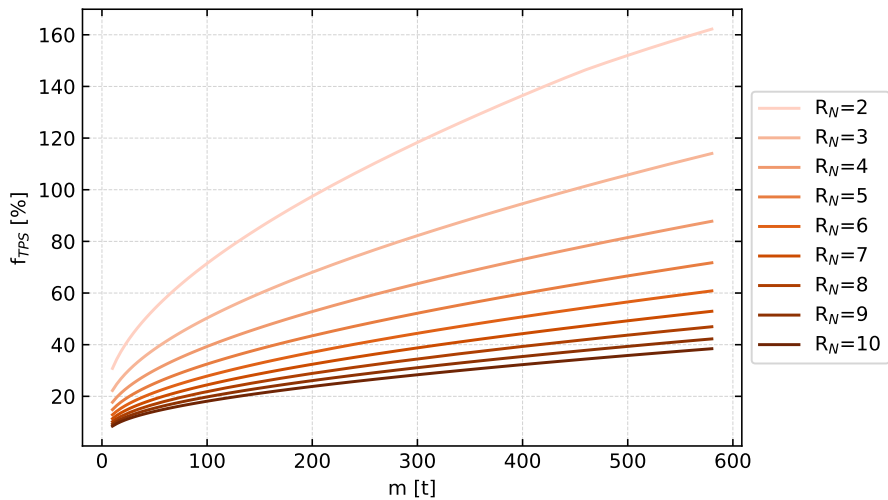
Figure 4.11: TPS mass fraction as a function of entry mass for varying nose radii, at v_{entry} = 10 km/s.

The resulting density profile is depicted in Figure 4.12, while the consequences on altitude, acceleration, and heat rate experienced during a representative aerocapture maneuver are shown in Figure 4.13. Generally, altitude decreases in the lower-density scenario as the spacecraft needs to reach densities that allow it to generate sufficient drag for aerocapture. Consequently, lower altitudes lead to increased maximum decelerations and heat rates in the lower-density scenario, rendering it the most critical one. Conversely, the higher-density case allows for a higher minimum altitude and lower maximum deceleration and heat rate, proving to be a more favorable scenario.
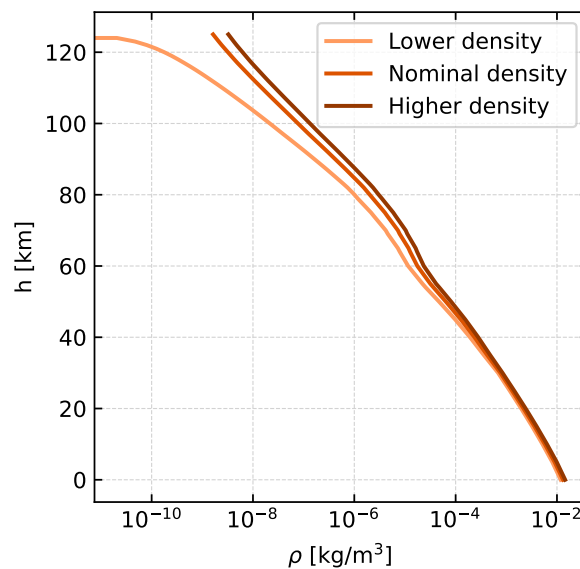
Figure 4.12: Density uncertainties range.

Percentage changes in the three constraints for the lower-density case were investigated by conducting the same analysis for varying nose radii and entry masses. Results indicated maximum variations in maximum deceleration manifested for larger nose radii and higher entry masses, reaching values of 4.35%. However, maximum variations on minimum altitude and heat rate manifested for larger nose radii

54

but lower entry masses, with percentages up to 4.69% and 4.80%, respectively.

The variation in the outcome velocity, which represents the ultimate metric of aerocapture efficiency, reached maximum percentages on the order of 10^{-3}%, highlighting how, regardless of density uncertainties, success can be ensured by modulating the altitude reached.

Overall, the percentage variations are low, enabling compliance with constraints even in less favorable scenarios, indicating that density uncertainties are not critical to the analysis. Nevertheless, while they may be negligible in a broad feasibility study such as this, actual mission design must consider the possibility of the design trajectory failing to achieve the desired Δv, underscoring the importance of robust guidance and navigation systems.
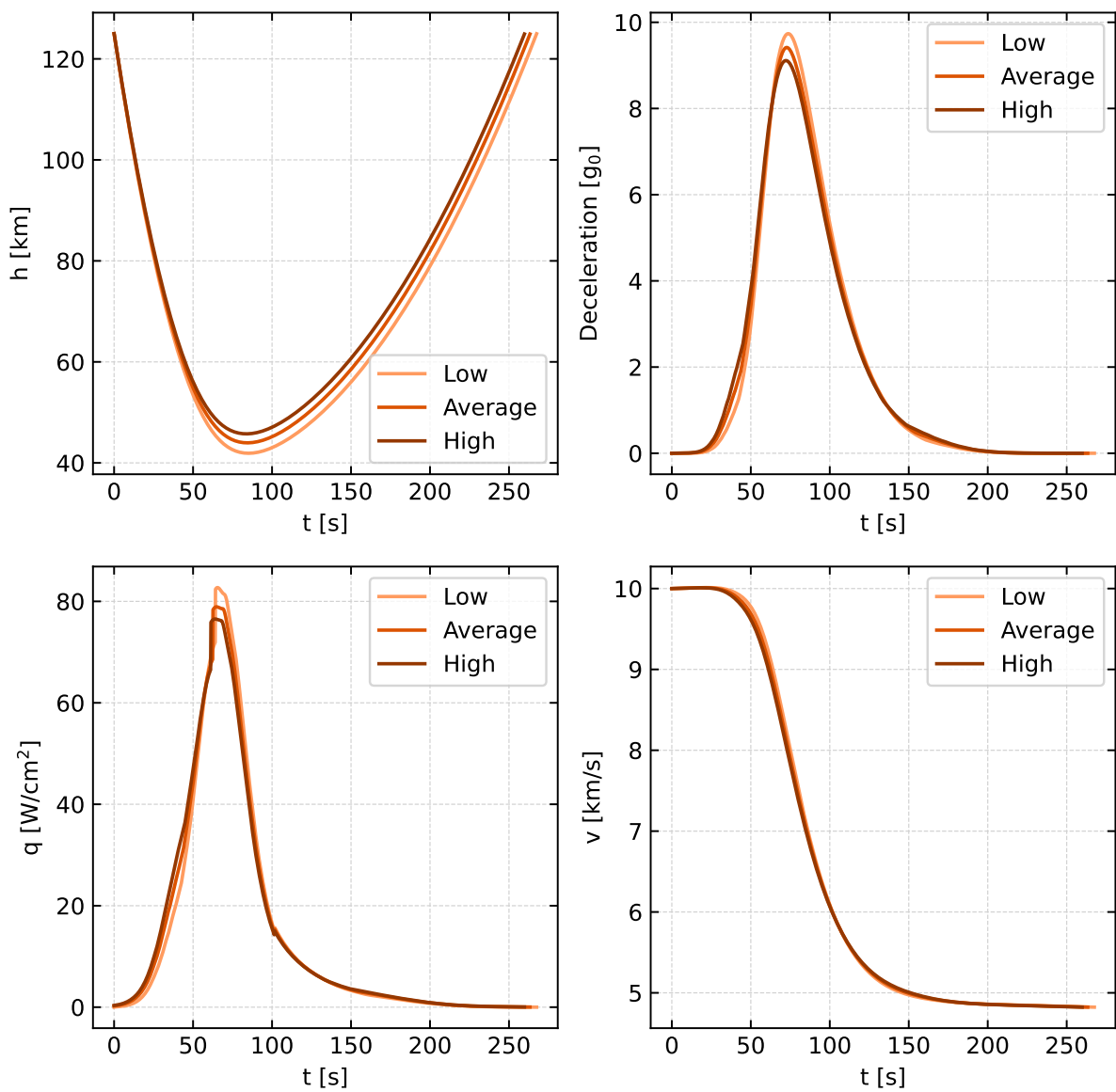
Figure 4.13: Altitude, acceleration, heat rate, and velocity during an aerocapture maneuver at $v_{\text{entry}} = 10$ km/s, $R_{\text{N}} = 10$ m, $m = 100$ t over the range of low, average, and high density hypotheses.
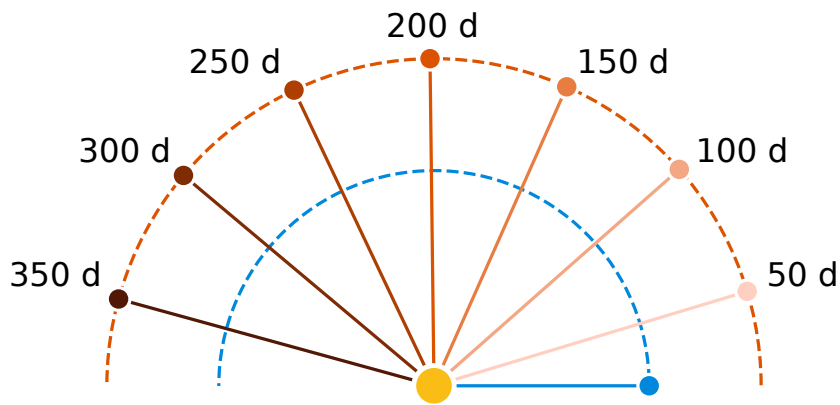
Figure 4.14: Required positions of Earth at departure and Mars at arrival depending on total mission time.

4.6 Interplanetary Trajectory

The interplanetary trajectory and its implications on the required Δv have been investigated for total mission times (including outbound segment, stay on Mars, and inbound segment) ranging from 50 days to 365 days, with a one-day time step.

The initial step in defining the interplanetary trajectory was determining the necessary transfer angle to reach Mars, spend 30 days there, and return with an inbound segment of equal duration to the outbound one. A visualization of the required starting conditions is provided in Figure 4.14.

Solving Lambert's problem over the entire time range provided the required velocities at the Earth and Mars, delineating the entire outbound segment. Subsequently, analysis was conducted to determine the velocity the spacecraft would attain at atmospheric entry on Mars. As shown in Figure 4.15, entry velocity exceeded the 10 km/s limit imposed by the constraint on maximum deceleration in all considered cases. This underscores the necessity for preliminary braking, as aerocapture cannot be safely achieved via direct insertion from the interplanetary orbit.

Preliminary braking can be executed at any moment preceding atmospheric entry, with the sole constraint of limiting the entry velocity v_{entry} to 10 km/s. To simplify the analysis, two extreme braking points were considered: immediately before atmospheric entry (at an altitude of 125 km) and at the interface of the sphere of influence of Mars (at a distance of 578 000 km from the center of Mars). In the former case, the Δv is applied directly to the entry velocity to reduce it to 10 km/s. In the latter, braking is applied to decrease the velocity at infinity to the value that ensures the atmosphere is crossed at 10 km/s.

The Δv resulting from these considerations are depicted in Figure 4.16, alongside those required at Earth to accelerate from LEO and to brake at Mars periapsis (the chosen strategy in the case of a purely propulsive transfer).

This plot reveals a notable reduction in all Δv as the transfer time increases, foreshadowing the substantial propellant requirement for achieving rapid arrival at Mars. Braking at Mars infinity appears
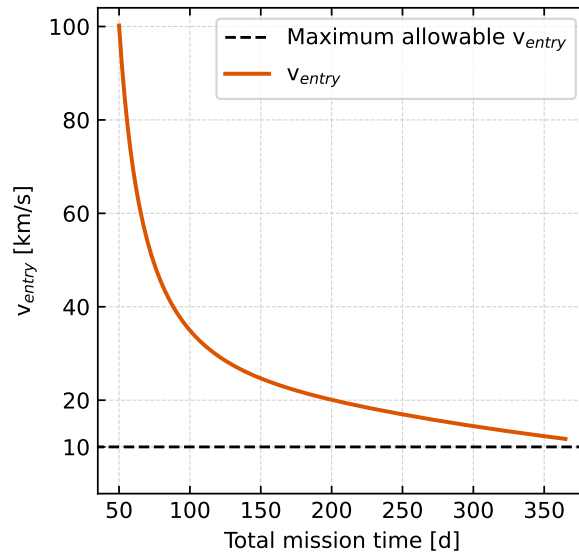
Figure 4.15: Entry velocity at Mars atmosphere as a function of total mission time.

marginally more advantageous than braking right before atmospheric entry, although the difference is minimal. The distance between the orange and red curves represents the portion of Δv that would be exerted by the atmosphere, representing the advantage achievable by introducing aerocapture. Particularly for lower transfer times, this benefit may seem modest, but its effect on reducing the propellant at Mars will reflect on the propellant demand at Earth, potentially offering more significant advantages in the IMLEO.
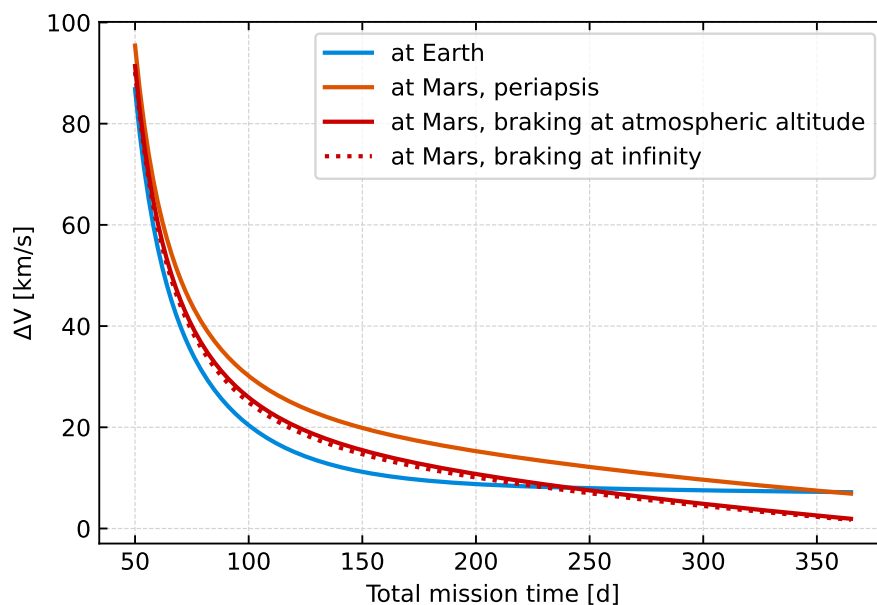
Figure 4.16: Δv requirements at Earth and Mars. Braking at periapsis represents the chosen strategy for a purely propulsive scenario, while braking at atmospheric altitude and infinity represent the preliminary braking to be done before an aerocapture maneuver.

4.7   Initial Mass in Low Earth Orbit

Once the required Δv and spacecraft mass are determined, the IMLEO can be computed for all propulsion systems presented in Table 2.1. The elements that contribute to the IMLEO were presented in Sections 2.5 and 3.5.3, and are summarized in Table 4.2.

| Element	Mass, kg
THAB main structure	$122.61 \left(N_{\text{crew}} d^{0.59}\right)^{2/3}$
THAB shielding	$804.37 \left(N_{\text{crew}} d^{0.59}\right)^{2/3}$
Crew	$82 N_{\text{crew}}$
Consumables	$9.88 N_{\text{crew}} d + 51.63 N_{\text{crew}} + 0.31 d + 182.5$
Subsystems	670.9
Accommodations	4010
Propulsion system	$\frac{T}{g_0 (T/W)}$
Propellant at Earth	$\frac{1}{1-\epsilon_{\text{t}}} \frac{m_{\text{pr,E}}}{m_{\text{pl}}} = \exp\left(\frac{1}{1-\epsilon_{\text{t}}} \frac{\Delta v_{\text{E}}}{g_0 I_{\text{sp}}} \left(1 + \frac{1}{24} \frac{\mu_{\text{E}}}{r_{\text{LEO}}^3} \left(\frac{g I_{\text{sp}}}{T} m_{\text{pr,E}}\right)^2\right)\right) - 1$
Propellant at Mars	$\frac{1}{1-\epsilon_{\text{t}}} \frac{m_{\text{pr,M}}}{m_{\text{pl}}} = \exp\left(\frac{1}{1-\epsilon_{\text{t}}} \frac{\Delta v_{\text{M}}}{g_0 I_{\text{sp}}} \left(1 + \frac{1}{24} \frac{\mu_{\text{M}}}{r_{\text{M}}^3} \left(\frac{g I_{\text{sp}}}{T} m_{\text{pr,M}}\right)^2\right)\right) - 1$
Aeroshield main structure	$\rho_{\text{ms}} t_{\text{ms}} \pi R_{\text{N}}^2 \left(2 - 2\sin\delta + \frac{R_{\text{a}}^2}{\sin\delta} - \frac{\cos\delta^2}{\sin\delta}\right)$
Aeroshield TPS	$m_{\text{entry}} f_{\text{TPS}}$

Table 4.2: Elements contributing to the IMLEO [1, 72].

Aeroshield main structure and aeroshield TPS are only considered in the case of aerocapture. The entry mass m_{entry} referred to in the calculation of the TPS comprises all preceding elements except propellant, which will be depleted by the time of atmospheric entry. The payload mass m_{pl} that figures in propellant calculation includes all the mass of the spacecraft at the time the maneuver is conducted. For propellant calculation at Mars, r_{M} denotes the radius at which braking occurs, representing the periapsis radius for the purely propulsive scenario, and either the radius of the atmospheric interface or that of the sphere of influence of Mars for aerocapture.

The table displays the multitude of parameters contributing to the IMLEO. Among these, the specific impulse I_{sp} and thrust-to-weight ratio of the engine T/W depend on the propulsion system under consideration (refer to Table 2.1), while thrust T is a design parameter. Δv_{E} and Δv_{M} depend on the total trip time d, and the latter also depends on whether aerocapture is used and, if so, whether braking occurs just before entering the atmosphere or at infinity. Finally, the nose radius R_{N} identifies the chosen shield size.

To ensure a comprehensive analysis, all propulsion systems will be examined for total trip times ranging from 50 to 365 days. The use of aerocapture will be explored with braking at atmospheric altitude and infinity, considering nose radii ranging from 2 m to 10 m. All cases will be studied across a broad range of thrust values, and the ones yielding the lower IMLEO will be selected for the final Pareto fronts.
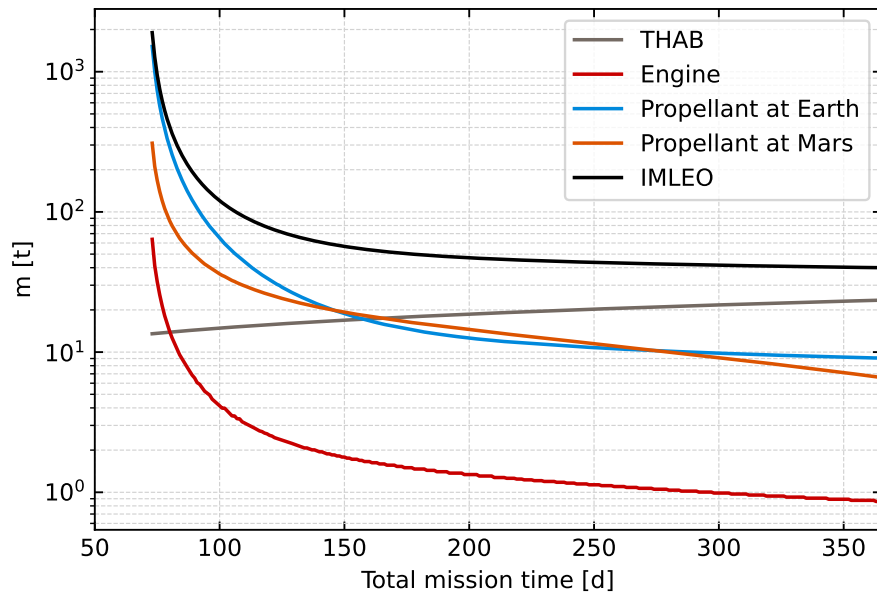
Figure 4.17: Mass contribution to the IMLEO of all the elements constituting the spacecraft in the propulsive case.

4.7.1 Purely Propulsive Scenario

The contribution to the IMLEO of the various elements is shown in Figure 4.17 for Case III. A minimum value for the total mission time can be observed, corresponding to the point at which the modified rocket equation no longer provides solutions for the propellant. Near this point, the curves representing the masses of the engines, propellants, and IMLEO tend asymptotically towards it, and then decrease with increasing transfer time. The THAB mass, which includes THAB main structure, THAB shielding, consumables, subsystems, and accommodations, is the only one showing an ascending trend, attributed to the proportionality of most of these terms to the outbound transfer time. The combination of this increase and the decreasing nature of the other curves implies the THAB mass becomes prevalent over longer transfer times and predicts the existence of a minimum point for the IMLEO. Conversely, for shorter trips, the IMLEO is mainly determined by the propellant mass, with a significant influence of that required for acceleration from LEO. The contribution of engine mass, except for a brief initial portion, is negligible compared to the other elements.

Results for all the propulsive cases (defined in Table 2.1) are presented in Figure 4.18. To ensure clarity, the plot has been capped at 10^4 t, allowing for a better visualization of Cases II to V, which would otherwise be flattened due to Case I reaching a maximum value of $4.43 \cdot 10^5$ t at 271 days.

The plot highlights how the lower limits to the total mission time decrease, hence providing a wider time range, as the efficiency of the propulsion system increases. The minimum total mission time for each case is provided, alongside that resulting from the use of aerocapture, in Table 4.4.

While cases I, II, and III demonstrate a monotonically decreasing trend in IMLEO with increasing total mission times, Cases IV and V exhibit a minimum IMLEO value at 146 days and 182 days, respectively, beyond which they start increasing again due to the effect of the transfer time on the THAB mass. This tendency suggests that a limit on the minimum IMLEO also exists for cases from I to III, but would
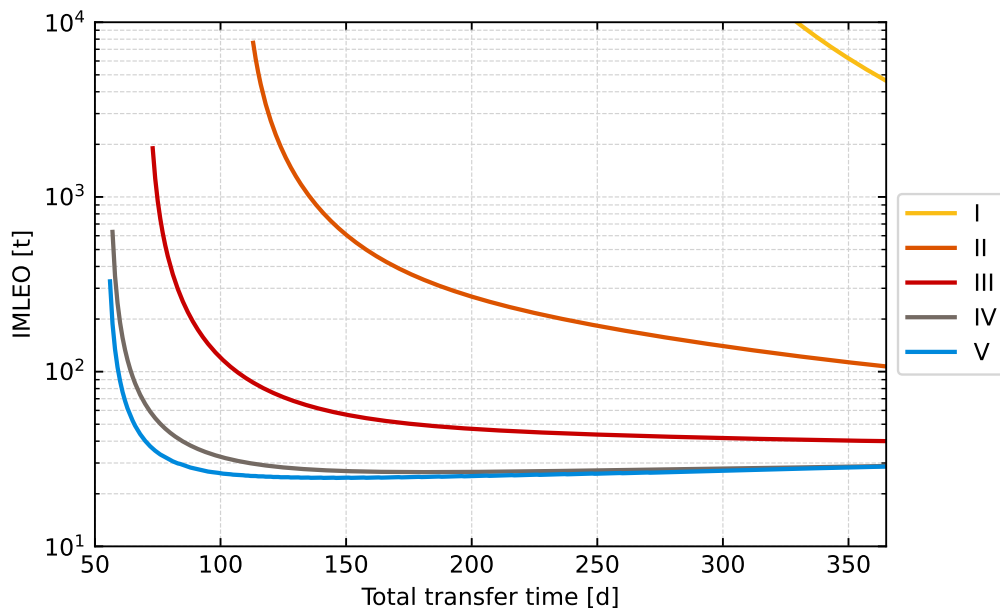
59

manifest for total mission times exceeding 365 days.

Figure 4.18: IMLEO for the purely propulsive case.

4.7.2 Aerocapture

As in the purely propulsive case, the IMLEO for aerocapture has been calculated for each total mission time over a sufficiently wide thrust range. Additionally, in this case, this operation has been performed for nose radii ranging from 2 m to 10 m, and, for each of them, in the case braking was conducted at infinity or atmospheric interface altitude.

The success of aerocapture implies that, once the atmosphere is exited, the orbit of the spacecraft is elliptical. The apoapsis altitude is a design parameter that is imposed at the beginning of the maneuver and it is automatically reached by providing the right Δv during the atmospheric passage. However, after the vehicle exits the atmosphere it will inevitably enter it again, unless a periapsis-raising maneuver is conducted. This maneuver is assumed at apoapsis altitude after jettisoning the aeroshield to reduce the mass and limit the propagation of the heat it is inevitably soaked with [12]. Upon calculation of the propellant mass required to perform the periapsis-raising maneuver, it demonstrated to amount to a maximum of 3% of the propellant required at Mars, independently on the propulsion system.

An illustrative example aerocapture IMLEO profile is presented in Figure 4.19 for Case III with braking at atmospheric altitude. The plot exhibits a similar pattern to that resulting from the corresponding purely propulsive case, although with a noticeable reduction in the mass of propellant at Mars as total mission time increases. However, this reduction, a direct consequence of braking with aerocapture, is offset by the mass of the shield. The optimal shield, in this scenario, features a nose radius of 5 m and 4 m for faster travels, transitioning quickly to a 3 m nose radius (see Table 4.3), explaining the peak near the asymptote. With increasing total time, the shield mass also increases due to its correlation with the entry mass which, excluding the propellant and considering the engine mass is quite low, is mainly dependent
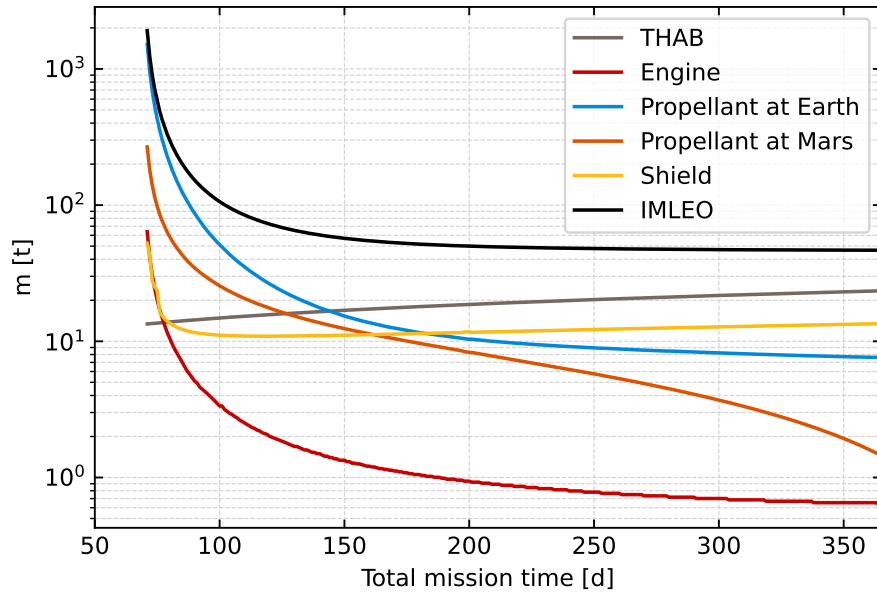
Figure 4.19: Mass contribution to the IMLEO of all the elements constituting the spacecraft in the case aerocapture is used.

on the THAB mass. Consequently, the trend of the shield mass curve mirrors that the THAB mass.

The braking distance has shown to provide greater variability than could have been predicted solely by observing the magnitude of the Δv, which, as shown in Figure 4.16, demonstrates no significant differences between the two cases. This is attributed to the influence of the radius in the modified rocket equation (2.16), where it is linked to the specific impulse, thrust, and propellant mass itself. Due to the interrelation among these parameters, the advantage for braking at infinity or at the atmospheric interface altitude has shown to depend on the chosen propulsion system, as evident in Figure 4.20. For Cases I, II, and III braking just before entering the atmosphere proves to be more beneficial, while Cases IV and V show a preference, although small, for braking at infinity.
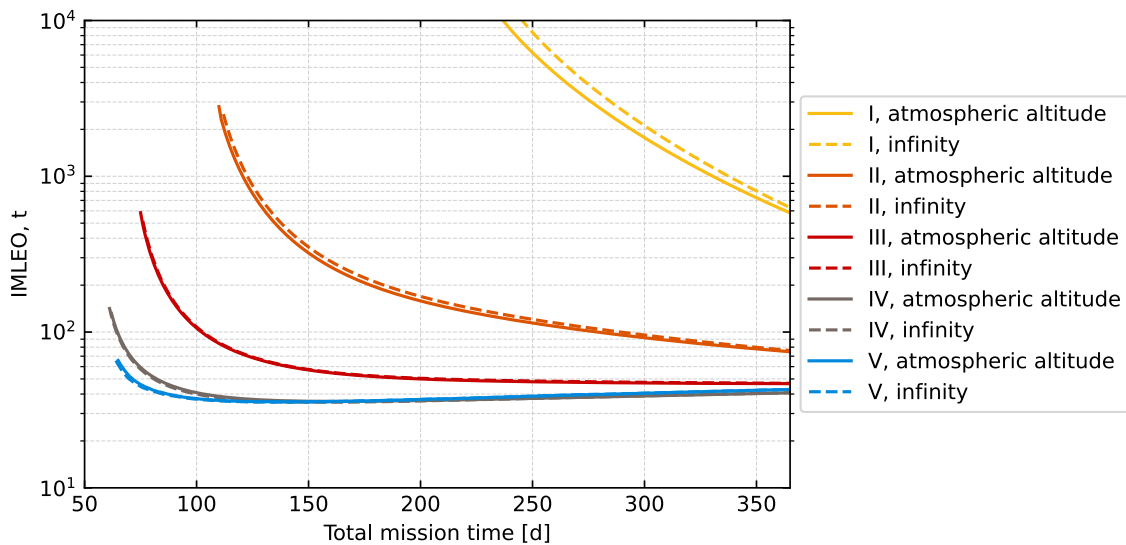
Figure 4.20: Effects of braking at atmospheric interface altitude or infinity for the various propulsion cases, with a nose radius of 3 m.

After determining the optimal braking point for each propulsion system, the minimum IMLEO values resulting from various nose radii have been selected and combined to obtain a single, optimized curve.

The resulting nose radii for each case across different total mission times are compiled in Table 4.3. A nose radius of 2 m yielded no results for any case or total mission time, due to the low entry mass limit imposed by the constraint on minimum altitude. Similarly, a nose radius of 10 m was not included in the table because, although it always produced results, the IMLEO was consistently much higher compared to other cases due to the weight of the aeroshield itself.

The table highlights how, regardless of the propulsion system, smaller nose radii are always preferable over longer transfer times. However, all cases demonstrate that, for shorter total mission times, larger aeroshields are more advantageous. In some cases, this is due to smaller aeroshields violating the entry mass limit, making the choice of larger aeroshields inevitable. In other cases, however, larger aeroshields resulted in lower IMLEOs due to the significant TPS mass required to withstand the high heat loads experienced by smaller aeroshields.

Case	R_N = 3 m	R_N = 4 m	R_N = 5 m	R_N = 6 m	R_N = 7 m	R_N = 8 m	R_N = 9 m
I	238-365 d	216-237 d	210-215 d	207-209 d	206 d	205 d	204 d
II	111-365 d	106-110 d	105 d	-	-	-	-
III	76-365 d	73-75 d	71-72 d	56 d	-	-	-
IV	61-365 d	58-60 d	57 d	-	-	56 d	-
V	64-365 d	59-63 d	57-58 d	56 d	-	-	55 d

Table 4.3: Nose radii that ensure minimum IMLEO depending on total mission time.

4.7.3 Aerocapture mass benefit

Once the IMLEO versus total mission time curves for the aerocapture scenario were established, they were compared with those resulting from the purely propulsive scenario, allowing for the calculation of the IMLEO mass gains:

$$\text{gain [\%]} = \frac{\text{IMLEO}_{\text{propulsive}} - \text{IMLEO}_{\text{aerocapture}}}{\text{IMLEO}_{\text{propulsive}}} \cdot 100. \tag{4.1}$$

Figure 4.21 effectively summarizes the results obtained. As shown, IMLEO gains resulting from the use of aerocapture heavily depend on the chosen propulsion system. For Case I, the average IMLEO gain reaches a maximum of 4.40×10^4 t for faster transfers, decreasing to gains on the order of 10^3 t for longer ones. For the subsequent cases, this gain decreases, eventually making aerocapture inconvenient for total mission times longer than 146 days in Case III, and for most of Cases IV and V.

The percentage gains on the IMLEO of the purely propulsive case were calculated and depicted in Figure 4.22. In the plot, a 100% gain indicates that aerocapture makes a journey of that duration feasible, where the sole use of the propulsion system did not provide results. For all cases, the efficiency of aerocapture is higher for shorter trips, decreasing as missions get longer.

This trend is attributed to the fact that, for faster missions, the propellant mass required at Mars is
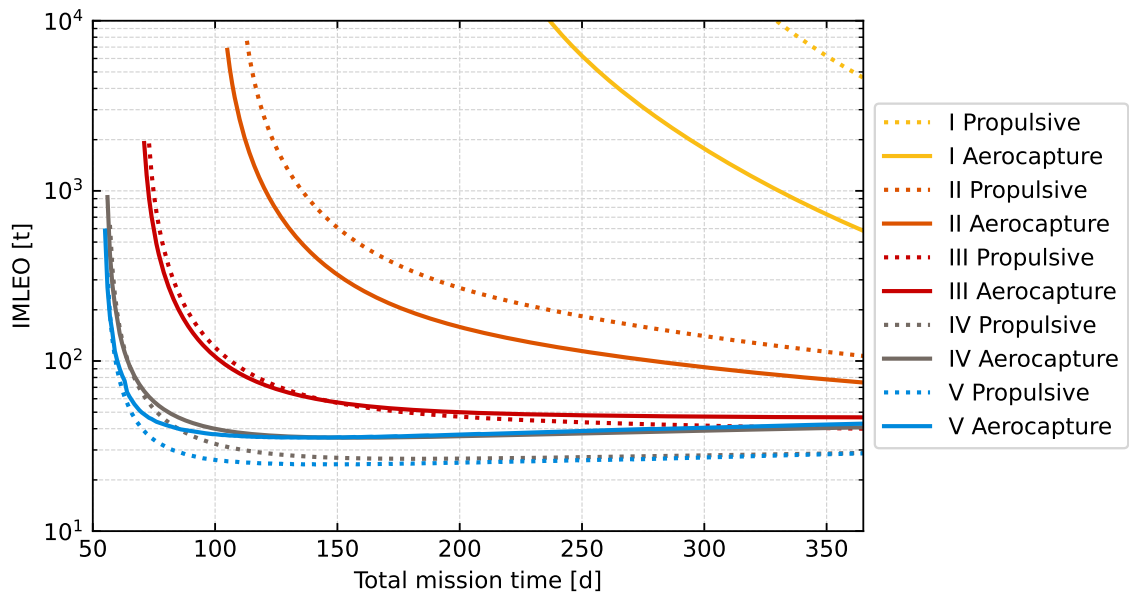
Figure 4.21: IMLEO for the purely propulsive and aerocapture scenarios.

substantial, which implies an even higher propellant mass at Earth, making propellant the main contributor to the IMLEO. Conversely, the mass of the aeroshield is lower than both the propellant masses (see Figure 4.19), thus its impact on the IMLEO is minimal. However, as mission durations increase, the required propellant mass decreases and the mass of the aeroshield becomes more significant in the IMLEO, making aerocapture less beneficial.

In Case I, the contribution of aerocapture is particularly remarkable, allowing for a reduction in the IMLEO of over 80%. The benefits of employing this strategy are also evident in Case II, where it enables an average reduction of 40%. However, aerocapture is generally not beneficial for Cases III, IV, and V, as the mass of the aeroshield exceeds the propellant savings.
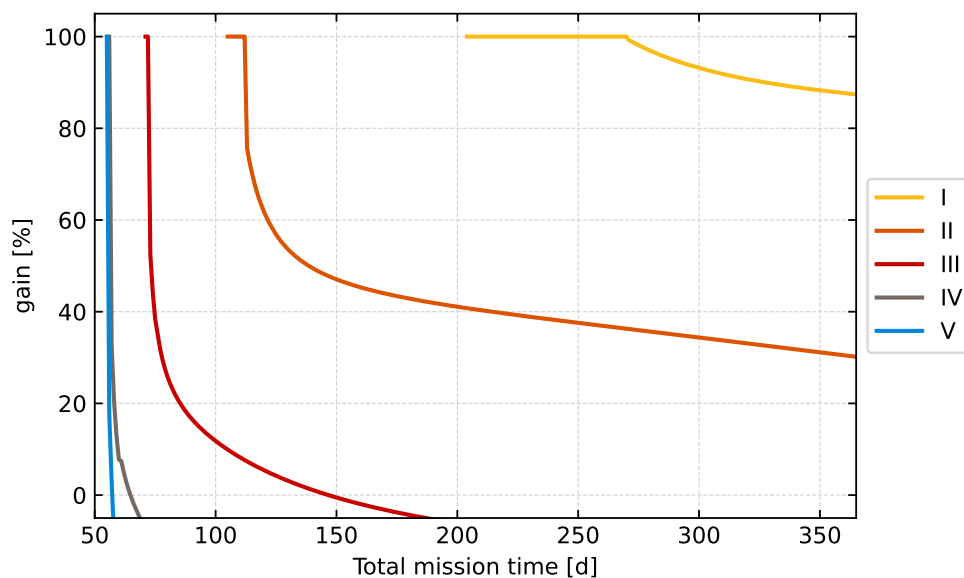
Figure 4.22: Percentage gain in IMLEO obtained by using aerocapture.

Despite this, it is noteworthy to observe that aerocapture remains advantageous for very fast transfers in all cases, allowing for a reduction in the minimum total mission time, as shown in Table 4.4. The minimum total mission time reduction is particularly significant for Case I, allowing for arrival at Mars over 60 days earlier than the purely propulsive counterpart. Similar to the gains in IMLEO, the reduction in minimum total mission time diminishes as propulsion systems become more advanced, confirming that aerocapture is primarily beneficial for currently available propulsion systems rather than futuristic, more efficient ones.

Case	Purely propulsive	Aerocapture
I	271 d	204 d
II	113 d	105 d
III	73 d	71 d
IV	57 d	56 d
V	56 d	55 d

Table 4.4: Minimum total mission time achievable for all the propulsion systems, in the purely propulsive and aerocapture scenarios.

Chapter 5

Conclusions

An analysis on the feasibility of employing aerocapture at Mars and its potential benefits to rapid crewed missions has been conducted. A literature survey explored the current state of research on fast transfers and aerocapture, revealing that while aerocapture is generally considered a viable strategy for reducing propellant mass, there is still a lack of studies exploring its potential to reduce transfer times.

The analysis of the aerocapture environment involved presenting the dynamics of atmospheric flight, the characteristics of the Martian atmosphere, and the peculiarities of the hypersonic flow regime that the spacecraft encounters upon entry. Special focus was given to analyzing the heating environment, revealing a lack of radiative heating models for Mars over a wide enough range of velocities, necessitating the adaptation of a model initially formulated for the similarly composed atmosphere of Venus.

A $70°$ sphere-cone aeroshield was designed, inspired by the Viking 1 aeroshell, with enhanced materials and a radius balancing mass and safety constraints.

The main constraints to the aerocapture maneuver were identified as being the minimum altitude required to achieve sufficient drag, the acceleration loads imposed on the crew, and the heat rates experienced by the shield. Acceleration loads were shown to be the primary constraint to the entry velocity, imposing that the atmosphere is crossed at velocities below 10 km/s, rendering direct insertion from interplanetary trips unfeasible for fast transfers. Achieving capture while maintaining a safe distance from the surface of Mars imposed constraints on the minimum aeroshield size and the entry mass, while the maximum heat rates that modern materials can withstand did not impose any additional constraint that was not already required by acceleration loads or minimum altitude.

The influence of expected atmospheric density uncertainties was explored, showing a negligible impact on maneuver feasibility.

Pareto fronts for the IMLEO were obtained for missions considering aerocapture or relying solely on the propulsion system in a range of total mission time going from 50 days to 365 days, for propulsion systems covering a wide range of Technology Readiness Levels. In both cases, the propellant mass was demonstrated to be predominant for faster transfers, albeit getting less impactful as mission duration increases, eventually becoming lower than the mass of the main structure and, in the case of aerocapture, that of the aeroshield.

Even the most efficient propulsion systems explored manifested a lower limit to the minimum mission time which, as the Initial Mass in Low Earth Orbit (IMLEO) itself, diminishes as their efficiency increases. Aerocapture was shown to allow for reaching Mars with shorter transfer durations for all propulsion systems, proving to be an allowing strategy to reach the Planet fast. Its mass benefits to the IMLEO manifested a heavy dependence on propulsion system efficiency, allowing for a mass benefit of over 80% for the only currently available propulsion system considered. As propulsion system efficiency was increased, however, the mass benefit would transition to lower values, eventually becoming disadvantageous for the more advanced, yet still immature, ones. This particular result shows how aerocapture can be a viable alternative to reach Mars with short trip durations without having to wait for the potential development of future technologies, representing a remarkable opportunity to open new possibilities in space exploration.

5.1   Recommendations for Future Research

This analysis represents a first attempt to integrate aerocapture with rapid transfers to Mars, requiring a simplified approach to certain intricate mission design concepts that deserve further exploration in future studies.

Firstly, future work should aim to liberate the interplanetary transfer from the assumptions of coplanarity and circular orbits that were used hereby, enabling a more precise determination of the required Δv, which may slightly differ from those obtained under current assumptions.

The feasibility of utilizing a spacecraft such as the one preliminarily designed in this analysis should also be explored. Additionally, alternative aeroshield configurations beyond the classical $70°$ sphere-cone should be investigated. Modern technological proposals, such as multi-stage jettisonable surfaces capable of drag modulation, have the potential to enhance aerocapture efficiency.

Finally, the heating environment encountered upon atmospheric entry at Mars, specifically that resulting from radiation, deserves a more thorough approach that utilizes either a radiative model specifically designed for the atmosphere of Mars or, ideally, Computational Fluid Dynamics. This approach would enable a more accurate estimation of the heating environment, potentially providing additional constraints or alleviating an aeroshield that, in this analysis, had to feature a massive Thermal Protection System.

Bibliography

[1] P. J. S. Gil and F. A. C. G. Teixeira. Rapid crewed missions to Mars with impulsive thrust. In *IAC 2021 Congress Proceedings, 72nd International Astronautical Congress (IAC), Dubai, United Arab Emirates*, 2021. URL `https://dl.iafastro.directory/event/IAC-2021/paper/62203/`. Paper ID 62203.

[2] A. G. C. Guerra, O. Bertolami, and P. J. S. Gil. Comparison of four space propulsion methods for reducing transfer times of crewed Mars missions. *The Journal of the Astronautical Sciences*, 69(2):284–311, 2022. ISSN 2195-0571. doi: 10.1007/s40295-021-00300-0. URL `https://doi.org/10.1007/s40295-021-00300-0`.

[3] D. R. Williams. Venus fact sheet. NASA Space Science Data Coordinated Archive, January 2024. Retrieved April 21, 2024, from `https://nssdc.gsfc.nasa.gov/planetary/factsheet/venusfact.html`.

[4] D. R. Williams. Mars fact sheet. NASA Space Science Data Coordinated Archive, January 2024. Retrieved April 21, 2024, from `https://nssdc.gsfc.nasa.gov/planetary/factsheet/marsfact.html`.

[5] B. G. Drake. Human Exploration of Mars Design Reference Architecture 5.0. Technical Report SP-2009-566, NASA, Johnson Space Center Houston, TX, U.S.A, July 2009. URL `https://www.nasa.gov/wp-content/uploads/2015/09/373665main_nasa-sp-2009-566.pdf?emrc=6dfe40`.

[6] D. S. Portree. *Humans to Mars: Fifty years of mission planning, 1950-2000*. Number 21 in Monographs in Aerospace History Series. NASA, Washington, DC, U.S.A, February 2001. ISBN 978-1-78039-305-6. NASA SP-2001-4521.

[7] D. R. Williams. Mars exploration timeline. NASA Space Science Data Coordinated Archive, May 2023. Retrieved April 12, 2024, from `https://nssdc.gsfc.nasa.gov/planetary/chronology_Mars.html`.

[8] R. K. Tripathi and J. E. Nealy. Mars radiation risk assessment and shielding design for long-term exposure to ionizing space radiation. In *2008 IEEE Aerospace Conference*, pages 1–9, Big Sky, MT, U.S.A, March 2008. doi: 10.1109/AERO.2008.4526513. URL `https://ieeexplore.ieee.org/document/4526513`.

[9] N. Kansas and D. Manzey. *Space Psychology and Psychiatry*, volume 22 of *Space Technology Library*. Springer, Dordrecht, Netherlands, 2nd edition, 2008. ISBN 978-1-4020-6769-3. doi: 10.1007/978-1-4020-6770-9. URL `https://doi.org/10.1007/978-1-4020-6770-9`.

[10] F. C. Sawin, J. Hayes, R. D. Francisco, and N. House. Considerations for development of countermeasures for physiological decrements associated with long-duration space missions. *Acta Astronautica*, 60(4-7):488–496, February-April 2007. ISSN 0094-5765. doi: 10.1016/j.actaastro. 2006.09.029. URL `https://doi.org/10.1016/j.actaastro.2006.09.029`.

[11] C. A. Kleuver. *Space Flight Dynamics*. Aerospace Series. Wiley, 111 River Street, Hoboken, NJ, U.S.A., 2nd edition, March 2018. ISBN 9781119157847.

[12] A. P. Girija. *A Systems Framework and Analysis Tool for Rapid Conceptual Design of Aerocapture Missions*. PhD thesis, Purdue University Graduate School, 610 Purdue Mall, West Lafayette, IN, U.S.A, August 2021. URL `https://doi.org/10.25394/PGS.14903349.v1`.

[13] H. S. London. Change of satellite orbit plane by aerodynamic maneuvering. *Journal of the Aerospace Sciences*, 29(3):323–332, 1962. ISSN 0095-9820. doi: 10.2514/8.9416. URL `https://doi.org/10.2514/8.9416`.

[14] M. Cruz. The aerocapture vehicle mission design concept-aerodynamically controlled capture of payload into Mars orbit. In *Conference on Advanced Technology for Future Space Systems*, pages 195–201, Hampton, VA, U.S.A, May 1979. AIAA. doi: 10.2514/6.1979-893. URL `https://arc.aiaa.org/doi/abs/10.2514/6.1979-893`.

[15] J. L. Hall, M. A. Noca, and R. W. Bailey. Cost-benefit analysis of the aerocapture mission set. *Journal of Spacecraft and Rockets*, 42(2):309–320, March-April 2005. ISSN 0022-4650. doi: 10.2514/1.4118. URL `https://doi.org/10.2514/1.4118`.

[16] T. R. Spilker, M. Adler, N. Arora, P. M. Beauchamp, J. A. Cutts, M. M. Munk, R. W. Powell, R. D. Braun, and P. F. Wercinski. Qualitative assessment of aerocapture and applications to future missions. *Journal of Spacecraft and Rockets*, 56(2):536–545, 2019. ISSN 0022-4650. doi: 10. 2514/1.A34056. URL `https://doi.org/10.2514/1.A34056`.

[17] R. Braun, R. Powell, and L. Hartung. Effect of interplanetary trajectory options on a manned Mars aerobrake configuration. Technical Publication 3019, NASA, Langley Research Center Hampton, VA 23665-5225, U.S.A, August 1990. URL `https://ntrs.nasa.gov/citations/19900016720`.

[18] A. P. Girija, S. J. Saikia, J. M. Longuski, Y. Lu, and J. A. Cutts. Quantitative assessment of aerocapture and applications to future Solar System exploration. *Journal of Spacecraft and Rockets*, 59(4):1074–1095, 2022. ISSN 0022-4650. doi: 10.2514/1.A35214. URL `https://doi.org/10.2514/1.A35214`.

[19] G. Walberg. Aerocapture for manned Mars missions - status and challenges. In *18th Atmospheric Flight Mechanics Conference*, New Orleans, LA, U.S.A, August 1991. doi: 10.2514/6.1991-2870. URL `https://arc.aiaa.org/doi/abs/10.2514/6.1991-2870`.

[20] A. P. Girija. Comparative study of planetary atmospheres and implications for atmospheric entry missions. *arXiv preprint*, July 2023. ISSN 2331-8422. doi: 10.48550/arXiv.2307.16277. URL `https://doi.org/10.48550/arXiv.2307.16277`.

[21] S. Solomon and J. Head. Evolution of the Tharsis province of Mars: The importance of heterogeneous lithospheric thickness and volcanic construction. *Journal of Geophysical Research*, 87 (B12):9755–9774, December 1982. ISSN 2169-8996. doi: 10.1029/JB087iB12p09755. URL `https://doi.org/10.1029/JB087iB12p09755`.

[22] A. Yin. An episodic slab-rollback model for the origin of the Tharsis rise on Mars: Implications for initiation of local plate subduction and final unification of a kinematically linked global plate-tectonic network on Earth. *Lithosphere*, 4(6):553–593, November 2012. ISSN 1947-4253. doi: 10.1130/L195.1. URL `https://doi.org/10.1130/L195.1`.

[23] M. Carr. The morphology of the Martian surface. *Space Science Reviews*, 25(3):231–284, March 1980. ISSN 0038-6308. doi: 10.1007/bf00221929. URL `https://link.springer.com/article/10.1007/BF00221929`.

[24] J. E. Lyne, A. Anagnost, and M. E. Tauber. Parametric study of manned aerocapture. II - Mars entry. *Journal of Spacecraft and Rockets*, 29(6):814–819, 1992. ISSN 0022-4650. doi: 10.2514/3.25536. URL `https://doi.org/10.2514/3.25536`.

[25] J. Esper and B. Aldrin. Mars small spacecraft human exploration resource prospector with aerobraking. In *International Astronautical Congress (IAC) 2019*, Washington, DC, U.S.A, October 2019.

[26] S. Bougher, G. Keating, R. Zurek, J. Murphy, R. Haberle, J. Hollingsworth, and R. Clancy. Mars Global Surveyor aerobraking: Atmospheric trends and model interpretation. *Advances in Space Research*, 23(11):1887–1897, 1999. ISSN 0273-1177. doi: 10.1016/S0273-1177(99)00272-0. URL `https://www.sciencedirect.com/science/article/pii/S0273117799002720`.

[27] R. D. Braun and R. W. Powell. Aerodynamic requirements of a manned Mars aerobraking transfer vehicle. *Journal of Spacecraft and Rockets*, 28(4):361–367, July-August 1991. ISSN 0022-4650. doi: 10.2514/3.26255. URL `https://doi.org/10.2514/3.26255`.

[28] J. Lyne. Physiologically constrained aerocapture for manned Mars missions. Technical Memorandum 103954, NASA, Ames Research Center Moffett Field, CA 94035-1000, U.S.A, August 1992. URL `https://ntrs.nasa.gov/citations/19930003532`.

[29] J. Dory. Constellation program human-system integration requirements. Technical Report CxP 70024, NASA, Johnson Space Center Houston, TX, U.S.A, November 2010. URL `https://ntrs.nasa.gov/citations/20120014522`.

[30] J. R. Davis, D. J. Fitts, and N. T. Server. NASA Space flight human-system standard. Volume 2: Human factors, habitability, and environmental health. Technical Report STD-3001, Revision D,

NASA, Johnson Space Center Houston, TX, U.S.A, October 2015. URL `https://www.nasa.gov/directorates/esdmd/hhp/human-spaceflight-and-aviation-standards/`.

[31] S. Hoffman. A comparison of aerobraking and aerocapture vehicles for interplanetary missions. In *Astrodynamics Conference*, Seattle, WA, U.S.A, August 1984. AIAA/AAS. doi: 10.2514/6.1984-2057. URL `https://doi.org/10.2514/6.1984-2057`.

[32] D. T. Lyons, S. Saunders, and D. G. Griffith. Magellan Venus mapping mission: aerobraking operations. *Acta Astronautica*, 35(9-11):669–676, June 1995. ISSN 0094-5765. doi: 10.1016/0094-5765(95)00032-U. URL `https://doi.org/10.1016/0094-5765(95)00032-U`.

[33] S. Val Serra, O. Bonnamy, O. Witasse, and O. Camino. Venus Express aerobraking. In *Proceedings of the 18th World Congress*, Milano, Italy, August-September 2011. doi: 10.3182/20110828-6-IT-1002.02433. URL `https://www.sciencedirect.com/science/article/pii/S1474667016436955`.

[34] J. Kawaguchi, T. Icbikawa, T. Nishimura, K. Uesugi, L. Efron, J. Ellis, P. R. Menon, and B. Tucker. Navigation for Muses-A (HITEN) aerobraking in the Earth's atmosphere – preliminary report. In *Proceedings of the 47th Annual Meeting of The Institute of Navigation*, pages 17–27, Williamsburg Hilton and National Conference Center, Williamsburg, VA, U.S.A., June 1991. URL `https://www.ion.org/publications/abstract.cfm?articleID=4975`.

[35] D. T. Lyons, J. G. Beerer, P. Esposito, M. D. Johnston, and W. H. Willcockson. Mars Global Surveyor: Aerobraking mission overview. *Journal of Spacecraft and Rockets*, 36(3):307–313, May-June 1999. ISSN 0022-4650. doi: 0.2514/2.3472. URL `https://doi.org/0.2514/2.3472`.

[36] J. C. J. Smith and J. L. Bell. 2001 Mars Odyssey Aerobraking. *Journal of Spacecraft and Rockets*, 42(3):406–415, May-June 2005. ISSN 0022-4650. doi: 10.2514/1.15213. URL `https://doi.org/10.2514/1.15213`.

[37] D. T. Lyons. Mars Reconnaissance Orbiter: aerobraking reference trajectory. In *AIAA/AAS Astrodynamics Specialist Conference and Exhibit*, Monterey, CA, U.S.A., August 2002. doi: 10.2514/6.2002-4821. URL `https://arc.aiaa.org/doi/abs/10.2514/6.2002-4821`.

[38] M. Denis, P. Schmitz, S. Sangiorgi, R. Guilanya, P. Mitschdoerfer, M. Montagna, H. Renault, and N. Kutrowski. Thousand times through the atmosphere of Mars: Aerobraking the ExoMars Trace Gas Orbiter. In *SpaceOps Conference*, Marseille, France, May 2018. doi: 10.2514/6.2018-2713. URL `https://arc.aiaa.org/doi/abs/10.2514/6.2018-2713`.

[39] A. P. Girija. Comparative study of planetary atmospheric uncertainties and design rules for aerocapture missions. *arXiv preprint*, October 2023. ISSN 2331-8422. doi: 10.48550/arXiv.2310.10067. URL `https://doi.org/10.48550/arXiv.2310.10067`.

[40] X. N. Vinh, A. Busemann, and D. R. Culp. *Hypersonic and Planetary Entry Flight Mechanics*, chapter 12. The University of Michigan Press, 839 Greene Street Ann Arbor, MI 48104-3209, U.S.A, January 1980. ISBN 978-0-472-10004-0.

[41] U. Walter. *Astronautics, the physics of space flight*. Springer, Gewerbestrasse 11, 6330 Cham, Switzerland, 3rd edition, February 2019. ISBN 978-3-319-74373-8. doi: 10.1007/ 978-3-319-74373-8. URL https://doi.org/10.1007/978-3-319-74373-8.

[42] P. Gallais. *Atmospheric re-entry vehicle mechanics*. Springer, Tiergartenstrasse 17, D-69121 Heidelberg, Germany, 1st edition, September 2007. ISBN 978-3-540-73647-9. doi: 10.1007/ 978-3-540-73647-9. URL https://doi.org/10.1007/978-3-540-73647-9.

[43] A. D. Vallado. *Fundamentals of Astrodynamics and Applications*. Microcosm Press, 4940 West 147th Street, Hawthorne, CA 90250-6708 USA, 4th edition, March 2013. ISBN 978-1-881883-18-0.

[44] P. Wooster, R. Braun, J. Ahn, and Z. Putnam. Trajectory options for human Mars missions. In *AIAA/AAS Astrodynamics Specialist Conference and Exhibit*, Keystone, CO, U.S.A, August 2006. doi: 10.2514/6.2006-6308.

[45] J. R. Wertz. Interplanetary round trip mission design. *Acta Astronautica*, 55(3-9):221–232, August-November 2004. ISSN 0094-5765. doi: 10.1016/j.actaastro.2004.05.019. URL https://doi.org/ 10.1016/j.actaastro.2004.05.019.

[46] N. S. Amade and J. R. Wertz. Design of a Mars rapid round trip mission. In *AIAA SPACE 2010 Conference Exposition*, Anaheim, CA, U.S.A, August-September 2010. doi: 10.2514/6. 2010-8642. URL https://doi.org/10.2514/6.2010-8642.

[47] J.-M. Salotti and B. Claverie. Human mission to Mars: All-up vs pre-deploy. In *Global Space Exploration Conference*, Wahington, DC, U.S.A, May 2012.

[48] J.-M. Salotti. Revised scenario for human missions to Mars. *Acta Astronautica*, 81(1):237–287, July 2012. ISSN 0094-5765. doi: 10.1016/j.actaastro.2012.07.018. URL https://doi.org/10. 1016/j.actaastro.2012.07.018.

[49] K. M. Hughes, P. J. Edelman, J. Longuski, M. Loucks, J. P. Carrico, and D. A. Tito. Fast Mars free-returns via Venus gravity assist. In *Astronautics AIAA/AAS Astrodynamics Specialist Conference*, San Diego, CA, U.S.A, August 2014. doi: 10.2514/6.2014-4109. URL https://doi.org/10. 2514/6.2014-4109.

[50] H. Price, R. Shishko, J. Mrozinski, and R. Woolley. Concept for 2033 crewed Mars orbital mission with Venus flyby. *Journal of Spacecraft and Rockets*, 60(1):49–58, 2023. ISSN 0022-4650. doi: 10.2514/1.A35437. URL https://doi.org/10.2514/1.A35437.

[51] M. Okutsu and J. Longuski. Mars free returns via gravity assist from Venus. *Journal of Spacecraft and Rockets*, 39(1):31–36, January-February 2002. ISSN 0022-4650. doi: 10.2514/2.3778. URL https://doi.org/10.2514/2.3778.

[52] D. F. Landau and J. M. Longuski. A reassessment of trajectory options for human missions to Mars. In *AIAA/AAS Astrodynamics Specialist Conference and Exhibit*, Providence, RI, U.S.A, August 2004. doi: 10.2514/6.2004-5095. URL `https://doi.org/10.2514/6.2004-5095`.

[53] T. T. McConaghy, J. M. Longuski, and D. V. Byrnes. Analysis of a broad class of Earth-Mars cycler trajectories. In *AIAA/AAS Astrodynamics Specialist Conference and Exhibit*, Monterey, CA, U.S.A, August 2002. doi: 10.2514/6.2002-4420. URL `https://doi.org/10.2514/6.2002-4420`.

[54] M. L. Balestrero and W. Markus. Parametric design of a crew transfer vehicle for Earth–Mars cyclers. *Journal of Spacecraft and Rockets*, 57(3):565–579, June 2020. ISSN 0022-4650. doi: 10.2514/1.A34637. URL `https://doi.org/10.2514/1.A34637`.

[55] D. F. Landau and J. M. Longuski. Comparative assessment of human-Mars-mission technologies and architectures. *Acta Astronautica*, 65(7-8):893–911, October 2009. ISSN 0094-5765. doi: 10.1016/j.actaastro.2009.02.008. URL `https://doi.org/10.1016/j.actaastro.2009.02.008`.

[56] G. D. Nordley and R. L. Forward. Mars-Earth rapid interplanetary tether transport system: I. initial feasibility analysis. *Journal of Propulsion and Power*, 17(3):499–507, May 2001. ISSN 1533-3876. doi: 10.2514/2.5798. URL `https://doi.org/10.2514/2.5798`.

[57] J. A. Christian, G. Wells, J. Lafleur, A. Verges, and R. D. Braun. Extension of traditional entry, descent, and landing technologies for human Mars exploration. *Journal of Spacecraft and Rockets*, 45(1):130–141, January 2008. ISSN 0022-4650. doi: 10.2514/1.31929. URL `https://doi.org/10.2514/1.31929`.

[58] P. Subrahmanyam and D. Rasky. Entry, descent, and landing technological barriers and crewed Mars vehicle performance analysis. *Progress in Aerospace Sciences*, 91:1–26, July 2017. ISSN 1873-1724. doi: 10.1016/j.paerosci.2016.12.005. URL `https://doi.org/10.1016/j.paerosci.2016.12.005`.

[59] H. S. Wright, D. Y. Oh, C. H. Westhelle, J. L. Fisher, R. E. Dyke, K. T. Edquist, J. L. Brown, H. L. Justh, and M. M. Munk. Mars aerocapture systems study. Technical Memorandum 2006-214522, NASA, Langley Research Center, Johnson Space Center Houston, TX, U.S.A, November 2006. URL `https://ntrs.nasa.gov/citations/20060056070`.

[60] W. Rochelle, S. Bouslog, P. Ting, and D. Curry. Aerothermodynamic environments for Mars entry, Mars return, and lunar return aerobraking missions. In *5th Conference on Advanced Technology for Future Space Systems*, Seattle, WA, U.S.A, June 1990. doi: 10.2514/6.1990-1701. URL `https://arc.aiaa.org/doi/abs/10.2514/6.1990-1701`. AIAA Paper 1990-1701.

[61] M. E. Tauber, J. V. Bowles, and L. Yang. Use of atmospheric braking during Mars missions. *Journal of Spacecraft and Rockets*, 27(5):514–521, 1990. ISSN 0022-4650. doi: 10.2514/3.26174. URL `https://doi.org/10.2514/3.26174`.

[62] M. E. Tauber and K. Sutton. Stagnation-point radiative heating relations for earth and Mars entries. *Journal of Spacecraft and Rockets*, 28(1):40–42, 1991. ISSN 0022-4650. doi: 10.2514/3.26206. URL https://doi.org/10.2514/3.26206.

[63] P. Lu, C. J. Cerimele, M. A. Tigges, and D. A. Matz. Optimal aerocapture guidance. *Journal of Guidance, Control, and Dynamics*, 38(4):553–565, 2015. ISSN 0731-5090. doi: 10.2514/1. G000713. URL https://doi.org/10.2514/1.G000713.

[64] R. A. Niemann. Two-position roll modulation of lift for aerodynamic braking of a Mars entry vehicle. *Journal of Spacecraft and Rockets*, 5(6):725–728, June 1968. ISSN 0022-4650. doi: 10.2514/3. 29337. URL https://doi.org/10.2514/3.29337.

[65] N. X. Vinh, N. A. Bletsos, R. D. Culp, and A. Busemann. Flight with lift modulation inside a planetary atmosphere. *AIAA Journal*, 15(11):1617–1623, November 1977. ISSN 0001-1452. doi: 10.2514/3.7461. URL https://doi.org/10.2514/3.7461.

[66] R. D. Brau and R. W. Powell. Predictor-corrector guidance algorithm for use in high-energy aerobraking system studies. *Journal of Guidance, Control, and Dynamics*, 15(3):672–678, May-June 1992. ISSN 0731-5090. doi: 10.2514/3.20890. URL https://doi.org/10.2514/3.20890.

[67] G. F. Mendeck and L. C. McGrew. Post-flight EDL entry guidance performance of the 2011 Mars Science Laboratory Mission. In *23rd AAS/AIAA Space Flight Mechanics Meeting*, Kauai, HI, U.S.A, February 2013. URL https://ntrs.nasa.gov/citations/20130009144.

[68] G. F. Mendeck and L. E. Craig. Entry guidance for the 2011 Mars Science Laboratory Mission. In *AIAA Atmospheric Flight Mechanics Conference*, Portland, OR, U.S.A, August 2011. doi: 10. 2514/6.2011-6639. URL https://doi.org/10.2514/6.2011-6639.

[69] C. Heidrich, E. Roelke, S. Albert, and R. Braun. Comparative study of lift- and drag-modulation control strategies for aerocapture. In *43rd Annual AAS Guidance, Navigation and Control Conference*, Breckenridge, CO, January 2020.

[70] Z. R. Putnam, I. G. Clark, and R. D. Braun. Drag modulation flight control for aerocapture. In *2012 IEEE Aerospace Conference*, pages 1–10, March 2012. doi: 10.1109/aero.2012.6186999. URL https://ieeexplore.ieee.org/document/6186999.

[71] Z. R. Putnam and R. D. Braun. Drag-modulation flight-control system options for planetary aerocapture. *Journal of Spacecraft and Rockets*, 51(1):139–150, February 2014. ISSN 0022-4650. doi: 10.2514/1.A32589. URL https://doi.org/10.2514/1.A32589.

[72] F. A. Teixeira. Rapid crewed missions to Mars: Impulsive case. Master's thesis, 2021. URL https://scholar.tecnico.ulisboa.pt/records/jFSE_39eZSkCSNLgkmX-1CNJyLfRSS6OJgNl.

[73] H. D. Curtis. *Orbital Mechanics for Engineering Students*. Butterworth-Heinemann, Elsevier, The Boulevard, Langford Lane, Kidlington, Oxford OX5 1GB, United King-

dom; 50 Hampshire Street, 5th Floor, Cambridge, MA 02139, U.S.A., 4th edition, August 2020. ISBN 9780081021330. URL `https://shop.elsevier.com/books/orbital-mechanics-for-engineering-students/curtis/978-0-12-824025-0`.

[74] R. H. Gooding. A procedure for the solution of Lambert's orbital boundary-value problem. *Celestial Mechanics and Dynamical Astronomy*, 48:145–165, June 1990. ISSN 0923-2958. doi: 10.1007/BF00049511. URL `https://doi.org/10.1007/BF00049511`.

[75] M. Jorge. Lamberthub: ICATT Version (0.1). Zenodo, June 2021. Retrieved December 18, 2023, from `https://doi.org/10.5281/zenodo.4971895`.

[76] K. D. Hicks. *Introduction to astrodynamic reentry*. Books Express Publishing, Greenham Business Park, Newbury, Berkshire, United Kingdom, September 2009. ISBN 9781782663102.

[77] J. Mankins. Technology readiness levels - a white paper. Technical report, NASA, Johnson Space Center Houston, TX, U.S.A, April 1995.

[78] J. T. S. R. Pinto. A survey of modern and future space propulsion methods. Master's thesis, November 2019. URL `https://scholar.tecnico.ulisboa.pt/records/vI5Ul1XuigZaVmnBvJY1ynVOczqJEhdsMHd1`.

[79] F. A. C. G. Teixeira and P. J. S. Gil. Rocket equation with burn losses and propellant tanks jettison. *Journal of Spacecraft and Rockets*, 59(2):685–690, March-April 2022. doi: 0.2514/1.A35201.

[80] G. R. Hintz. *Orbital Mechanics and Astrodynamics*. Springer Cham, Gewerbestrasse 11 6330 Cham, Zurich, Switzerland, 1 edition, January 2015. doi: 10.1007/978-3-319-09444-1. URL `https://link.springer.com/book/10.1007/978-3-319-09444-1`.

[81] J. D. J. Anderson. *Hypersonic and High Temperature Gas Dynamics*. AIAA Education Series. American Institute of Aeronautics and Astronautics, 1801 Alexander Bell Drive, Reston, VA 20191-4344, U.S.A., 2nd edition, October 2006. ISBN 9781563477805.

[82] A. P. Girija, S. J. Saikia, J. M. Longuski, and J. A. Cutts. Amat: A python package for rapid conceptual design of aerocapture and atmospheric entry, descent, and landing (EDL) missions in a Jupyter environment. *Journal of Open Source Software*, 6(67):3710, November 2021. ISSN 2475-9066. doi: 10.21105/joss.03710. URL `https://doi.org/10.21105/joss.03710`.

[83] R. M. Haberle, R. T. Clancy, F. Forget, M. D. Smith, and R. W. Zurek. *The Atmosphere and Climate of Mars*, volume 18 of *Cambridge Planetary Science*. Cambridge University Press, University Printing House, Cambridge CB2 8BS, United Kingdom, August 2017. ISBN 9781107016187. doi: 10.1017/9781139060172. URL `http://www.cambridge.org/9781107016187`.

[84] S. A. Haider. *Aeronomy of Mars*, volume 469 of *Astrophysics and Space Science Library*. Springer Nature Singapore, 152 Beach Road, 21-01/04 Gateway East, Singapore 189721, Singapore, 1st edition, August 2023. ISBN 9789819931378. URL `https://link.springer.com/book/10.1007/978-981-99-3138-5`.

[85] H. L. Justh, A. M. Dwyer Cianciolo, and J. Hoffman. Mars Global Reference Atmospheric Model (Mars-GRAM): User guide. Technical Memorandum 20210023957, NASA, Johnson Space Center Houston, TX, U.S.A, November 2021. URL `https://ntrs.nasa.gov/api/citations/20210023957/downloads/Mars-GRAM%20User%20Guide.pdf`.

[86] P. W. White and J. Hoffman. Earth Global Reference Atmospheric Model (Earth-GRAM): User guide. Technical Memorandum 20210022157, NASA, Johnson Space Center Houston, TX, U.S.A, September 2021. URL `https://ntrs.nasa.gov/api/citations/20210022157/downloads/Earth-GRAM%20User%20Guide_1.pdf`.

[87] H. L. Justh, A. M. Dwyer Cianciolo, and J. Hoffman. Venus Global Reference Atmospheric Model (Venus-GRAM): User guide. Technical Memorandum 20210022168, NASA, Johnson Space Center Houston, TX, U.S.A, September 2021. URL `https://ntrs.nasa.gov/api/citations/20210022168/downloads/Venus-GRAM%20User%20Guide.pdf`.

[88] T. Al-Shemmeri. *Engineering Fluid Mechanics*. Ventus Publishing ApS, 3336 Arapahoe Road, Unit B-114, Erie, CO 80516-6014, U.S.A., 2012. ISBN 9788740301144.

[89] A. Sasoh. *Compressible Fluid Dynamics and Shock Waves*. Springer Nature Singapore, 152 Beach Road, 21-01/04 Gateway East, Singapore 189721, Singapore, 1st edition, January 2020. doi: 10.1007/978-981-15-0504-1.

[90] N. M. Laurendau. *Statistical Thermodynamics: Fundamentals and Applications*. Cambridge University Press, University Printing House, Cambridge CB2 8BS, United Kingdom, 1st edition, November 2005. ISBN 9780521846356. URL `https://www.cambridge.org/us/universitypress/subjects/engineering/thermal-fluids-engineering/statistical-thermodynamics-fundamentals-and-applications?format=HB&isbn=9780521846356`.

[91] B. W. McCormick. *Aerodynamics, Astronautics, and Flight Mechanics*. John Wiley Sons, 111 River Street, Hoboken, NJ 07030-5774, U.S.A., 2nd edition, September 1994. ISBN 9780471575061. URL `https://www.wiley.com/en-br/Aerodynamics%2C+Aeronautics%2C+and+Flight+Mechanics%2C+2nd+Edition-p-9780471575061`.

[92] M. A. Furudate. Mc-new: A program to calculate newtonian aerodynamic coefficients based on Monte-Carlo integration. *Aerospace*, 9(6):330, June 2022. ISSN 2226-4310. doi: 10.3390/aerospace9060330. URL `https://www.mdpi.com/2226-4310/9/6/330`.

[93] J. Meseguer, I. Pérez-Grande, and A. Sanz-Andrés. *Spacecraft Thermal Control*. Woodhead Publishing, 80 High Street, Sawston, Cambridge CB22 3HJ, United Kingdom, 1st edition, August 2012. ISBN 9781845699963.

[94] M. D. Griffin and J. R. French. *Space Vehicle Design*. AIAA Education Series. American Institute of Aeronautics and Astronautics, 1801 Alexander Bell Drive, Reston, VA 20191-4344, U.S.A., 2nd edition, December 2005. ISBN 9781563475399.

[95] P. M. Sforza. *Manned Spacecraft Design Principles*. Butterworth-Heinemann, Elsevier, The Boulevard, Langford Lane, Kidlington, Oxford OX5 1GB, United Kingdom; 225 Wyman Street, Waltham, MA 02451, U.S.A., 1st edition, November 2015. ISBN 9780128044254.

[96] I. Cozmuta, M. J. Wright, B. Laub, and W. H. Willcockson. Defining ablative thermal protection system margins for planetary entry vehicles. In *42nd AIAA Thermopysics Conference*, Honolulu, HI, U.S.A., June 2011. doi: 10.2514/6.2011-3757. URL https://doi.org/10.2514/6.2011-3757.

[97] K. Sutton and A. J. Graves. A general stagnation-point convective-heating equation for arbitrary gas mixtures. Technical Report R-376, NASA, NASA Langley Research Center, Hampton, Va. 23365, U.S.A., November 1971. URL https://ntrs.nasa.gov/api/citations/19720003329/downloads/19720003329.pdf.

[98] J. A. Samareh. A multidisciplinary tool for systems analysis of planetary entry, descent, and landing (SAPE). Technical Memorandum 2009-215950, NASA, Langley Research Center, Hampton, Virginia 23681-2199, U.S.A, November 2009. URL https://ntrs.nasa.gov/api/citations/20090041828/downloads/20090041828.pdf.

[99] T. K. West and A. M. Brandis. Stagnation-point aeroheating correlations for Mars entry. *Journal of Spacecraft and Rockets*, 57(2):319–327, January 2020. ISSN 0022-4650. doi: 10.2514/1.A34602. URL https://doi.org/10.2514/1.A34602.

[100] S. Craig and J. E. Lyne. A parametric study of aerocapture for missions to Venus. *Journal of Spacecraft and Rockets*, 42(6):1035–1038, November-December 2005. doi: 10.2514/1.2589. URL https://doi.org/10.2514/1.2589.

[101] W. A. Page and H. T. Woodward. Radiative and convective heating during Venus entry. *AIAA Journal*, 10(10):1379–1381, October 1972. ISSN 0001-1452. doi: 10.2514/3.6632. URL https://doi.org/10.2514/3.6632.

[102] K. M. Rauf, H. Hossieni, D. Majeed, and R. Ibrahim. Comparing the atmospheric compositions of all planets and giant moons in Solar System. *Journal of Astrobiology Outreach*, 3(3), July 2015. ISSN 2332-2519. doi: 10.4172/2332-2519.1000136. URL https://doi.org/10.4172/2332-2519.1000136.

[103] F. A. Demele. A study of the convective and radiative heating of shapes entering the atmospheres of Venus and Mars at superorbital speeds. Technical Note D-2064, NASA, Ames Research Center, Moffett Field, CA, U.S.A, December 1963. URL https://ntrs.nasa.gov/api/citations/19640001994/downloads/19640001994.pdf.

[104] V. N. Mirski. Radiative heating of bodies entering the atmosphere of Venus. *Fluid Dynamics*, 27:556–559, July 1992. ISSN 0015-4628. doi: 10.1007/BF01051334. URL https://doi.org/10.1007/BF01051334.

[105] D. R. Williams. Viking mission to Mars. NASA Space Science Data Coordinated Archive, April 2018. URL `https://nssdc.gsfc.nasa.gov/planetary/viking.html`. Retrieved March 15, 2024, from `https://nssdc.gsfc.nasa.gov/planetary/viking.html`.

[106] K. T. Edquist, M. J. Wright, and G. A. J. Allen. Viking afterbody heating computations and comparisons to flight data. In *44th AIAA Aerospace Sciences Meeting and Exhibit*, Reno, NV, U.S.A., January 2006. doi: 10.2514/6.2006-386. URL `https://arc.aiaa.org/doi/10.2514/6.2006-386`.

[107] D. K. Prabhu and D. A. Saunders. On heatshield shapes for Mars entry capsules. In *50th AIAA Aerospace Sciences Meeting including the New Horizons Forum and Aerospace Exposition*, Nashville, TN, U.S.A., January 2012. doi: 10.2514/6.2012-399. URL `https://ntrs.nasa.gov/api/citations/20120004297/downloads/20120004297.pdf`.

[108] T. R. White, M. Mahzari, D. Bose, and J. A. Santos. Post-flight analysis of the Mars Science Laboratory entry aerothermal environment and thermal protection system response. In *44th AIAA Thermophysics Conference*, San Diego, CA, U.S.A., June 2013. doi: 10.2514/6.2013-2779. URL `https://ntrs.nasa.gov/api/citations/20140005545/downloads/20140005545.pdf`.

[109] S. A. Striepe and W. T. Suit. Aeroassist Flight Experiment. Technical Memorandum 100556, NASA, Johnson Space Center Houston, TX, U.S.A, February 1988. URL `https://ntrs.nasa.gov/citations/19880011860`.

[110] J. E. Lyne, P. Wercinski, G. Walberg, and R. Jits. Mars aerocapture studies for the Design Reference Mission. Technical Report NCC2-5198, University of Tennessee, NASA, and North Carolina State University, Johnson Space Center Houston, TX, U.S.A, January 1997. URL `https://ntrs.nasa.gov/citations/19990053343`.

[111] W. B. Stephens and M. S. Anderson. Structural analyses for the modification and verification of the Viking aeroshell. Technical Note D-8300, NASA, Johnson Space Center Houston, TX, U.S.A, November 1976. URL `https://ntrs.nasa.gov/api/citations/19770005493/downloads/19770005493.pdf`.

[112] M. J. Wright, R. A. S. Beck, K. T. Edquist, D. Driver, S. A. Sepka, E. M. Slimko, W. H. Willcockson, A. DeCaro, and H. H. Hwang. Sizing and margins assessment of the Mars Science Laboratory aeroshell thermal protection system. In *41st AIAA Thermophysics Conference*, San Antonio, TX, U.S.A., June 2009. doi: 10.2514/1.A32579. URL `https://arc.aiaa.org/doi/abs/10.2514/1.A32579?journalCode=jsr`.

[113] L. Weijie, Z. Zhongwei, J. Zuhang, Z. Mengdie, Z. Jun, H. Haiming, and L. I. N. E. C. Jun. Comprehensive performance of multifunctional lightweight composite reinforced with integrated preform for thermal protection system exposed to extreme environment. *Aerospace Science and Technology*, 126, July 2022. ISSN 1270-9638. doi: 10.1016/j.ast.2022.107647. URL `https://www.sciencedirect.com/science/article/pii/S1270963822003212#br0170`.

[114] E. Venkatapathy, B. Laub, G. J. Hartman, J. O. Arnold, M. J. Wright, and G. A. Allen. Thermal protection system development, testing, and qualification for atmospheric probes and sample return missions: Examples for Saturn, Titan and Stardust-type sample return. *Advances in Space Research*, 44(1):138–150, July 2009. ISSN 0273-1177. doi: 10.1016/j.asr.2008.12.023. URL `https://www.sciencedirect.com/science/article/pii/S0273117709001434`.

[115] S. Sepka and J. A. Samareh. Thermal protection system mass estimating relationships for blunt-body, earth entry spacecraft. In *45th AIAA Thermophysics Conference*, Dallas, TX, U.S.A., June 2015. doi: 10.2514/6.2015-2507. URL `https://ntrs.nasa.gov/api/citations/20160004208/downloads/20160004208.pdf`.

[116] F. S. Milos, Y.-K. Chen, and M. Mahzari. Arcjet tests and thermal response analysis for dual-layer woven carbon phenolic. *Journal of Spacecraft and Rockets*, 55(3):712–722, May-June 2018. doi: 10.2514/1.A34142. URL `https://arc.aiaa.org/doi/pdf/10.2514/1.A34142`.

[117] D. J. Rainford and D. P. Gradwell. *Ernsting's Aviation Medicine*. CRC Press, 6000 Broken Sound Parkway NW, Boca Raton, FL, U.S.A., 4th edition, March 2006. ISBN 9780340813195.

[118] CEL Components S.R.L. Aluminum honeycomb, December 2021. Retrieved April 30, 2024, from `https://www.cel.eu/img_ins/files/Alluminio_38_uk_Rev12.pdf`.

[119] P. Bauduin. MSL (Curiosity). Weebau Spaceflight Encyclopedia, January 2019. Retrieved March 2, 2024, from `https://weebau.com/satplan/msl.htm`.